Technische Universität München
TUM School of Natural Sciences

Electronic Structure and Quasiparticle Lifetime Oscillations in CoSi

Nico Huber

Vollständiger Abdruck der von der TUM School of Natural Sciences der Technischen Universität München zur Erlangung des akademischen Grades eines

Doktors der Naturwissenschaften (Dr. rer. nat.)

genehmigten Dissertation.

Vorsitz:		Prof. Dr. Laura Classen
Prüfende der Dissertation:	1.	Prof. Dr. Christian Pfleiderer
	2.	Prof. Dr. Rudolf Gross

Die Dissertation wurde am 30.07.2024 bei der Technischen Universität München eingereicht und durch die TUM School of Natural Sciences am 11.02.2025 angenommen.

Abstract

In this thesis, we report on quantum oscillation studies of the chiral topological semimetal CoSi. The Fermi surface geometry is determined by angular-dependent measurements of the Shubnikov-de Haas and de Haas-van Alphen effect at temperatures down to the mK-regime and in high magnetic fields up to 31.4 T. Multiple oscillation frequencies originating from Fermi surface pockets centered around the R- and Γ-point of the simple cubic Brillouin zone are observed. The frequencies are compared to ab-initio band structure calculations and are discussed with regard to the band topology. Our results establish the presence of symmetry-enforced degeneracies on the entire Brillouin zone boundary and complete the experimental determination of the Fermi surface of CoSi. Combinations of fundamental frequencies are detected in the Shubnikov-de Haas spectra. The oscillations at the difference frequency exhibit an unusually weak temperature dependent damping and cannot be explained by conventional mechanisms. We show that our findings are in excellent agreement with oscillations of the quasiparticle lifetime in the presence of a finite interband coupling. The proposed mechanism may explain unexpected oscillation frequencies reported in the literature and provide a tool to study the coupling between different parts of the Fermi surface in a wide range of material classes.

Kurzzusammenfassung

In dieser Dissertation berichten wir über Quantenoszillationsstudien an dem chiralen topologischen Halbmetall CoSi. Die Geometrie der Fermi-Fläche wird durch winkelabhängige Messungen des Shubnikov-de Haas und des de Haas-van Alphen Effekts bei Temperaturen bis in den mK-Bereich und unter hohen Magnetfeldern von bis zu 31.4 T bestimmt. Es werden mehrere Oszillationfrequenzen beobachtet, die von Fermi-Flächen stammen, welche um den R- und Γ-Punkt der einfach kubischen Brillouin-Zone zentriert sind. Die Frequenzen werden mit ab-initio Bandstrukturrechnungen verglichen und im Hinblick auf die Topologie der Bandstruktur diskutiert. Unsere Resultate belegen die Existenz von symmetrieerzwungenen Entartungen am gesamten Rand der Brillouin-Zone und vervollständigen die experimentelle Bestimmung der Fermi-Fläche von CoSi. In den Shubnikov-de Haas Spektren werden Kombinationen von Fundamentalfrequenzen detektiert. Die Oszillazionen mit der Differenzfrequenz weisen eine ungewöhnlich schwache temperaturabhängige Dämpfung auf und können nicht durch konventionelle Mechanismen erklärt werden. Wir zeigen, dass unsere Ergebnisse in hervorragender Übereinstimmung mit Oszillationen der Quasiteilchen-Lebensdauer in Anwesenheit einer endlichen Interband-Kopplung sind. Der vorgeschlagene Mechanismus könnte eine Erklärung für unerwartete Oszillationsfrequenzen in der Literatur geben und als Probe für die Kopplung zwischen verschiedenen Teilen der Fermi-Fläche in einer großen Menge verschiedener Materialklassen dienen.

Contents

List of Abbreviations

ARPES	Angle-resolved photoemission spectroscopy
BZ	Brillouin zone
CMC	Common mode choke
CPO	Chemical potential oscillations
DFT	Density functional theory
dHvA	De Haas-van Alphen
DOS	Density of states
FFT	Fast Fourier transform
FS	Fermi surface
FSD	Fermi surface degeneracy
FWHM	Full Width at Half Maximum
IVC	Inner vacuum chamber
LCC	Leadless chip carrier
LK	Lifshitz-Kosevich
MB	Magnetic breakdown
MI	Magnetic interaction
MISO	Magneto-intersubband oscillations
MR	Magnetoresistance
NP	Nodal plane
OFHC	Oxygen-free high-conductivity
QI	Quantum interference
QO	Quantum oscillation
QPI	Quasiparticle interference
QPL	Quasiparticle lifetime
RRR	Residual resistivity ratio
SdH	Shubnikov-de Haas
SG	Space group

SOC	Spin-orbit coupling
SQUID	Superconducting quantum interference device
TP	Topological protectorate
UHV	Ultra-high vacuum
X-ray	Röntgen radiation

1 Introduction

1.1 Motivation

The properties of crystalline materials fundamentally depend on their electronic structure. It does not only determine the electrical transport properties but manifests itself in almost all physical observables including the thermal conductivity, heat capacity, magnetic susceptibility, and the optical properties. A detailed understanding of the electronic structure therefore plays a key role in the explanation of interesting phenomena such as charge density wave phases [1, 2] and unconventional superconductivity [3, 4]. Moreover, the prediction of material properties from their electronic structure enables the systematic search for materials tailored to specific applications, which have found use in numerous fields ranging from the semiconductor industry over materials science to sensor technology.

The behavior of electrons in a periodic lattice is distinctly different from that of a free electron gas. The permitted states are confined to energy bands as a result of the interaction between conduction electrons and the ion cores of the underlying crystal lattice. The band structure describes the energy spectrum, which is determined by the crystal structure, the interaction potential, and the wave vector of the electrons. Its characteristics are used in the explanation of many material properties. For instance, the classification of a material as an electrical conductor can be inferred from its band structure featuring partially filled bands [5]. In contrast, semiconductors and insulators feature only completely filled and completely empty bands, which are separated by a narrow or a large gap, respectively. Furthermore, the allowed transitions between occupied and empty states dominate the optical properties [6, 7] and the deviation of the energy dispersion of conduction electrons from that of the free electron gas explains the existence of positive Hall coefficients [8, 9]. Underlying all of these explanations is the notion that electrons in a crystalline lattice can be adequately described in terms of quasiparticles with renormalized properties, whose characteristics are determined by the band structure.

Initial calculations of band structures were performed using exactly solvable models, which provide a tractable description of simple systems, such as the noble metals. The development of density functional theory paved the way for numerical calculations of the electronic ground state [10] and advancements in computational power have enabled their utilization in the prediction of the electronic structure of complex

materials. Nevertheless, a precise calculation of the resulting energy spectrum from first principles remains a challenge and experimental studies are essential for the determination of the electronic band structure, particularly in materials with strong correlations.

With the realization by Sir Michael Berry that the electron wave functions carry a geometrical phase which has physical relevance [11], it became evident that a reduced description focusing on the eigenenergies alone does not provide a full picture. Instead, an approach using the geometric properties, which are described in the language of topology, has proven to be highly successful in elucidating various physical phenomena [12–16] and has led to the classification of materials based on their topological properties [17–19]. Topology is a branch of mathematics concerned with the continuous deformation of geometric objects. Properties that remain unchanged through these deformations, such as the number of twists in a Möbius strip or the number of holes in a donut, are known as topological invariants. Underlying the topology of the band structure is the so-called Berry curvature [11], which is a local description of the geometric properties of the electronic eigenstates. The Chern theorem [20] states that the integral of the flux of Berry curvature over a closed manifold, such as a sphere or torus, is quantized in units of 2π. The associated topological invariant is known as the Chern number [21].

Following the interpretation of the integer quantum Hall effect in terms of a series of topological phase transitions [12, 13], the classification of materials based on their topology gained momentum with the prediction and discovery of topological insulators [22–26]. These materials have been experimentally identified primarily based on their non-trivial surface states, whose ultrahigh mobilities and large magnetoresistance effects have sparked interest in their use for technological applications [27]. Soon after, it was realized that the bulk electronic states in three-dimensional Weyl and Dirac semimetals [28–35] feature band degeneracies with linear dispersions. The low-energy excitations around these degeneracies mimic elementary particles described by the Weyl and Dirac equations. The distinction between the two types of materials is related to the symmetries of their crystal structure. In Dirac semimetals, both time-reversal and spatial inversion symmetry are upheld, leading to a twofold degeneracy of every electronic state due to Kramer's theorem [36]. If either of these symmetries is broken, the twofold degeneracy is lifted, and a Weyl semimetal may emerge. In Weyl semimetals, the crossing points occur in pairs of different handedness, which is characterized by the sign of the associated Chern number. In contrast, Dirac

crossings can be thought of as a pair of Weyl nodes positioned on top of each other. Hence, they carry no net topological charge. Consequently, Dirac crossings are not topologically protected and the emerging behavior is profoundly different for the two material classes.

The non-trivial topological properties of Weyl semimetals gives rise to a multitude of interesting physical phenomena. One of the most spectacular features, widely used in the identification of Weyl semimetals, is the presence of Fermi arc surface states, which have been observed in numerous different materials [28, 37, 38]. They arise from the bulk-boundary correspondence [39, 40] and connect the projections of Weyl nodes in the bulk electronic structure to the surface Brillouin zone, analogous to the conducting surface states in topological insulators. The chiral nature of the Weyl crossing points can give rise to the chiral magnetic effect [41, 42]. It has been predicted to manifest itself in the transport properties of Weyl semimetals as a negative longitudinal magnetoresistance, which has been experimentally observed in TaAs [43, 44]. However, it is possible that other effects might give rise to a similar phenomenology [45]. The optical responses of Weyl semimetals also exhibit signatures of their band topology, which manifest themselves as an ω-linear optical conductivity for interband transitions in the vicinity of the Weyl nodes [46–48]. Non-linear responses, such as the quantized circular photogalvanic effect [49–51], can emerge for Weyl nodes located at different energies. Other phenomena induced by the non-trivial band topology include the intrinsic anomalous Hall effect in magnetic Weyl semimetals [52–54], the intrinsic spin Hall effect in inversion symmetry breaking materials [55], and a π Berry phase in quantum oscillations under certain conditions [56–59].

The strength of topological responses critically depends on the following factors. First, because most response functions scale with the Berry curvature the charge of topological defects, i.e., their Chern number, is directly proportional to the strength of the topological response. Furthermore, most physical properties are dominated by the electronic structure in the vicinity of the Fermi level. Thus, topological response functions are expected to be especially strong if the topological defects are located energetically close to the Fermi level or equivalently close to the Fermi surface in reciprocal space. Lastly, the presence of topologically trivial states at the Fermi level may outweigh the influence of topological degeneracies in some materials. Therefore, in order to observe strong topological responses a band structure with no trivial states at the Fermi energy is desirable.

A recent systematic analysis of the symmetries of all 230 space groups identified higher-order crossings beyond Dirac and Weyl points featuring large Chern numbers [60, 61]. Because fermions in condensed matter systems are not constrained by the Poincaré symmetry of free space, the low-energy spectrum in the vicinity of these crossing points results in the emergence of fermionic excitations with no counterpart in particle physics potentially exhibiting novel properties. The large Chern numbers associated with these crossing points are predicted to give rise to substantial topological responses. These prospects initiated intense research activity on materials featuring multifold crossing points, both from the theoretical [50, 62–67] and experimental side [68–72].

The family of non-magnetic B20 compounds, crystallizing in the simple cubic space group (SG) 198, has proven to be an especially fruitful material class for the investigation of multifold crossings [73–92]. Their representatives include the transition metal silicides and germanides CoSi, RhSi, CoGe, and RhGe, as well as PdGa and PtAl [93]. All of these compounds feature multifold symmetry-enforced crossings at high-symmetry points of the Brillouin zone. Their location with respect to the Fermi energy and the dispersion of the bands around them differs between the compounds. However, the multifold crossing points are not the only symmetry-enforced degeneracies in SG 198. There are entire planes in reciprocal space located at the BZ boundary on which pairs of bands are enforced to be degenerate and movable Weyl points along high-symmetry lines [94, 95]. These additional degeneracies have a profound impact on the global topology of the band structure.

In many materials topological defects appear in pairs with opposite topological charge, satisfying the Nielsen-Ninomiya no-go theorem [96–98]. A simple argument that explains why Weyl points appear in pairs relies on the fact that the Chern number of a 2D slice through the BZ changes by ± 1 when it is moved across a Weyl point. Due to the periodicity of the BZ another Weyl point with opposite charge must exist. Recently, it was realized that this argument holds true only if there exist fully gapped slices through the BZ on which the Chern number is well defined. Since the symmetries of SG 198 enforce band degeneracies on the entire BZ boundary, called nodal planes (NPs), this condition is not given in this material class. The NPs open up the possibility of Weyl points with no partner in the interior of the BZ whose charge is compensated by the NPs on the BZ boundary [99]. The observation of topologically non-trivial NPs in the field-polarized phase of MnSi [100] raises the question whether their influence can also be seen in its non-magnetic counterparts

and more generally, whether a description of the band topology in B20 compounds focusing on pairs of isolated band degeneracies is warranted.

In the work presented here, we report on our experimental studies on the semimetallic compound CoSi. We used quantum oscillations as a probe for the band structure. First observed by de Haas and van Alphen as variations in the magnetic susceptibility of bismuth [101], they are periodic oscillations of physical observables as a function of the inverse magnetic field. This effect is not limited to the magnetization but has been observed in numerous material properties, including the electrical resistivity [102–107], specific heat [108–110], magnetostriction [111–115], thermal conductivity [116, 117], or ultrasonic attenuation [118–120]. Quantum oscillations have proven to be a valuable tool in the determination of the Fermi surface (FS) of metallic systems [121], as evidenced by their use in uncovering the electronic structure of a wide range of materials, including elemental metals such as silver and gold [122, 123], unconventional superconductors [124, 125], and heavy fermion systems [126, 127].

A comprehensive theoretical description following the semi-classical arguments by Onsager [128] has been established by Lifshitz and Kosevich [129]. Under the influence of a magnetic field, the permitted electronic states in reciprocal space perpendicular to the field are confined to isoenergy contours known as Landau tubes. The size and degeneracy of these tubes depends on the magnetic field strength. Whenever a Landau tube leaves the zero-field FS, the electrons redistribute onto the next lower Landau tube leading to an abrupt change in the thermodynamic potential, that manifests itself in changes in nearly all physical observables. The frequency at which these changes occur provides valuable insight into the FS geometry. Further characteristics of quantum oscillations offer additional information about the properties of the involved quasiparticles. The temperature dependence of the oscillation amplitudes is, for example, related to their cyclotron mass and correspondingly the band dispersion at the Fermi level. The evolution of oscillation amplitudes with the strength of the magnetic field can be used to infer the quantum lifetime.

In general, the finite quasiparticle lifetime manifests itself distinctively in different material properties. A well-known example is the difference between quantum lifetimes extracted from quantum oscillation studies and the transport lifetimes which can be obtained from the Hall mobility [130–133]. The ratio between the two lifetimes yields insights into the relevant scattering mechanisms whose microscopic determination and characterization remains one of the ongoing efforts in modern condensed matter

physics [134–136]. One of the key challenges is that most probes are only sensitive to the average over all scattering events, rendering it difficult to disentangle individual contributions.

In complex metallic systems featuring multiple FS pockets arising from different bands the resulting quantum oscillation spectrum is typically described by a superposition of individual oscillation frequencies. The interpretation of the quantum lifetime follows the same idea and is typically analyzed separately for each individual frequency [132, 133]. This approach provides further insight into the relevant scattering mechanisms for distinct parts of the Fermi surface but neglects mutual interactions between them.

There are amendments to the standard theory of quantum oscillations describing how different frequencies may influence each other. However, they are mostly based on a feedback from oscillations arising from one part of the FS on the oscillations arising from another while remaining in the independent-band picture. Interactions between electronic states are typically only taken into account by a renormalization of the band properties in the framework of Fermi liquid theory. This raises the question if there are effects beyond the independent-band picture that give us direct access to probe the interaction between different parts of the Fermi surface. As one of the main results of this thesis, we report on the observation of quantum oscillations in CoSi that cannot be explained by a simple renormalization of individual bands but instead imply a coupling of electronic states on a fundamental level.

1.2 State of the art

Following the prediction of multifold, symmetry-enforced, crossing points in the band structure of compounds crystallizing in SG 198 [60, 73], there have been several studies probing the electronic structure of CoSi. Here, we summarize the key observations of these studies and discuss their results with respect to the band topology, the role of spin-orbit coupling (SOC), and the influence of nodal planes located on the BZ boundary.

Angle-resolved photoemission spectroscopy (ARPES) was used in CoSi to probe the bulk dispersion and look for signs of Fermi arcs in the surface states [79–81]. Bulk sensitive measurements using soft X-rays confirmed the rough band structure predicted by density functional theory (DFT) [73, 75]. Due to the limited energy resolution in these studies, fine details of the band structure, such as the open question about a SOC-induced splitting of the bands, could not be resolved. By probing the

surface electronic structure using vacuum ultraviolet radiation, Fermi arc surface states connecting projections of the multifold crossing points located at the Γ- and R-points onto the surface BZ were detected, thereby confirming their topologically non-trivial nature. From the number of observed Fermi arcs a topological charge of ± 2 for the crossing points was inferred and taken as evidence that SOC is negligible in CoSi. However, due to the limited resolution of ARPES, a splitting of the individual Fermi arcs may have not been resolved.

An alternative approach to probe the surface electronic structure by recording quasiparticle interference (QPI) patterns was used in Ref. [137]. The authors attribute some of the features they observe to Fermi arc surface states. Since these features always appear in pairs in the dispersions taken along different cuts through the surface BZ, the authors conclude that there is a SOC induced band splitting on the order of 25 meV and 35 meV at the Fermi energy.

Additionally, optical conductivity studies were performed looking for signatures of multifold fermions [82, 90]. The authors compare their experimental results to calculations using the band structure obtained from DFT and find that their data is best explained if SOC is included in the calculations.

Several studies report on quantum oscillations in the magnetothermopower [138], magnetoresistance [139–141] and magnetization [141, 142]. We summarize their main findings and interpretations in the following and comment on their consistency with our results.

In the earliest QO studies reported in Refs. [138, 139], two oscillation frequencies at approximately 565 T and 665 T are observed. The reported dependence of the oscillation frequencies on the angle of the applied magnetic field is small, indicating nearly spherical Fermi surface pockets as their origin. An analysis of the temperature dependence of the oscillation amplitudes yields effective masses between $0.8\,m_e$ and $1.2\,m_e$. The authors link the detected frequencies to the FS of CoSi around the R-point and conclude that the observation of two frequencies is a sign that there is no SOC-induced splitting of the bands. As we shall see later, this interpretation does not take the role of symmetry-enforced degeneracies at the nodal planes into account correctly.

A subsequent study reported in Ref. [142] confirms these two frequencies, but attributes an asymmetrical shape of the observed Fourier peaks to a SOC-induced

splitting of the bands. Again, this conclusion does not take the nodal planes into account and the interpretation of the peak asymmetry as a small splitting of the frequencies would indicate a band splitting that is much smaller than anticipated by calculations including SOC. The reported effective masses of $0.36\,m_e$ and $0.37\,m_e$ differ by almost a factor of three from the otherwise consistent reports in the literature and our results. Additionally, the authors detect slow oscillations with a frequency of 20 T and a light effective mass of $0.11\,m_e$. This oscillation frequency also exhibits almost no angular dispersion and is attributed to a small FS pocket located around the Γ-point. However, the authors infer an unrealistically large upward band shift of 45 meV, which would correspond to a substantial hole doping of their samples that is not reflected in the frequencies detected for the FS pockets around the R-point.

Ref. [141] reports on the two frequencies at 558 T and 663 T with effective masses ranging between $0.85\,m_e$ and $1.11\,m_e$. The authors correctly attribute these frequencies to the electron pockets around the R-point, but do not comment further on the role of SOC. They also observe the slow frequency at 18 T with an effective mass of $0.16\,m_e$ and attribute it to a small hole pocket around the Γ-point.

A magnetotransport study on microstructures of CoSi, performed in parallel to our work, is reported in Ref. [140]. The two frequencies arising from the FS pockets around the R-pocket are reported at ≈550 T and ≈660 T with cyclotron masses of $\approx 0.84\,m_e$. In their analysis, the authors consider the band structure including SOC and correctly take into account the symmetry-enforced band degeneracies at the BZ boundary. They further argue that there are quasi-symmetry protected near degeneracies with an energy gap no larger than 2 meV in the vicinity of the R-point, at which quasiparticles tunnel between orbits through magnetic breakdown. The calculated breakdown field is below 0.11 T for any field direction, rendering the gap completely transparent at magnetic field strengths at which quantum oscillations are observed. The authors compare their experimental data to calculations for extremal orbits that take into account both the exact degeneracies at the NPs and full magnetic breakdown at the quasi-symmetry protected near crossings, yielding a consistent explanation between experiment and theory.

In summary, there have been a number of optical spectroscopy and quantum oscillation studies on CoSi. The QO studies consistently report the detection of two almost dispersionless frequencies at ≈560 T and ≈660 T with cyclotron masses of $\approx 1\,m_e$. A low oscillation frequency at ≈20 T with an effective mass of $\approx 0.15\,m_e$, which

also exhibits almost no angular dispersion, is detected in two studies on the dHvA effect. There are conflicting interpretations in the literature regarding the role of SOC. Moreover, the proposed Fermi surface trajectories around the R-point in most studies did not take into account the enforced degeneracies on the NPs correctly. Although there are multiple FS pockets centered around the Γ-point predicted by DFT calculations, there was only one quantum oscillation frequency related to this part of the FS observed experimentally, which was not attributed correctly to the calculated band structure.

1.3 Structure of this thesis

In Chapter 2, we provide an overview of the theoretical concepts relevant for the work presented in this thesis. We give a brief overview of how crystalline symmetries can enforce degeneracies in the band structure in Sec. 2.1. We then discuss the basic ideas of band topology. Section 2.2 describes the crystal and band structure of CoSi and the influence of SOC on the band structure. We summarize the theory of quantum oscillations in Sec. 2.3 and discuss various mechanisms leading to combination frequencies in quantum oscillatory spectra in Sec. 2.4.

Chapter 3 summarizes the experimental methods employed in the course of this work. Section 3.1 provides a description of the single-crystal preparation process and a comparison of the samples investigated in this thesis. Section 3.2 presents an overview of the cryogenic system, which has been utilized for the majority of the measurements presented here. The integration of cryogenic wiring and the use of low-pass filters and signal transformers, which are essential for the high signal-to-noise ratio of our experiments, are discussed in detail. Different measurement techniques have been used in this thesis to probe the electric and magnetic properties of CoSi. The underlying physical principles and technical realizations of the measurement setups are presented in Section 3.3. The chapter concludes with a detailed step-by-step description of the procedure employed in the analysis of our quantum oscillatory data in Section 3.4.

In Chapter 4, we discuss the Fermi surface determination of CoSi through measurements of the Shubnikov-de Haas (SdH) and de Haas-van Alphen (dHvA) effects. We begin with an overview of the magnetic and electric properties of CoSi in Section 4.1. The presentation of our quantum oscillation studies is divided into two parts. In Section 4.2 we focus on the part of the SdH spectrum that arises from the FS pockets centered around the R-point. We discuss our results with regards to the relevance

of spin-orbit coupling and the role of nodal planes on the Brillouin zone boundary. In Section 4.3, we report on SdH and dHvA oscillations in a sample with improved crystalline quality. The oscillations feature additional frequencies, which arise from heavier FS pockets situated around the Γ-point. We discuss our findings with respect to the global band topology of CoSi in Section 4.4 and conclude with an outlook on current projects in our group.

One of the central results of this thesis, presented in Chapter 5, is the observation of combination frequencies in the quantum oscillation spectra of CoSi, which are not explained by the conventional theory and its amendments. Section 5.1 presents a detailed analysis of these frequencies with regards to their angular dispersion, phase relation to the underlying frequencies and unusual temperature-dependent damping. The observed characteristics are then compared to conventional mechanisms in Section 5.2, which are known to lead to combination frequencies in quantum oscillation spectra. It is shown that these mechanisms do not account for our experimental observations. Finally, we present a theory explaining our findings through quantum oscillations of the quasiparticle lifetime in the presence of interband coupling in Section 5.3. We then discuss the generality of our proposed mechanism and present examples of experimental observations in the literature exhibiting a phenomenology similar to the one observed in CoSi.

We summarize the main results of this thesis in Chapter 6 and discuss their implications in a broader context.

2 Theoretical Background

In this Chapter, we present the basic theoretical concepts relevant for the work performed in the course of this thesis. We begin with a discussion of the relation between crystalline symmetries and degeneracies in the band structure and their classification by topological invariants in Sec. 2.1. The concepts are applied to the crystal and band structure of CoSi in Sec. 2.2. The theory of quantum oscillations is briefly recapitulated in Sec. 2.3, followed by a discussion of mechanisms known to give rise to combination frequencies in quantum oscillatory spectra in Sec. 2.4.

2.1 Symmetry and topology

Following the famous theorem by Wigner and von Neumann [143] electronic bands with the same symmetry cannot be degenerate at generic points in the Brillouin zone (BZ) and form avoided crossings at points in k-space where they approach each other. However, for bands with topologically non-trivial character degeneracies can be protected by their topology and crossing points, lines or entire planes may emerge [144, 145]. We can group these degeneracies into two categories which are closely linked to the underlying crystal symmetries. The first are accidental crossings which may exist in a material with a given set of symmetries but are not stable under large symmetry-preserving transformations [146, 147]. The second category comprises symmetry-enforced degeneracies which cannot be removed by symmetry-preserving changes of the Hamiltonian, i.e., they are stable under variations of the chemical composition or other material specific details [30, 148, 149]. In this section, we discuss both types of band crossings and their relation to the crystalline symmetries. We focus on three-dimensional materials and the zero- and two-dimensional defects relevant for the band structure of CoSi and show how they can be classified by their Chern number. A comprehensive account of crossings in further dimensionalities and the full classification of the relevant symmetries is given in Refs. [144, 150]. The explanations presented below follow the treatment given in Ref. [150].

We begin our discussion with accidental band crossings which may exist if bands with non-trivial topology and/or opposite symmetry overlap. Accidental crossings are protected by symmorphic and/or non-spatial symmetries. Symmorphic symmetries are symmetries that leave at least on point in real space invariant, such as rotations or inversions. Non-spatial symmetries are symmetries that act locally in real space, such as time-reversal or particle-hole symmetry. Accidental band crossings may

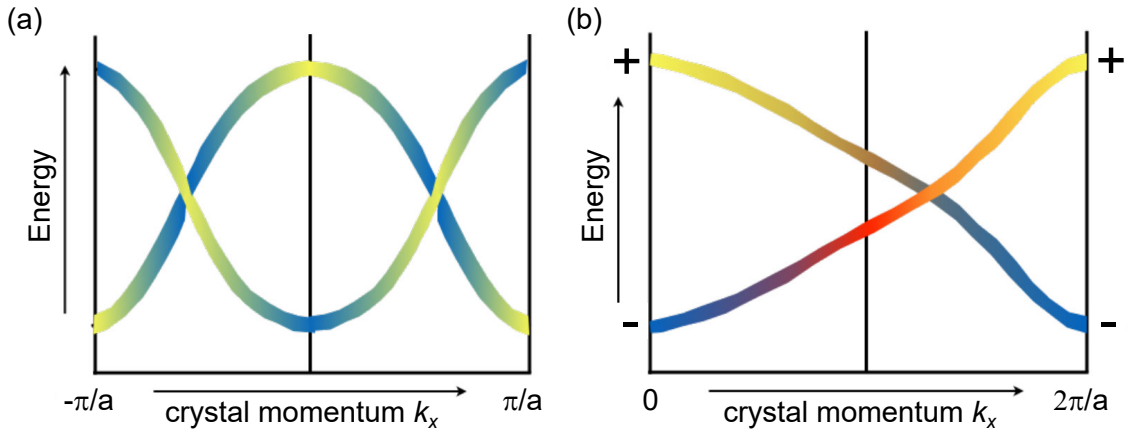

Figure 2.1: Types of band crossings. (a) Accidental band crossings. If two bands of different symmetry overlap, they form two band crossings. The shading indicates a $\boldsymbol{k}$-dependent pseudo-spin degree of freedom which is orthogonal at the crossing points for the two intersecting bands. (b) Movable band crossing protected by a non-symmorphic symmetry. The color shading indicates the eigenvalue of the non-symmorphic symmetry operator which switches sign after crossing the full BZ. Figure adapted from Ref. [150].

occur at general positions in the BZ because of the different symmetry of the involved bands as shown in Figure 2.1 (a). They can be moved by small symmetry-preserving perturbations but are protected in the sense that these perturbations cannot remove them by opening up a gap. However, large perturbations may remove the band crossings entirely, e.g., by annihilation of two crossing points with opposite topological charge. Therefore, for a given crystalline symmetry it can only be inferred that accidental band crossings are possible but not if they are actually realized in a particular material. Weyl points at arbitrary points in the BZ are a typical example of accidental band crossings.

The second category of band degeneracies are symmetry-enforced crossings which are required to exist by symmetry alone. They can further be divided in movable and non-movable band crossings with the latter being realized if the degeneracy is enforced at a high-symmetry point or an entire plane of the BZ. Symmetry-enforced band crossings are protected by non-symmorphic symmetries [148]. A non-symmorphic symmetry $G = \{g|\boldsymbol{t}\}$ combines a n-fold point group symmetry g, such as rotation or reflection, with a translation $\boldsymbol{t}$ by a fraction p/n of a Bravais lattice vector $\boldsymbol{a}$, where $p \in \{1,2,\ldots,n-1\}$. Examples for non-symmorphic symmetries include screw rotation axes and glide reflection planes.

We first focus on movable crossing points and consider spinless quasiparticles, i.e., Bloch electrons without spin-orbit coupling, for simplicity. Following Ref. [150], the

lattice translation operator $T_{\boldsymbol{a}}$ belonging to the lattice vector $\boldsymbol{a}$ can be constructed by applying the non-symmorphic symmetry n times, i.e.,

$$G^n = \{g^n | n\boldsymbol{t}\} = pT_{\boldsymbol{a}} \ . \tag{2.1}$$

The enforcement of a crossing point can be understood by considering how the eigenvalues of G change as a function of crystal momentum $\boldsymbol{k}$ in the space left invariant by g. In these lines or planes we can construct Bloch states $|\psi_m(\boldsymbol{k})\rangle$ which are both eigenfunctions of G and the Hamiltonian of the system. By applying G^n to $|\psi_m(\boldsymbol{k})\rangle$, we find

$$G^n \, |\psi_m(\boldsymbol{k})\rangle = e^{-ip\boldsymbol{k}\cdot\boldsymbol{a}} \, |\psi_m(\boldsymbol{k})\rangle \ . \tag{2.2}$$

The eigenvalues of G are then given by

$$G \, |\psi_m(\boldsymbol{k})\rangle = e^{i2\pi m/n} e^{-ip\boldsymbol{k}\cdot\boldsymbol{a}/n} \, |\psi_m(\boldsymbol{k})\rangle \ , \tag{2.3}$$

where $m \in \{0,1,\ldots,n-1\}$.
For concreteness we consider the case of a two-fold screw rotation axis $\tilde{C}_2^x$ along k_x. From Eq. (2.3) it follows that

$$G \, |\psi_m(\boldsymbol{k})\rangle = \begin{cases} +e^{-ik_x \cdot a/2} \, |\psi_m(\boldsymbol{k})\rangle \ \text{ for } m = 0 \ , \\ -e^{-ik_x \cdot a/2} \, |\psi_m(\boldsymbol{k})\rangle \ \text{ for } m = 1 \ . \end{cases} \tag{2.4}$$

The eigenvalues along a $\tilde{C}_2^x$-invariant line are shown in Figure 2.1 (b). For a particular band they change sign after translation through a full BZ. Consequently, to get back to the same eigenvalue the BZ needs to be crossed twice (or in the general case n times). Due to the fact that the $|\psi_m(\boldsymbol{k})\rangle$ are simultaneously eigenfunctions of the Hamiltonian the eigenenergies of a pair of bands are also interchanged by a translation by $2\pi/a$. In the absence of further degeneracies the two bands therefore must cross an odd number of times as they cross the BZ. Without additional symmetry constraints the location of these crossings depends on the band dispersions with the only restriction being that they lie along lines or planes that are invariant under the non-symmorphic symmetry G protecting them. Hence, they are called movable band crossings. Examples for movable band crossings include Weyl nodal lines protected by glide reflection symmetry and Weyl points protected by screw rotation axes [151].

In the presence of additional symmetries band crossings can be pinned to particular points, lines or planes in the BZ. An example for this is Kramers' degeneracy in

systems with time-reversal symmetry $\mathcal{T}$. It follows directly from the fact that for every Bloch state $|\psi(\boldsymbol{k})\rangle$ there exists another Bloch state at $|\psi(-\boldsymbol{k})\rangle$ with the same energy [36]. Consequently, if $\boldsymbol{k}$ is a time-reversal invariant momentum, there is a Kramer's degeneracy. In the following we will focus on a symmetry-enforced band crossing pinned to an entire plane in reciprocal space. We will explain how the combination of time-reversal symmetry $\mathcal{T}$ and a two-fold screw rotation axis $\tilde{C}_2$ enforces a band degeneracy at the BZ boundary, called a nodal plane (NP) [94, 100].

We consider the symmetries of space group 198 in which CoSi, the material investigated in this thesis, crystallizes (cf. Fig. 2.3). It lacks inversion, mirror or roto-inversion symmetries but features time-reversal and two-fold screw-rotation symmetries along all three equivalent directions x, y, and z. For concreteness, we focus on the x-direction in the following. We consider spinful quasiparticles described by their Bloch wave functions $|\psi(\boldsymbol{k})\rangle$.

The two-fold screw rotation symmetry along x acts on the real-space coordinates and the spin part of $|\psi(\boldsymbol{k})\rangle$ as

$$\tilde{C}_2^x \equiv \{C_2^x|\tfrac{1}{2}\tfrac{1}{2}0\} \;:\; (x,y,z) \to (x+\frac{1}{2}, -y+\frac{1}{2}, -z) \otimes (i\sigma_x) \;, \tag{2.5}$$

where σ_x is the first Pauli matrix. Time-reversal symmetry can be expressed by

$$\mathcal{T} \equiv i\sigma_y \mathcal{K} \;, \tag{2.6}$$

where σ_y is the second Pauli matrix acting on the spin and $\mathcal{K}$ is the complex conjugation operator. In reciprocal space the combination of both symmetries effectively maps $\boldsymbol{k}$-points to

$$\mathcal{T}\tilde{C}_2^x \;:\; (k_x, k_y, k_z) \to (-k_x, k_y, k_z) \;, \tag{2.7}$$

acting like an effective mirror symmetry which leaves points at $k_x = 0$ and $k_x = \pi$ invariant.

The effect of the combined symmetries is illustrated in Fig. 2.2 (a). It can be shown that this combined symmetry is anti-unitary which can be used to derive the existence

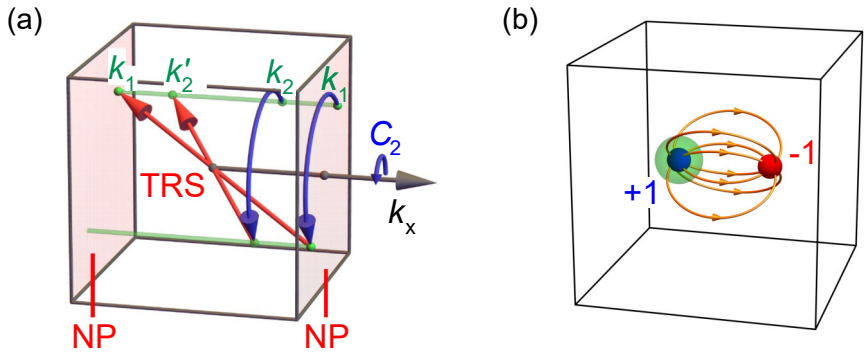

Figure 2.2: Nodal planes and Weyl points. (a) The combination of a screw rotation axis C_2 and time-reversal symmetry (TRS) enforces a nodal plane (NP) on the BZ boundary. Panel adapted from Ref. [100]. (b) Schematic depiction of two Weyl points with opposite charge. Lines indicate the flux of Berry curvature from one node to the other. The Chern numbers can be calculated by integrating the Berry curvature over a sphere (green) enclosing the Weyl node.

of Kramers' degeneracy at $k_x = \pi$. If we consider the square of $\mathcal{T}\tilde{C}_2^x$ and let it act on a Bloch state we obtain

$$\left[\mathcal{T}\tilde{C}_2^x\right]^2 = T_{(1,0,0)} = e^{ik_x} = \begin{cases} +1 \text{ for } k_x = 0 \ , \\ -1 \text{ for } k_x = \pi \ . \end{cases} \tag{2.8}$$

Within the $k_x = \pi$ plane $\mathcal{T}\tilde{C}_2^x$ consequently acts like a time reversal symmetry that squares to -1. Due to Kramers' theorem [36] all states in this plane are therefore at least twofold degenerate. Due to the lack of inversion symmetry in SG 198 the degeneracy is lifted at arbitrary points in the BZ and therefore there exist symmetry enforced band crossings at the entire $k_x = \pi$ plane. The same arguments hold true for the screw rotations $\tilde{C}_2^y$ and $\tilde{C}_2^z$ along the y and z crystallographic directions, enforcing a trio of nodal planes on the entire BZ boundary.

The band crossings described above may be further characterized by their topology. For this, we first introduce the concept of Berry curvature [11]. As we shall see, band degeneracies can act as monopoles of Berry curvature quantified by a topological invariant known as the Chern number [20]. We then discuss how the Chern number can be calculated for point-like crossings and the nodal planes discussed above. Comprehensive reviews on topological aspects of the band structure can be found in Refs. [16, 21].

We consider a generic band structure described by

$$\mathcal{H}\left|\psi_m(\boldsymbol{k})\right\rangle = E_m\left|\psi_m(\boldsymbol{k})\right\rangle \ , \tag{2.9}$$

where $\mathcal{H}$ is the Hamiltonian of the system and $|\psi_m(\boldsymbol{k})\rangle$ are the Bloch wavefunctions. When the eigenstate $|\psi_m(\boldsymbol{k})\rangle$ is adiabatically moved along a path $\mathcal{C}$ in $\boldsymbol{k}$-space it picks up a phase

$$\gamma_m = \int_{\mathcal{C}} d\boldsymbol{k}\cdot\mathcal{A}_m(\boldsymbol{k}) \ , \tag{2.10}$$

where $\mathcal{A}_m(\boldsymbol{k})$ is the Berry connection [11] given by

$$\mathcal{A}_m(\boldsymbol{k}) = \left\langle\psi_m(\boldsymbol{k})\right| i\nabla_{\boldsymbol{k}}\left|\psi_m(\boldsymbol{k})\right\rangle \ . \tag{2.11}$$

The Berry connection is gauge dependent and thus does not correspond to an observable in physical properties. However, if we consider the phase accumulated along a closed loop

$$\gamma_m = \oint_{\mathcal{C}} d\boldsymbol{k}\cdot\mathcal{A}_m(\boldsymbol{k}) \ , \tag{2.12}$$

it can be proven that this so-called Berry phase is gauge invariant up to an integer multiple of 2π and therefore a physical observable.

The Berry curvature vector $\boldsymbol{\Omega}_m(\boldsymbol{k})$ is defined by

$$\boldsymbol{\Omega}_m(\boldsymbol{k}) = \nabla_{\boldsymbol{k}}\times\mathcal{A}_m(\boldsymbol{k}) \ . \tag{2.13}$$

Intuitively, the Berry curvature can be understood as the analog of a magnetic field in $\boldsymbol{k}$-space arising from the vector potential $\mathcal{A}_m(\boldsymbol{k})$. Using Stokes' theorem, the Berry phase can then be expressed as

$$\gamma_m = \int_{\mathcal{S}} d\boldsymbol{S}\cdot\mathcal{A}_m(\boldsymbol{k}) \ , \tag{2.14}$$

where $\mathcal{S}$ is an arbitrary surface enclosed by the path $\mathcal{C}$ and $\boldsymbol{S}$ is the normal vector on the surface.

The Berry curvature $\boldsymbol{\Omega}_m(\boldsymbol{k})$ can also be expressed as a summation over the eigenstates [11]

$$\boldsymbol{\Omega}_m(\boldsymbol{k}) = i\sum_{m'\neq m}\frac{\left\langle\psi_m\right|\nabla_{\boldsymbol{k}}\mathcal{H}(\boldsymbol{k})\left|\psi_{m'}\right\rangle\times\left\langle\psi_{m'}\right|\nabla_{\boldsymbol{k}}\mathcal{H}(\boldsymbol{k})\left|\psi_m\right\rangle}{(E_m(\boldsymbol{k})-E_{m'}(\boldsymbol{k}))^2} \ . \tag{2.15}$$

Because the denominator in Eq. (2.15) involves the difference between the energies of individual bands, the Berry curvature may become large where bands are energetically close to each other and may diverge at points where bands are degenerate.

In that sense, band degeneracies may act as monopoles, i.e., quantized sources or sinks of Berry curvature. We can characterize their topological charge by integrating the Berry curvature over a closed manifold $\mathcal{O}$ yielding

$$\frac{1}{2\pi}\int_{\mathcal{O}} d\boldsymbol{O}\cdot\boldsymbol{\Omega}_m(\boldsymbol{k}) = C \ , \tag{2.16}$$

where $\boldsymbol{O}$ is the normal vector on the surface and C is the integer Chern number. On the integration contour $\mathcal{O}$ the band with index m must not be degenerate with any other band, i.e., $\mathcal{O}$ must be a fully gapped region of the band structure. The quantization of Berry curvature given by the Chern number is responsible for various topological effects.

The Berry curvature and the associated Chern numbers have global constraints. First, the summation over the Berry curvature of all energy levels must vanish for each value of $\boldsymbol{k}$ [21]

$$\sum_m \Omega^m_{\mu\nu}(\boldsymbol{k}) = 0 \ . \tag{2.17}$$

Second, following the no-go theorem by Nielsen and Ninomiya [96, 97] the sum of all Chern numbers for a particular band index m has to add up to zero over the whole Brillouin zone

$$\sum_{\mathrm{BZ}} C = 0 \ . \tag{2.18}$$

Technical implementations for calculating the Chern numbers can be realized by using Eqs. (2.15) and (2.16) and the wave functions obtained from first-principles calculations [100, 152]. For crossing points located in the interior of the BZ the integration contour can be chosen as a small sphere enclosing the degeneracy [cf. Fig.2.2 (b)]. However, for degeneracies located on a nodal plane no fully gapped integration contour can be found. Therefore, the non-Abelian Berry curvature [75], which excludes the summation over degenerate bands in Eq. (2.15), has been used to calculate the non-Abelian Chern numbers for pairs of degenerate bands. For the trio of nodal planes located at the BZ boundary only the total charge is quantized. The Chern number for the trio of NPs has been calculated by integrating the Berry curvature over a cube slightly smaller than the BZ.

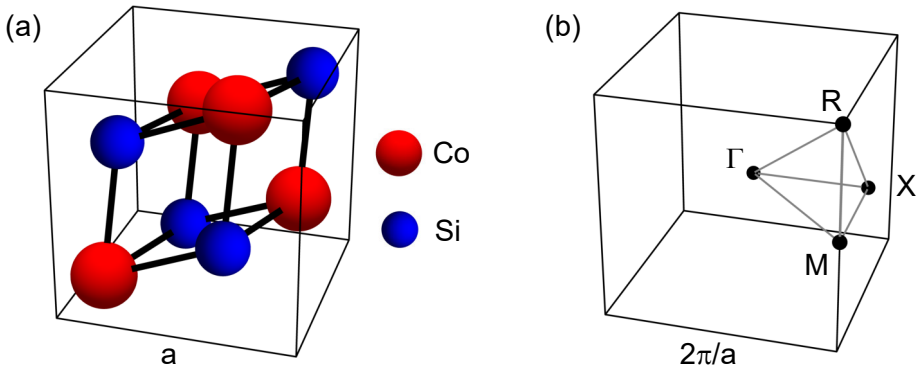

Figure 2.3: Crystal structure of CoSi. (a) Simple cubic unit cell with a lattice constant of a = 4.444 Å. (b) Reciprocal unit cell with points and lines of high symmetry.

2.2 Crystal and band structure

CoSi crystallizes in the non-symmorphic chiral space group 198 ($P2_13$) with an experimentally determined lattice constant of $a = 4.444$ Å [153]. The simple cubic unit cell containing four formula units is shown in Figure 3.1 (a). The Co and Si atoms occupy Wyckoff positions 4a with coordinates (u,u,u), $(-u+1/2,-u,u+1/2)$, $(-u,u+1/2,-u+1/2)$, and $(u+1/2,-u+1/2,-u)$, where $u_{\mathrm{Co}} = 0.143$ and $u_{\mathrm{Si}} = 0.844$. The reciprocal unit cell with points and lines of high symmetry indicated is shown in Fig. 3.1 (b).

The electronic band structure of CoSi was calculated from first principles using DFT in our group. The calculations were performed using WIEN2K [154] and QUANTUM ESPRESSO [155, 156] within the generalized gradient approximation [157]. We compare the band structures calculated without and with the inclusion of SOC and discuss the resulting Fermi surface in the following.

The band structure along high-symmetry lines without the inclusion of SOC is depicted in Fig. 2.4 (a). There is a total of four spin-degenerate bands crossing the Fermi level. Symmetry-enforced nodal planes on the BZ boundary are highlighted in blue shading. Because the symmetries enforce pairwise degeneracies on all three BZ boundaries in the x, y, and z direction, there exist two trios of NPs from the four bands around the Fermi level. The topological charges, or Chern numbers, of all degeneracies are given in curly brackets using the following notation: Chern numbers, including the spin-degeneracy of the bands, are given for each band, which is involved in the crossing, in order of increasing energy. For the multifold crossing point at R, the Chern number is not well defined because no closed integration contour around the crossing point can be found for which the energy spectrum is fully gapped.

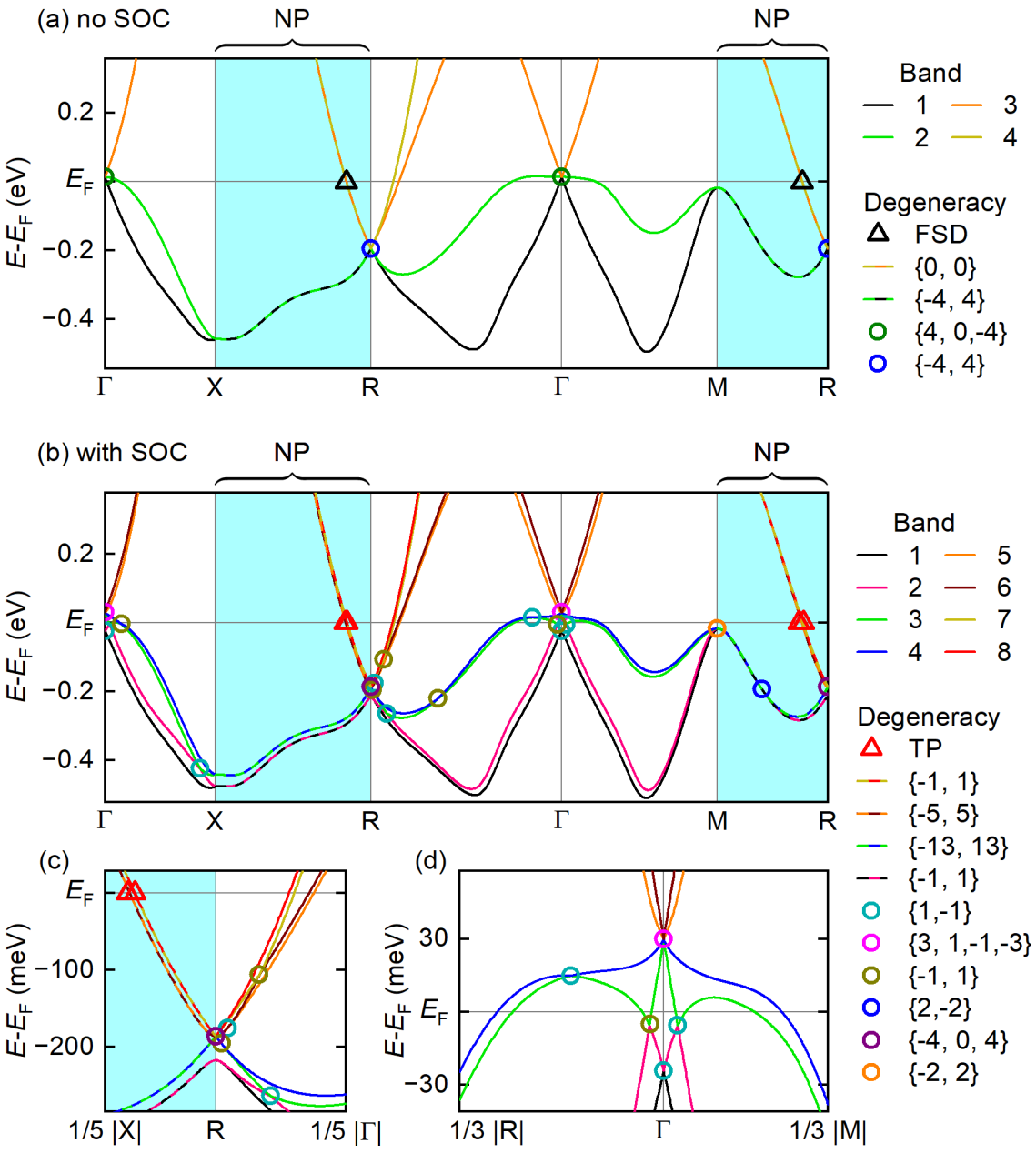

Figure 2.4: Electronic band structure of CoSi along high-symmetry directions. Calculated band structure without (a) and with (b) SOC. The BZ boundary hosting nodal planes (NPs) is indicated by blue shading. Fermi surface degeneracies (FSD) and topological protectorates (TP) are marked by triangles. Degenerate bands on the NP are marked by dashed lines. Topological crossing points are indicated by open circles. The numbers in curly brackets denote the topological charges of the involved bands in order of increasing energy (see text for details). (c), (d) Close-up views of the band structure including SOC surrounding the multifold crossing points located at R and Γ.

Therefore, the non-Abelian Chern numbers [75, 158] were calculated for every second band and are stated in curly brackets. Interestingly, because the upper trio of nodal planes intersects the Fermi level, there is an enforced degeneracy of the bands pinned to E_{F}, which we denote as Fermi surface degeneracy (FSD). We note that for the band structure without SOC the nodal planes are not enforced to, but may, carry a topological charge, as can be seen from the calculated topological charges of $\{0, 0\}$ for the upper trio of NPs and $\{-4, 4\}$ for the lower trio of NPs.

The relativistic band structure including SOC is depicted in Fig. 2.4 (b). Because the crystal structure of CoSi lacks inversion symmetry, spin degeneracy is lifted away from time-reversal invariant momenta and the four bands in the vicinity of the Fermi level split into eight. Correspondingly, the two trios of NPs split into four. Close-up views of the multifold crossing points located at R and Γ are shown in Fig. 2.4 (c) and (d), respectively. The fourfold crossing at R splits into a sixfold crossing with charge $\{-4, 0, 4\}$ and a topologically trivial twofold crossing. The threefold crossing at Γ splits into a fourfold crossing, carrying a charge of $\{3, 1, -1, -3\}$, and a Weyl point with a charge of $\{1, -1\}$. While there are further Weyl points located throughout the BZ, the singular Weyl point located at Γ has no symmetry-related partner [99, 159]. Because all other crossings in the interior of the BZ have symmetry-related copies with an even multiplicity, they cannot compensate the charge of the singular Weyl point. To satisfy the Fermion doubling theorem [96–98], this charge must be compensated by the only other degeneracy present, i.e., the nodal planes. Consequently, with the inclusion of SOC, the nodal planes are enforced to carry an odd topological charge, as reflected in the charges calculated from the DFT bands. Remarkably, unlike point-like degeneracies, there is no upper limit for the charge of the nodal planes. In the relativistic case, the degenerate bands forming the two nodal planes which are higher in energy, cross the Fermi level. These crossings occur on lines in k-space, which we denote as topological protectorates (TPs). With the enforced charge of the nodal planes, there is a generic mechanism pinning a large Berry curvature directly to the Fermi level, which may give rise to interesting topological responses of the system.

Next, we discuss the Fermi surface with and without SOC and examine the influence of NPs on the band connectivity. The Fermi surface contours calculated from the DFT band structure are presented in Figure 2.5.

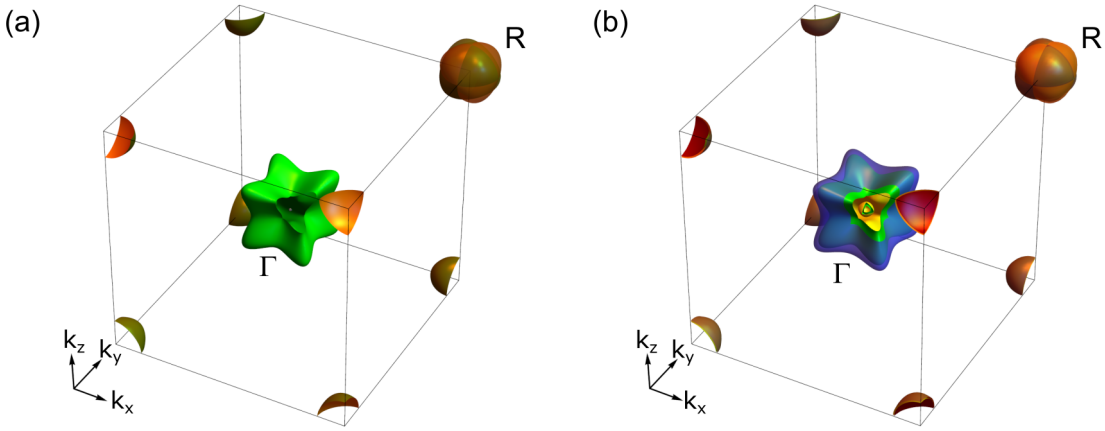

Figure 2.5: Fermi surface of CoSi. (a) Calculated FS without SOC. There are two intersecting electron-like FS pockets around the R-point and two hole-like pockets around the Γ-point. (b) Calculated FS with SOC. There are two pairs of intersecting FS sheets around the R-point. The FS around Γ consists of multiple nested sheets, which are discussed in detail in Sec. 4.3. One octant of the FS sheets around the Γ-point has been cut out and the outer sheet is drawn semi-transparent to allow for a view of the inner sheets. Neighboring BZs have been included for the pocket around the R-point in the upper right corner. Different colors represent the FS contours arising from different bands.

Without SOC, there are two hole-like FS sheets centered around the Γ-point. The small, nearly spherical pocket arises from the lower, linearly dispersing band depicted in Fig. 2.4 (a). The larger, cuboid-shaped pocket arises from a weakly dispersive band around the Γ-point. The bands around the R-point give rise to two electron-like FS pockets that intersect each other at the NPs.

With the inclusion of SOC, the bands and correspondingly the FS sheets split into pairs due to the non-centrosymmetric symmetry of SG 198. The Fermi surface pockets around the R-point intersect at the nodal planes on the BZ boundary and can be grouped into two pairs of pockets, which are discussed in detail in Sec. 4.2. The FS around the Γ-point is composed of several, multiply connected FS sheets which are the focus of Sec. 4.3.

2.3 Quantum oscillations

Quantum oscillations have been used as a powerful tool for the determination of the Fermi surface of metallic systems for almost a century. A comprehensive description is given in the textbook by D. Shoenberg [121]. In the following we briefly recapitulate the basic underlying principles.

A quantum mechanical description of conduction electrons in a metal under the influence of an external magnetic field $\boldsymbol{B}$ restricts the permitted states in $\boldsymbol{k}$-space to so-called Landau tubes. For a spherical Fermi surface with parabolic dispersion they form cylinders with a common axis parallel to $\boldsymbol{B}$, as illustrated in Figure 2.6. The crystal momenta perpendicular to the applied field are quantized to circles of constant energy

$$\varepsilon_r = \left(r + \frac{1}{2}\right) \frac{e\hbar B}{m^*} = \left(r + \frac{1}{2}\right) \hbar\omega_c \ , \tag{2.19}$$

where r is an integer indexing the Landau level, $\hbar$ the reduced Planck constant, e the electron charge, m^* the cyclotron mass and ω_c the cyclotron frequency given by

$$\omega_c = \frac{eB}{m^*} \ . \tag{2.20}$$

The cross section of a Landau tube in $\boldsymbol{k}$-space is given by

$$a_r = \left(r + \frac{1}{2}\right) \frac{2\pi eB}{\hbar} \ . \tag{2.21}$$

A Landau tube leaves the Fermi surface, whenever its cross sectional area equals an extremal area A on the FS perpendicular to the applied magnetic field, leading to periodic variations in the thermodynamic potential. This condition is fulfilled at equidistant intervals in $1/B$ given by

$$\Delta\left(\frac{1}{B}\right) = \frac{2\pi e}{\hbar A} \ . \tag{2.22}$$

Consequently, the oscillations frequencies are directly proportional to extremal cross-sectional areas on the Fermi surface perpendicular to the applied magnetic field via the Onsager relation [128]

$$f = \frac{\hbar}{2\pi e} A \ . \tag{2.23}$$

The oscillatory part of the grand canonical potential of a three-dimensional is given by [121]:

$$\tilde{\Omega} = \left(\frac{e}{2\pi\hbar}\right)^{3/2} \frac{e\hbar B^{5/2}}{\pi^2 m^* (A'')^{1/2}} \sum_p \frac{1}{p^{5/2}} \cos\left[2\pi p \left(\frac{f}{B} - \frac{1}{2}\right) \pm \frac{\pi}{4}\right] \ , \tag{2.24}$$

where A'' is the curvature factor obtained by differentiating A twice with respect to its normal vector.

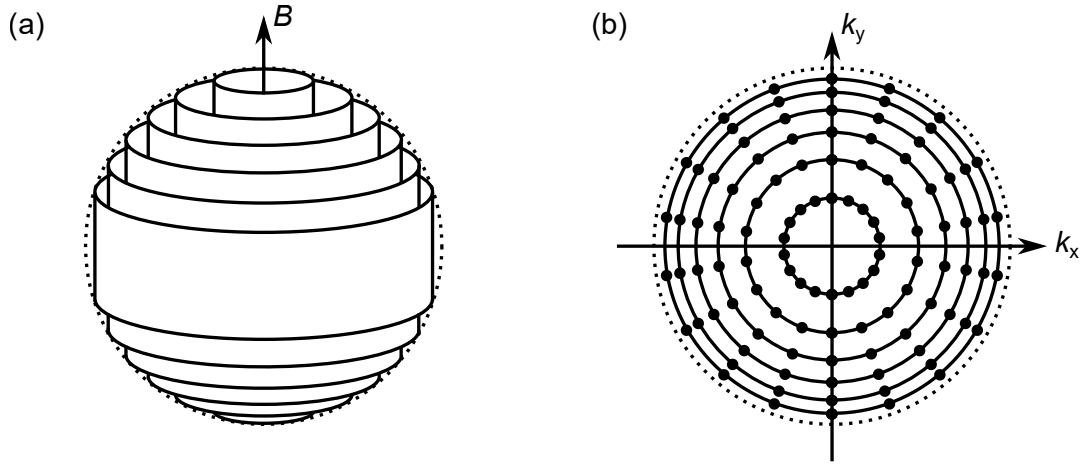

Figure 2.6: Landau quantization. (a) Landau tubes for a spherical Fermi surface with parabolic dispersion. The dotted line represents the zero-field Fermi surface. (b) Quantization of electronic states in a plane perpendicular to the applied magnetic field. Figure adapted from Ref. [121].

Quantum oscillations in the magnetization, the de Haas-van Alphen effect, can be obtained by appropriate differentiation with respect to B or the angle θ between the vectors $\boldsymbol{B}$ and $\boldsymbol{M}$ in the plane where Ω varies most rapidly. The components parallel and perpendicular to the magnetic field are given by

$$\tilde{M}_{\parallel} = -\left(\frac{e}{2\pi\hbar}\right)^{3/2} \frac{\hbar e f B^{1/2}}{2^{1/2}\pi^{5/2} m^* (A'')^{1/2}} \sum_p \frac{1}{p^{3/2}} \sin\left[2\pi p\left(\frac{f}{B} - \frac{1}{2}\right) \pm \frac{\pi}{4}\right] , \quad (2.25)$$

$$\tilde{M}_{\perp} = -\frac{1}{f}\frac{\partial f}{\partial \theta}\tilde{M}_{\parallel} , \quad (2.26)$$

where subleading terms have been omitted. In general, the direction of $M_\perp$ is defined by the anisotropy of the FS. However, in torque magnetometry experiments one typically is only sensitive to a plane defined by the experimental geometry which effectively projects out the component of $M_\perp$ lying in this plane. Thus, for practical purposes the differentiation with respect to θ has to be performed in the plane determined by the experimental geometry.

Oscillations in the resistivity, i.e., the Shubnikov-de Haas effect, are derived from the oscillatory density of states at the Fermi level and can be expressed as

$$\tilde{\rho} \propto \frac{B^{1/2}}{(A'')^{1/2}} \sum_p \frac{1}{p^{1/2}} \sin\left[2\pi p\left(\frac{f}{B} - \frac{1}{2} \pm \frac{\pi}{4}\right)\right] . \quad (2.27)$$

The effects of a finite temperature and the finite lifetime of quasiparticles are expressed in terms of the multiplicative amplitude reduction factors R_T and R_D. The temperature reduction factor R_T arises from the thermal redistribution of electronic states in an area $k_B T$ around the Fermi energy and is given by

$$R_T(m^*) = \frac{X}{\sinh X} \qquad \text{with} \qquad X = \frac{2\pi^2 p m^* k_B T}{\hbar e B} \ , \tag{2.28}$$

where k_B the Boltzmann constant and T the temperature.

The Dingle damping factor is related to the broadening of Landau levels due to the finite lifetime of quasiparticles. It can be expressed as

$$R_D = \exp\left(-\frac{\pi p}{\tau \omega_c}\right) = \exp\left(-\frac{\pi p \sqrt{\frac{2\hbar f}{e}}}{l_{mfp} B}\right) \ , \tag{2.29}$$

where τ is the quasiparticle lifetime and l_{mfp} the mean free path under the assumption of a circular cross section.

The cyclotron mass for a given frequency can be inferred from the temperature dependence of the oscillation amplitudes. Since equation (2.28) gives the temperature reduction factor at a fixed value of B and the oscillation amplitudes were analyzed in a finite field range, the mean value of this field range in $1/B$ was taken as an approximation. This approach is further justified by the use of a windowing function that weighs the data most strongly at this field value and is symmetric with respect to it. We note that this procedure systematically underestimates the cyclotron mass [160]. The estimated uncertainty of the cyclotron masses reported in this thesis is $\pm 5\,\%$.

Magnetic breakdown was taken into account by identifying points at which extremal $\boldsymbol{k}$-space trajectories are close to each other. The probability for magnetic breakdown can be expressed by

$$p = e^{-\frac{B_0}{B}} \ , \tag{2.30}$$

with the breakdown field B_0 given by Chamber's formula [161]

$$B_0 = \frac{\pi \hbar}{2e} \sqrt{\frac{k_g^3}{a+b}} \ . \tag{2.31}$$

Here, k_g is the gap in $\boldsymbol{k}$-space, and a and b are the curvatures of the original orbits at the breakdown junction.

The absolute value of quantum oscillation amplitudes depends on various material specific as well as sample dependent factors. While this renders it challenging to gain information from the absolute amplitudes, a relative comparison of oscillations amplitudes in a set of measurements performed on a single sample can lead to new insights about the underlying electronic structure. In the comparison of our data with predictions from DFT, we calculated the expected relative QO amplitudes using

$$A = \frac{f}{m^*(A'')^{1/2}} R_T R_D \ . \tag{2.32}$$

The cyclotron mass m^* and curvature factor A'' were extracted from the DFT calculations with the SKEAF tool [162]. Realistic experimental values of $B = 18\,\mathrm{T}$, $T = 0.1\,\mathrm{K}$ and $l_{\mathrm{mfp}} = 30\,\mathrm{nm}$ were used in the evaluation. For frequency branches which are only detected in our high field torque magnetometry experiments, we additionally considered the torque factor

$$R_{\mathrm{Torque}} = \frac{1}{f}\frac{\partial f}{\partial \theta} \tag{2.33}$$

in the calculation of the expected QO amplitudes.

2.4 Combination frequencies

There are various mechanisms that are known to lead to combination frequencies in quantum oscillatory spectra that do not correspond to extremal orbits of a single band [121]. These mechanisms include magnetic breakdown [161, 163–165], magnetic interaction [166, 167], chemical potential oscillations [168–170], and quantum interference, also referred to as Stark interference [171]. We briefly explain the mechanisms and their experimental characteristics in the following in order to facilitate the discussion of their relevance to the combination frequencies observed in CoSi in Sec. 5.2.

The first and perhaps most renowned mechanism under consideration is magnetic breakdown (MB). It describes the field assisted tunneling of quasiparticles between adjacent FS trajectories at points at which orbits closely approach each other in $\boldsymbol{k}$-space. In the scenario of two non-intersecting orbits MB results in the emergence of the sum frequency of the individual orbits [173, 174]. If the two orbits have different

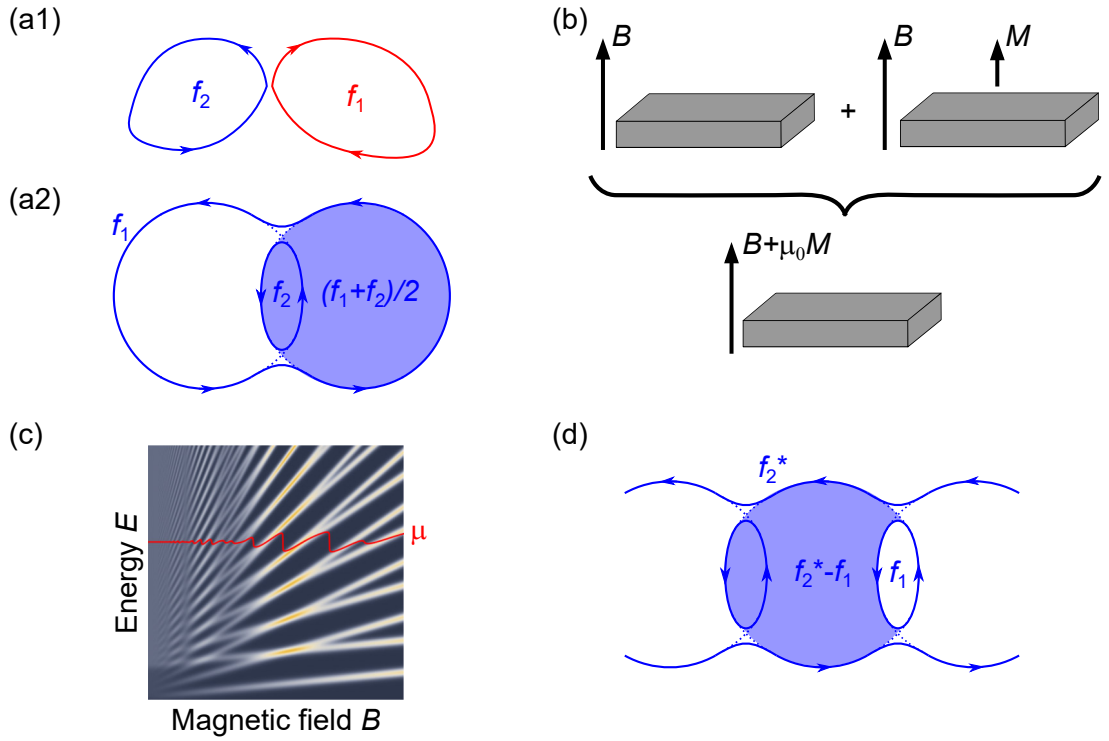

Figure 2.7: Conventional mechanisms leading to combination frequencies. (a1) Magnetic breakdown between two orbits with different character. The signed enclosed area by the combined orbit is $f_2 - f_1$. (a2) MB between nested pockets of the same character. The area enclosed by the MB orbit is $(f_1 + f_2)/2$ (b) Magnetic interaction arises because the field relevant for quasiparticles giving rise to QOs is the internal field $B + \mu_0 M$. The feedback of the induced magnetization M on itself through the internal field may lead to combination frequencies in QO spectra. (c) As a function of B the chemical potential μ oscillates. In the presence of multiple orbits the oscillations in μ may mix the QO frequencies and give rise to combination frequencies. (d) Quantum interference may arise if quasiparticle trajectories are connected through partial magnetic breakdown junctions that realize an interferometer geometry. The particles pick up a phase along their trajectory that depends on the enclosed area. If multiple pathways enclosing different areas are possible, $1/B$-periodic oscillations of transport properties with a frequency proportional to the difference of the enclosed areas may occur. Figure adapted from Ref. [172].

character, i.e., one is an electron and one is a hole orbit, the sign of the enclosed cross sectional area needs to be considered and the combined orbit gives rise to a difference frequency [164, 175]. This case is depicted in Fig. 2.7 (a1). Another situation often encountered in real materials is the case of two nested orbits of the same character which is schematically illustrated in Fig. 2.7 (a2). Complete magnetic breakdown between the two orbits leads to an orbit with frequency $(f_1 + f_2)/2$. If there are more than two breakdown junctions between the nested orbits, various MB orbits with frequencies lying between f_1 and f_2 can be realized. We note that a MB orbit corresponding to the difference frequency of orbits with the same character is semi-

classically forbidden because it would require part of the trajectory to revolve against the direction dictated by the Lorentz force. Further, if we consider partial magnetic breakdown between the nested orbits, a MB trajectory corresponding to the sum of both underlying frequencies is possible. The temperature dependent damping of oscillation amplitudes arising from MB orbits follows the LK temperature reduction factor R_T involving an effective mass determined by the mass of the constituent orbits and the portion of the original trajectory included. For MB between adjacent pockets each orbit is completely included and the effective mass therefore is $m_1^* + m_2^*$. This holds true for both MB between orbits of the same character and MB between an electron and a hole orbit. In the case of the nested orbits shown in Fig. 2.7 (a2) the effective mass is $(m_1^* + m_2^*)/2$ since only half of each original orbit is included. For a sum frequency arising from partial MB the effective mass again is $m_1^* + m_2^*$.

Next, we discuss the effect of magnetic interaction (MI) schematically illustrated in Figure 2.7 (b). If we apply a magnetic field B to a material, a magnetization M is induced. The field relevant for the quasiparticles in the material is the internal magnetic field $B_{\text{int}} = B + \mu_0 M$ rather than only the externally applied field B. Consequently, if there are oscillations in M, they influence the magnetic field that causes them in the first place leading to a feedback effect. If the oscillations in M are large, this feedback can modify the QO spectrum appreciably and in the presence of multiple frequencies it can lead to the generation of combination frequencies. The prerequisite for MI to become appreciable is $\mathrm{d}\tilde{M}/\mathrm{d}H \geq 1$ [121]. The temperature-dependent damping of combination frequencies arising from MI scales with $R_T(m_1^*)R_T(m_2^*)$, suppressing them stronger than the underlying frequencies.

Another mechanism which can potentially give rise to combination frequencies are chemical potential oscillations (CPOs). When Landau levels are not coupled to a thermodynamic reservoir, the chemical potential cannot be treated as a constant, but also experiences quantum oscillations [cf. Fig 2.7 (c)]. In a metal with several extremal FS cross sections, these oscillations may mix the oscillation frequencies. This effect is most pronounced for (quasi-)two-dimensional materials with only a few Landau levels occupied because (almost) the entire FS contributes to the oscillations. In three-dimensional materials CPOs are suppressed due to a large reservoir of unquantized electronic states along the field direction, which do not contribute to the oscillations and act as a reservoir, keeping the chemical potential nearly constant. As for the frequencies arising from MI, combination frequencies caused by CPOs are damped with $R_T(m_1^*)R_T(m_2^*)$.

The last mechanism under consideration is quantum interference (QI), also known as Stark interference. The effect can be understood in terms of interference between quasiparticle trajectories that are linked by partial magnetic breakdown at breakdown junctions. A model of an interferometer geometry for a chain of circular orbits coupled by a weak periodic potential is depicted in Figure 2.7 (d). Note that the orbit corresponding to frequency f_2 is not a fundamental orbit but already involves magnetic breakdown. A quasiparticle on the open orbit has a finite probability of enclosing additional loops with areas f_1 or f_2^*. The real space trajectories are rotated by $\pi/2$ and scaled with the magnetic length squared $l_B^2 = \hbar/(eB)$. For each loop included they pick up a phase of $eBAl_B^4$ through the Aharanov-Bohm effect [176], where Al_B^4 is the real space area enclosed by the loop. The interference between different pathways determines the transmission probability of quasiparticles between breakdown junctions along the open trajectory and therefore influences the transport properties. We note that for this interference effect to be relevant, there needs to be partial magnetic breakdown at the breakdown junctions. The characteristics of QI oscillations are remarkably similar to QOs. Since the relative phase between paths scales with $1/B$, QI leads to $1/B$-periodic oscillations of the transport properties. The frequency of QI oscillations is proportional to the difference of the areas enclosed by the interfering pathways in reciprocal space A. While in general they do not need to be combinations of fundamental QO frequencies, in the simple model depicted in Fig. 2.7 (d) an interferometer geometry is realized by the small orbit f_1 and the large MB orbit f_2^* which can give rise to QI oscillations at the difference frequency $f_2^* - f_1$. Interestingly, this mechanism may exhibit a weak temperature dependent damping [164]. This is the case if the area enclosed by the interferometer only depends weakly on the chemical potential. Quantum interference has primarily been investigated in quasi-two-dimensional systems featuring a complex network of magnetic breakdown junctions with open orbits [177–179].

3 Experimental Methods

In this thesis, high-quality single crystals of CoSi have been investigated using a range of different measurement techniques. In this chapter, we introduce the experimental methods used. First, we discuss the sample preparation and characterization. Next, we give an overview of the cryogenic system used most extensively for the measurements presented here and describe measures that have been taken to minimize external noise on the signal. We discuss the measurement techniques used to determine the magnetic and electric properties of CoSi and explain how the data was analyzed in order to obtain the presented quantum oscillation spectra.

3.1 Sample preparation

High-quality single crystals of CoSi were grown at our chair using the optical floating zone technique [180–182] prior to the work reported here. The samples have been characterized in terms of their residual resistivity (cf Fig. 3.2). Samples obtained from optical floating zone growths are labeled as HKZ7 S1 and HKZ7 S2.

During the course of this thesis we synthesized further CoSi single crystals using a flux growth method inspired by Refs. [138, 139]. The flux-grown sample selected for the measurements presented here is denoted as FLX1. We tested several annealing procedures while systematically varying the annealing parameters on samples obtained from both flux and optical floating zone growths. As a result, samples exhibiting a higher crystalline quality than previously available have been obtained.

3.1.1 Single-crystal synthesis

We prepared single crystals of CoSi with a flux growth method using the following procedure. High-purity starting materials of 99.995 % Co (MaTecK) and 99.9999 % Si (Alfa Aesar) were mixed with 99.9999 % Te (Alfa Aesar) flux in an atomic ratio of $1 : 1 : 20$. The mixture was loaded into an alumina crucible and sealed in a quartz tube under Ar atmosphere. It was heated to 1150 °C in a rod furnace and kept constantly at this temperature for 20 h to allow for homogenization. The mixture was then slowly cooled to room temperature at a rate of 3 °C/h. The Te flux was removed through etching with 50 % nitric acid. Several millimeter-sized crystals with octahedral shape, as depicted in Fig. 3.1 (a), were obtained.

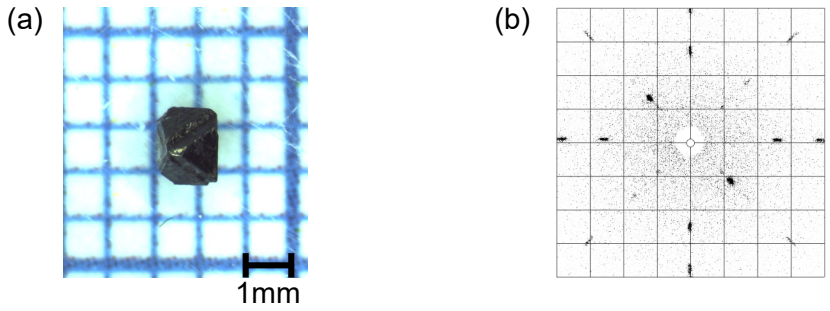

Figure 3.1: Flux grown sample. (a) Octahedral single crystal obtained from a Te flux growth. (c) Typical Laue pattern of a CoSi single crystal oriented along a [100] direction.

The phase purity was confirmed via powder X-ray diffraction. The orientation of the single crystals was determined by Laue X-ray diffraction. A typical Laue pattern recorded with the sample oriented along a crystallographic [001] direction is depicted in Fig. 3.1 (b). The positions of the atoms in the simple cubic unit cell (cf. Sec. 2.2) reduce the symmetry from four- to twofold, as seen in the diffraction pattern. The absence of additional reflexes confirms the high crystalline quality. The samples were cut into thin platelets with edges parallel to the major crystallographic axes using a wire saw. The thickness of the samples ranges from 120 µm to 200 µm, the width from 0.8 mm to 1 mm, and the length from 1 mm to 5 mm. The longest axis of the platelet is oriented along a crystallographic [110] direction for all samples. The shortest axis corresponds to a [001] direction for samples HKZ7 S1 and HKZ7 S2, and to a [111] direction for sample FLX1.

3.1.2 Annealing

Crystalline defects, which may have bee introduced by rapid cooling or the mechanical preparation of the samples, may be reduced by heating the platelets to a temperature close to their melting point. This annealing procedure was performed in an UHV-compatible oven with the option of introducing Argon atmosphere. All samples were characterized in terms of their residual resistivity both before and after the annealing. Different annealing protocols were tested for samples obtained from both flux and optical floating zone growths. Samples exhibiting the highest crystalline quality have been obtained by keeping them a constant temperature of 1100 °C for 100 h, followed by a slow cooling to room temperature with a rate of 12.5 °C/h. Samples HKZ7 S1 and FLX1 have been annealed under Argon atmosphere and sample HKZ7 S2 has been annealed in a vacuum of $\approx 2 \times 10^{-8}$ mbar.

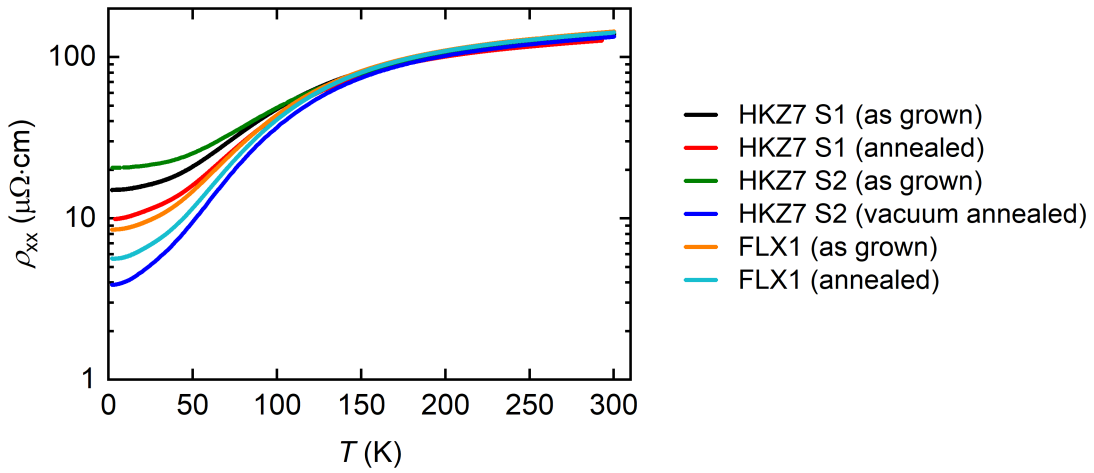

Figure 3.2: Sample quality comparison. Resistivity ρ_{xx} as a function of temperature T. All samples exhibit metallic behavior with varying residual resistivities indicating different defect concentrations.

The resistivity as a function of temperature is shown in Figure 3.2. All samples exhibit a metallic behavior with a resistivity of $\rho_{300\,\mathrm{K}} \approx 140\,\mu\Omega\,\mathrm{cm}$ at room temperature, consistent with reports from the literature [138, 153]. The residual resistivity ρ_0 at 2 K varies between the samples. The residual resistivity ratio (RRR), defined as $\rho_{300\,\mathrm{K}}/\rho_0$, may be taken as an indicator for the defect concentration. The RRRs of samples HKZ7 S1, HKZ7 S2, and FLX1 are 16, 34, and 26, respectively. These values for CoSi are rather low when compared to other metallic compounds but are among the highest reported to date for CoSi [138–140, 142, 153, 183, 184].

3.2 Measurement setup

The detection of small signals in a cryogenic environment and under high magnetic fields requires a carefully designed setup, which ensures reliable signal detection while minimizing unwanted noise and heat load on the cryostat. A large part of the measurements presented in this thesis were performed in a dilution refrigerator, that was equipped with cryogenic wiring and a rotational stage suitable for the installation of custom measurement setups and in-situ sample rotation. This section provides an overview of the whole setup, describes the custom wiring, and discusses methods to reduce noise on the measurement signal through filtering and amplification.

Figure 3.3 shows a schematic overview of the measurement setup that was developed and used for most experiments presented in this thesis. The sample is mounted in a dilution refrigerator insert, which can be installed into an 18/20 T superconducting

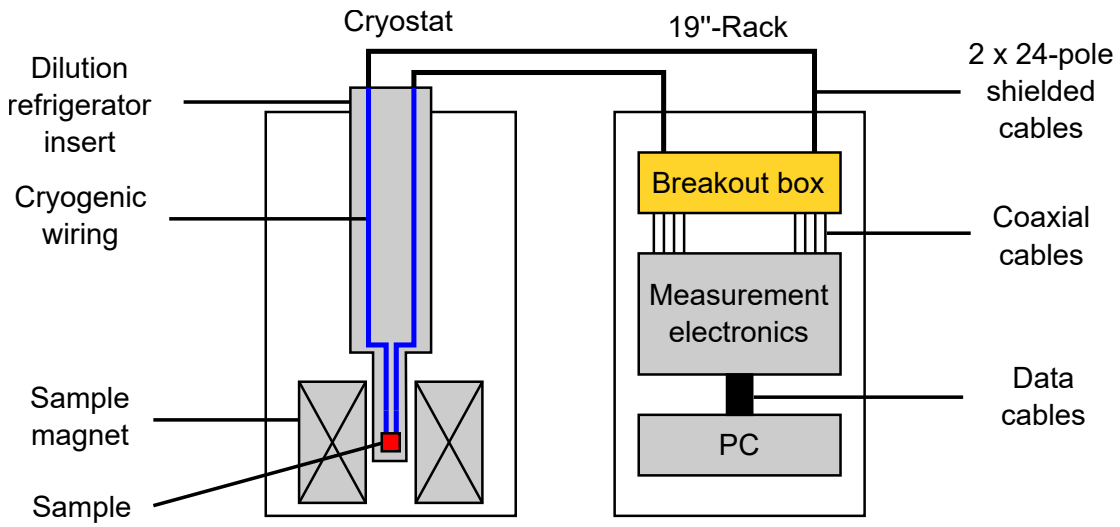

Figure 3.3: Measurement setup. The sample is mounted in an 18/20 T superconducting magnet system with a dilution refrigerator insert. Contacts to the measurement electronics are established via cryogenic wiring inside the cryostat and shielded cables at room temperature.

magnet system. The insert has been equipped with electrical connections suited for a range of experiments. The measurement electronics and data acquisition PC are situated in a separate rack. It is connected to the cryostat via two 24-pole shielded cables. Inside the rack, the cables connect to a breakout box equipped with low-pass filters. The 48 poles are mapped to individual BNC connectors allowing for an easy connection to the measurement electronics. The data acquisition PC serves to record the detected signals, control the cryostat system, and execute automated measurement protocols.

3.2.1 Dilution refrigerator

The dilution refrigerator utilized for measurements in the milli-Kelvin regime is an Oxford Instruments Kelvinox MX400 [185]. It provides a continuous cooling power of 400 µW at 100 mK and reaches a base temperature <10 mK at the mixing chamber (MC) in the absence of any additional heat loads.

The operating principle of dilution refrigerators is well explained in standard text books [186, 187] and is only briefly recapitulated here. A picture and schematic of the low-temperature part of the dilution refrigerator insert used in this thesis is depicted in Figure 3.4. During operation the whole insert is sealed by the inner vacuum chamber (IVC) and evacuated in order to thermally insulate the ultra-low-temperature stages from the surrounding He-bath of the cryostat. The MX400 uses

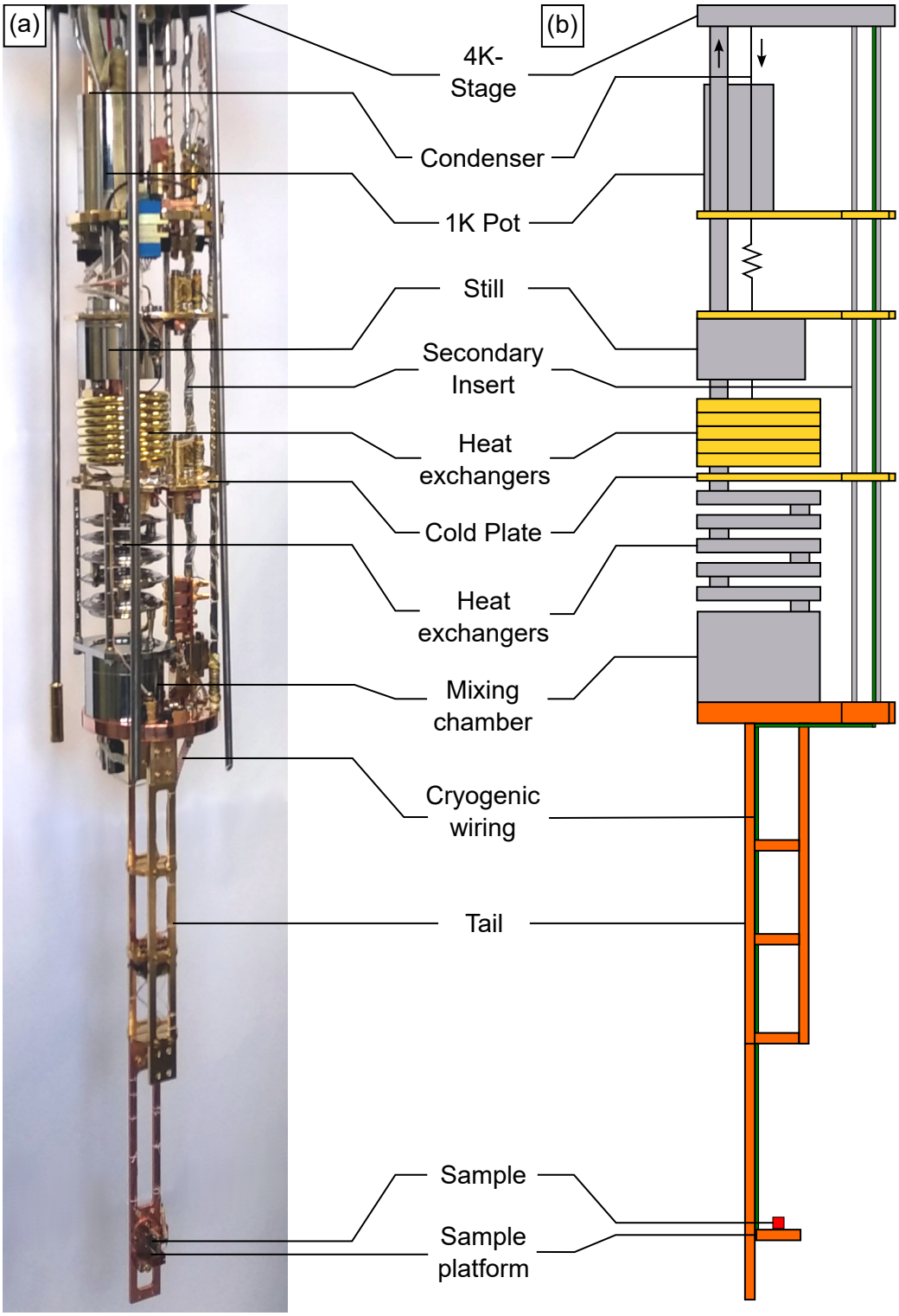

Figure 3.4: Dilution refrigerator insert. (a) Photograph of the low-temperature part of the Kelvinox MX400 dilution refrigerator insert. In operation, the mixing chamber and tail is surrounded by a radiation shield mounted at the cold plate stage. The whole assembly is enclosed by the inner vacuum chamber (IVC) and evacuated before being mounted in the cryostat. The sample is mounted on a rotational platform located at the bottom of the insert. (b) Schematic depiction of the low-temperature part of the dilution refrigerator insert. The flow of ^{3}He-^{4}He mixture is indicated by arrows.

an additional heat shield mounted at the cold plate stage that additionally protects the MC and the sample from thermal radiation of the IVC. A mixture of ^{3}He-^{4}He is circulated in a closed cycle. The mixture enters the insert through the condenser in gaseous form. It is precooled in several stages condensing it into a liquid. A phase boundary in the mixing chamber separates a ^{3}He-rich phase from a mixed phase of ^{3}He and ^{4}He. The positive enthalpy of mixing results in a cooling effect when ^{3}He-atoms transfer from the ^{3}He-rich phase into the mixed phase. To establish a continuous flow of ^{3}He atoms they are constantly removed from the mixed phase at the still. All stages of the dilution refrigerator have optimal operating conditions and care has to be taken when modifying the insert, e.g., through experimental wiring or additional devices mounted in the system, in order to ensure minimal impact on the cooling process.

The following modifications were developed and implemented during the course of this thesis and a preceding master's thesis [188]. First, a mechanical assembly was constructed that extends the bottom of the MC to the field center of the superconducting magnet. This tail was equipped with a piezoelectric rotator supplied by attocube [189]. The rotational stage was later replaced by a mechanical rotator supplied by Oxford Instruments which was modified in order to improve the thermal connection between the rotational stage and the MC. The rotational stages are further discussed in Sec. 3.2.2. Second, the dilution refrigerator insert was equipped with custom cryogenic wiring. The Kelvinox MX400 features a removable secondary insert into which the experimental wiring was incorporated. Details of the technical considerations and their implementation are given in Sec. 3.2.3. Finally, the system was equipped with CMR low-temperature transformers [190] described in Sec. 3.2.4 to achieve a better signal-to-noise ratio in the performed electrical transport measurements.

3.2.2 Rotational stage

For an investigation of the influence of the magnetic field direction on the response of our samples, the setup was equipped with a uniaxial rotator allowing for in situ sample rotation. Two different rotators have been used in the measurements presented in this thesis. The first setup, utilized for the majority of electrical transport measurements, incorporates a piezoelectric rotator with resistive readout supplied by attocube [189]. It has been implemented in a preceding master's thesis in which it is described in further detail [188]. One of the limitations of this setup is the need for experimental wiring that exerts little restoring torque to the rotational motion in order to prevent a

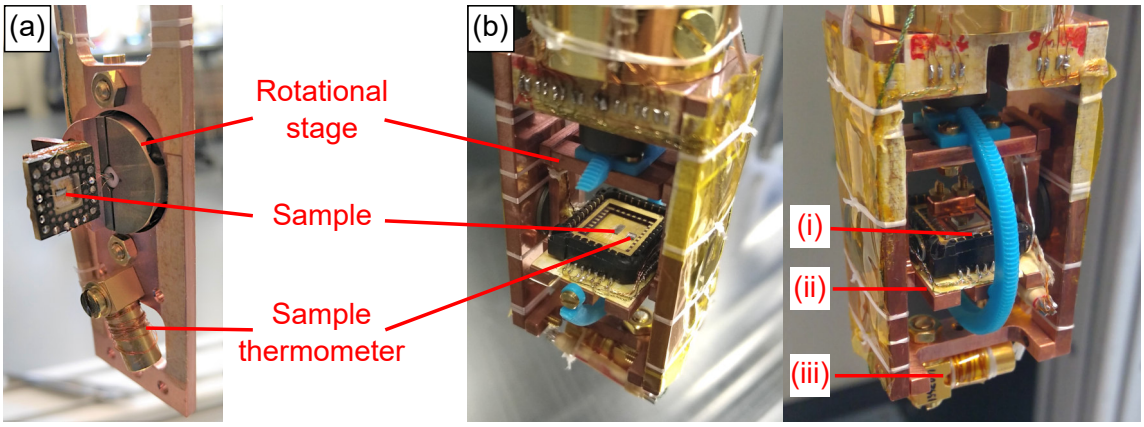

Figure 3.5: Rotational stage. (a) Piezoelectric rotator mounted at the tail of the cryostat. Its implementation and characterization is described in detail in Ref. [188]. (b) Lower part of the modified mechanical rotator developed during this thesis. The sample is mounted on an LCC. Three resistance thermometers (i)-(iii) have been mounted on different parts of the setup to probe the thermal contact between them.

slipping of the rotational platform. Especially for torque magnetometry measurements, for which shielded coaxial cables are essential, the piezoelectric rotator is therefore not ideal. During the course of this thesis a mechanical rotator supplied by Oxford Instruments has been installed and the rotational platform was modified in order to improve the thermal contact between the mixing chamber and the sample stage. We discuss the technical considerations and calibration of the modified design in the following.

Figure 3.5 shows both the piezoelectric and the mechanical rotator. Both setups include a hollow axis through which the experimental wiring is routed. For the piezoelectric rotator 50 µm Cu wires have been used. The sample is mounted on a Cu platform which can be attached to the rotational stage. The experimental wiring is then soldered onto a contact pad surrounding the sample. For the setup incorporating the mechanical rotator, a socket for leadless chip carriers (LCCs) was mounted on the rotational platform. Electrical contacts are established through seven twisted pairs of 80 µm Cu wires and two coaxial cables with a 200 µm Cu inner conductor an outer jacket diameter of 1 mm. All wires are again routed through the hollow axis of the rotational stage and soldered onto the LCC socket connectors. Unused pins on the LCC socket were mutually connected to each other and to one of the outer conductors of the coaxial cables in order to establish a common ground potential. Samples for this setup are prepared on an LCC which can then be mounted into the system establishing electrical connections without the need for additional soldering.

One of the concerns with the mechanical rotator setup as delivered by Oxford Instruments was the thermal coupling of the rotational stage. The rotational platform was manufactured from an insulating plastic (Torlon-PAI) which has a low thermal conductivity in the milli-Kelvin temperature range. Consequently, initial tests showed that while the MC achieved a base temperature of <15 mK, a resistance thermometer mounted on the rotator as supplied decoupled from the MC and remained at a constant temperature of ≈150 mK. We completely redesigned the rotational stage shown in Fig. 3.5 (b) and replaced all plastic parts by OFHC copper where possible. The only part that could not be manufactured from copper due to its complex geometry is the gear wheel. It was fabricated from epoxy resin using a 3D-printer. We equipped the modified rotational stage with three resistance thermometers located on the LCC (i), at the bottom of the rotational platform (ii), and at the bottom of the insert tail (iii). Initial tests showed a slow cooldown of the sample platform to ≈50 mK and a significant rise in temperature to ≈100 mK upon applying an excitation current to the sample indicating an insufficient thermal coupling of the platform. We therefore added a vacuum annealed silver wire with a diameter of 0.5 mm to the setup. It was clamped to the MC and the rotational platform, thereby providing a direct thermal connection between the two. A good thermal equilibration was observed for temperatures >100 mK. For lower temperatures, the temperature of the rotational platform lags behind the mixing chamber temperature, although much less than without the additional silver wire. The base temperature achieved at the sample platform was 40 mK and the lowest temperature recorded on the LCC was 65 mK. Further improvements of the thermal coupling may be achieved by incorporating more silver wires and optimizing the annealing procedure to improve their thermal conductivity.

Following the redesign of the rotational stage a Hall probe was mounted on the rotational platform in order to test the calibration and reproducability of the rotator. The sample orientation is manipulated by a stepper motor located on top of the insert whose movement is mechanically transmitted to the sample platform via a shaft and gear assembly. The angle of the rotational platform is then calculated form the position of the stepper motor. To have an independent measure of the sample orientation the Hall voltage over the Hall probe was recorded in an applied magnetic field of 5 T. Data recorded during the calibration procedure is shown in Figure 3.6. The platform was rotated over a total angle of 240° as calculated with the transmission ratio of the original setup. The resulting signal as a function of the calculated angle is shown in Fig. 3.6 (a). A fit of the Hall voltage yields a periodicity

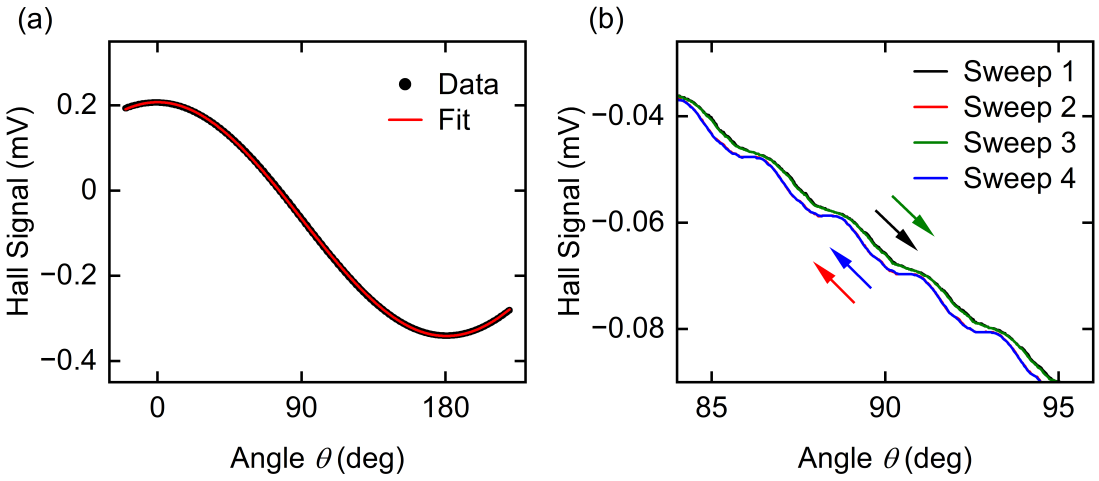

Figure 3.6: Rotator Calibration. (a) Voltage signal of the Hall probe as a function of calculated angle θ. (b) Signal for subsequent angular sweeps. The data curves for sweeps in the same direction lie almost perfectly on top of each other. The oscillations on the voltage signal indicate a motion of the rotational platform that is not perfectly uniform.

of $(360.1 \pm 0.5)^\circ$ indicating that the modified setup has the same transmission ratio as the original one. We note that the position corresponding to 0° is a variable parameter and needs to be recalibrated after mounting a new sample. In order to verify the reliable operation of the rotator it was rotated in four subsequent angular sweeps, two for increasing and two for decreasing angle, while simultaneously recording the voltage signal of the Hall probe. Fig. 3.6 (b) shows that the Hall signals for rotations in the same direction lie almost perfectly on top of each other indicating a good reproducability of the sample orientation. The deviation of the signals recorded for increasing and decreasing angle is attributed to a mechanical backlash of the rotator which is estimated to be $<1^\circ$. Additionally, we note that the Hall signal for decreasing angle exhibits an oscillating nature indicating that the rotational motion is not perfectly uniform. The same effect is seen for increasing angle, although with a smaller amplitude. We estimate the angular accuracy of the modified setup to be $\pm 0.3^\circ$ for rotation with increasing angle and $\pm 0.6^\circ$ for rotation with decreasing angle.

3.2.3 Cryogenic wiring

The cryogenic wiring inside the dilution refrigerator insert serves to provide electrical connections to the sample stage without introducing an excessive heat load on the system. Since the measurement setup was intended to be used with a variety of different experimental setups, it was prepared with the necessary cables for each measurement technique. Additional wires for the connection of further thermometers or heaters have been included.

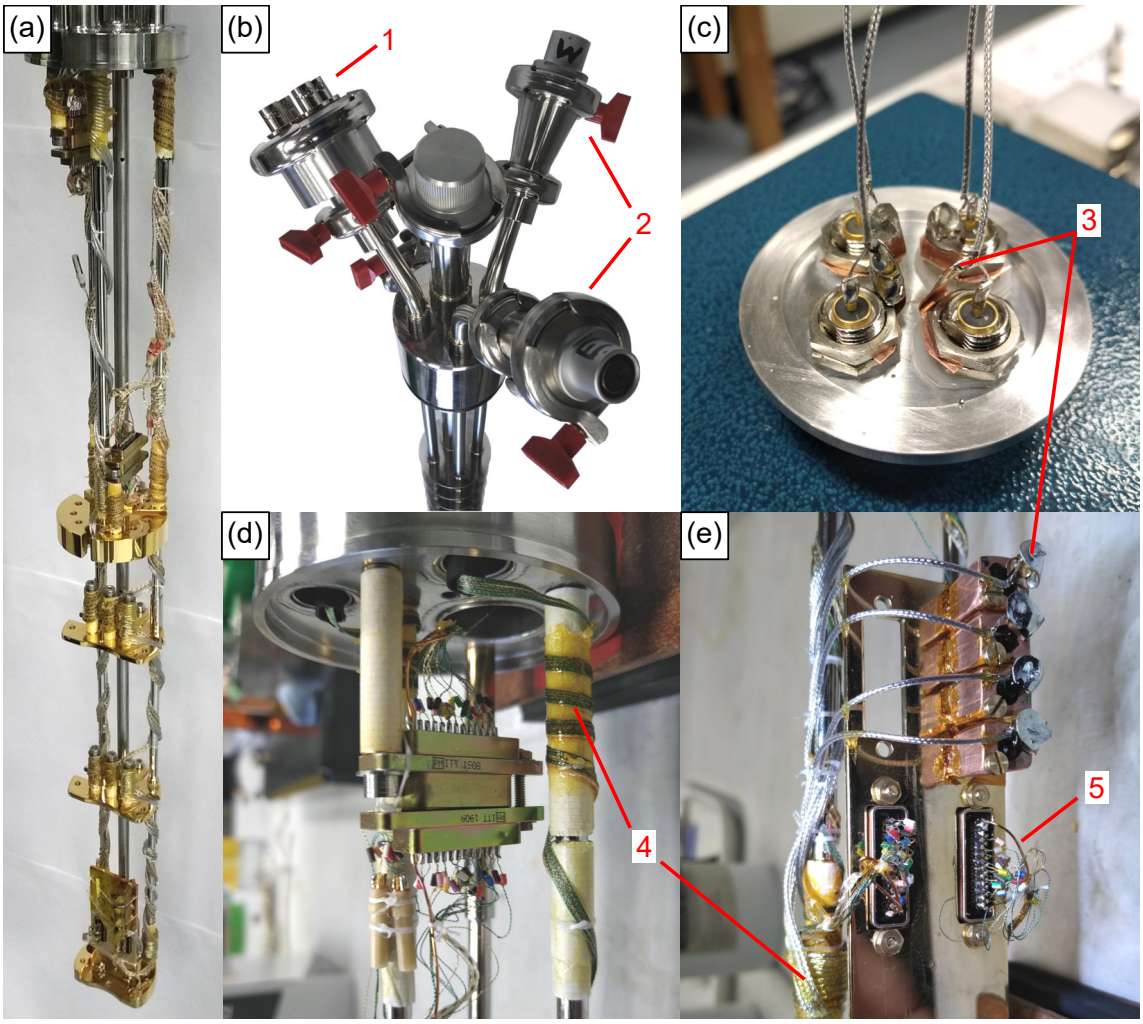

Figure 3.7: Cryogenic wiring. (a) Lower part of the secondary insert with custom wiring. (b) Top view of the secondary insert with vacuum feedthroughs for 4 BNC-connectors (1) and two 24-pole shielded cables (2). (c) Inner part of the BNC-connector flange. The outer conductor of the coaxial cables (3) is isolated from the cryostat ground. (d) Connections at the 4 K plate. The cryogenic wires are varnished onto Cu heat sinks (4) to allow for a good thermal anchoring at each temperature stage of the dilution refrigerator. Electrical insulation is ensured by a thin layer of cigarette paper. (e) Connectors at the mixing chamber plate. A strain relief (5) ensures mechanical protection of the soldering connections.

Each wire that connects the room temperature side of the dilution refrigerator with the sample introduces a heat load, consequently elevating the base temperature of the system. The thermal conductivity κ of a metal is linked to its electrical conductivity σ by the Wiedemann-Franz law, $\kappa = L\sigma T$, where L is the Lorenz number and T is the temperature. Hence, wires possessing high electrical resistivity have a lower impact on the heat load as compared to those with lower resistivity. However, this may change due to Joule heating when an electrical current flows through the wires. The power dissipated in an Ohmic conductor is given by $P = I^2R$, where I is the

current and R the resistance. Therefore, for wires conducting substantial currents during an experiment, it is preferable to utilize low-resistance wiring to mitigate this effect.

Photographs of the custom-made experimental wiring are shown in Figure 3.7. A combination of constantan, copper, brass, and superconducting NbTi wires in a CuNi cladding have been installed to meet various experimental requirements. We used twisted pairs to reduce the influence of external noise, e.g., from radio frequency radiation. Additionally, the wires carrying excitation currents are spatially separated from wires which are used for the detection of small voltage signals in order to avoid crosstalk. Stainless steel coaxial cables have been installed for three-terminal capacitance measurements, for which the outer conductor of the cable is used as a shield. In order to avoid ground loops that could introduce noise on the signal the outer conductors are separated from the cryostat ground along their entire length. Depending on the experimental needs, they can be grounded either at the measurement electronics or close to the sample.

Special care was taken in thermally anchoring the wires to each temperature stage of the dilution refrigerator insert to avoid excessive heat load on the mixing chamber. To achieve a good thermal contact of the wires, they were wound around Cu cylinders mounted at each stage. The wires were fixed into place with dental floss and covered with GE varnish. Cigarette paper around the Cu cylinders is used to prevent electrical contact between the wires and cryostat ground. Assuming a perfect equilibration of the temperature of the wires at every stage, the heat load $\dot{Q}$ on each stage can then be calculated using

$$\dot{Q} = n\frac{A}{l}\int_{T_1}^{T_2} \kappa(T)dT \ , \tag{3.1}$$

where n is the number of wires, A their cross section, l their length, T_1 and T_2 the temperature of the respective stages and κ the thermal conductivity of the wires. Thermal conductivity integrals have been taken from Refs. [191, 192].

The calculated heat load on the different stages of the dilution refrigerator insert is summarized in Table 3.1. The heat load on the upper stages up to the still are not crucial for the performance of the dilution refrigerator because of the large cooling power of these stages. Also the cooling power of the mixing chamber (400 µW at 100 mK) is much larger than the heat load of 1.7 µW introduced by the cryogenic

Stage	$\dot{Q}$ (µW)					
	Cu	Brass	Constantan	NbTi	Coax	**Total**
4K	20×543	–	28×27	–	4×890	**15176**
1K-Pot	12×7.26	–	28×0.04	8×0.04	4×0.33	**89.9**
Still	4×2.65	–	28×0.02	16×0.01	4×0.07	**11.6**
Cold plate	4×1.206	4×0.009	28×0.003	16×0.006	4×0.018	**5.1**
MC	4×0.408	4×0.003	28×0.001	4×0.004	4×0.006	**1.7**

Table 3.1: Heat load. Calculated heat load $\dot{Q}$ on the stages of the dilution refrigerator introduced by the cryogenic wiring.

wiring. The biggest effect has been observed on the cold plate temperature. This stage is only passively cooled by cold mixture from the mixing chamber and consequently the additional heat load manifested itself in a rise of the cold plate base temperature from 80 mK without experimental wiring to 150 mK with the additional heat load from the wires. This increased temperature results in a increased temperature of the mixture returning to the mixing chamber and consequently a higher base temperature. With the experimental wiring installed the dilution refrigerator consistently achieved a base temperature below 15 mK at the mixing chamber.

3.2.4 Signal filtering and amplification

The connection of cryogenic wiring to the measurement electronics is established via a breakout box, which maps the 24-pole shielded cables onto separate BNC connectors. Only the inner conductors are used for signal transmission and the outer conductors act as shielding. The breakout box includes low-pass filters to further reduce high-frequency noise on the wires, that could lead to unwanted heating of the sample or affect the measured signal. The filters are realized as a LC circuit comprising a common mode choke as impedance for each twisted pair, as depicted in Fig. 3.8 (b). The cutoff frequency f_0 is given by

$$f_0 = \frac{1}{2\pi LC} \tag{3.2}$$

With the chosen inductance of $L = 1\,\text{mH}$ and capacitance of $C = 4.7\,\text{nF}$ the cutoff frequency is 73.4 kHz. This configuration effectively filters out radio-frequency noise while leaving moderately high AC signals unaffected. A photograph of the breakout box is shown in Figure 3.8 (a).

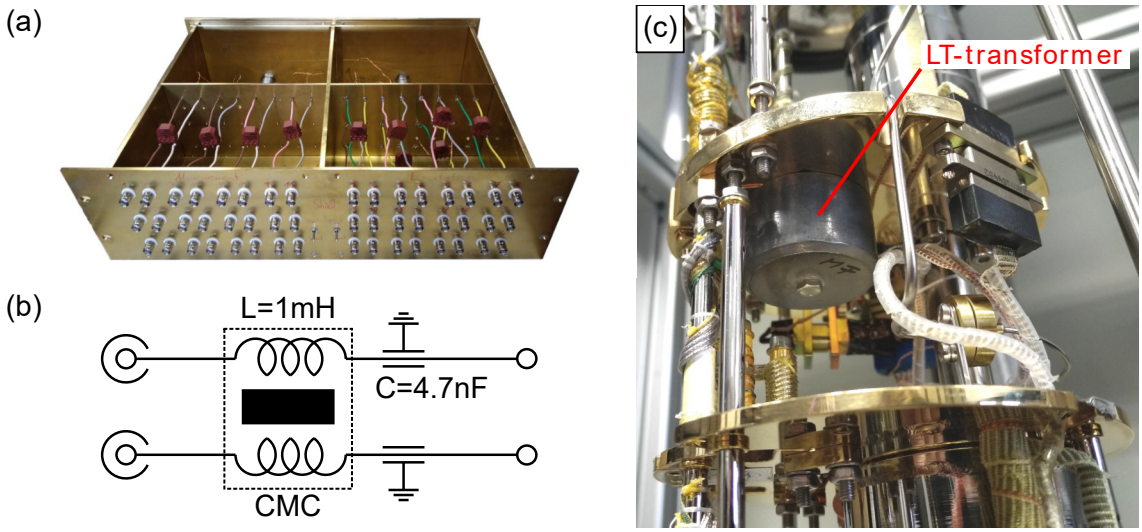

Figure 3.8: Low-pass filters and low-temperature transformer. (a) Front view of the breakout box housing the low-pass filters. (b) Circuit diagram of the filters. The common mode choke (CMC) shares a single core for both signal lines in order to reduce common mode noise. (c) Low-temperature transformer surrounded by lead shielding mounted on the bottom of the 1K-plate.

Another way of increasing the signal-to-noise ratio involves signal amplification. For this purpose, two different kinds of transformers have been used in this thesis. The first kind of transformer, employed for the majority of measurements presented here, is an AMETEK Model 1900 low-noise transformer. Positioned within the signal line between the breakout box and the measurement electronics, this transformer was used with an amplification ratio of 1:100. However, together with the amplification the noise level also exhibited a tenfold increase. Consequently, the net gain in signal-to-noise ratio using this setup is approximately one order of magnitude. The second type of transformer, we used, is a LTT-m low-temperature transformer provided by CMR-Direct [190]. This transformer was mounted on the 1K-pot plate within the dilution refrigerator insert, as shown in Figure 3.8 (c). Here, the amplification takes place close to the signal source and the transformer is operated at cryogenic temperatures. Therefore, minimal noise is introduced on the signal before the amplification. Operating at amplification ratios of up to 1:100, no discernible increase of the noise level was observed, consequently allowing for a signal-to-noise ratio improved by two orders of magnitude.

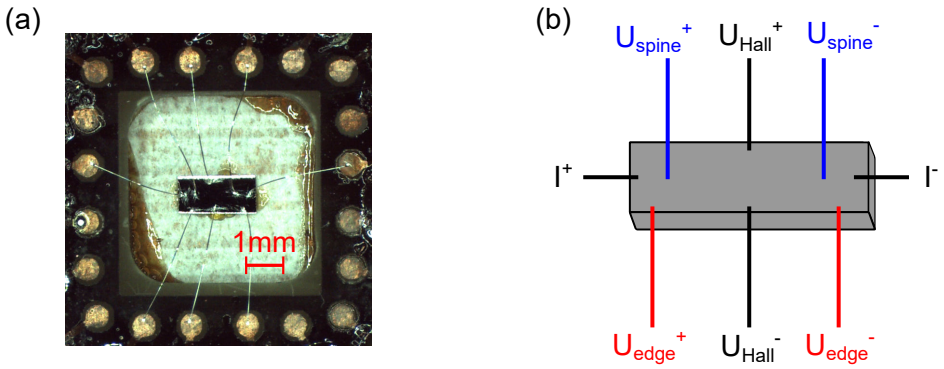

Figure 3.9: Transport sample. (a) Photograph of the sample contacted in an 8-point configuration with longitudinal voltage contacts at the edge and spine of the sample. (b) Schematic depiction of the contact geometry.

3.3 Measurement techniques

This section provides an overview of the measurement techniques used in this thesis. We begin with a description of electrical transport measurements. Next, we explain how the magnetization was measured using cantilever-based torque magnetometry and vibrating sample magnetometry.

3.3.1 Electrical transport

For measurements of the electrical transport properties, the samples have been glued onto a Cu platform using GE varnish. Electrical isolation from the cryostat ground is ensured via a thin cigarette paper between sample and platform. Electrical contacts to the sample are established via Al wire bonds, which connect the sample to a PCB onto which the cryogenic wiring was soldered. A photograph of a typical transport sample is shown in Figure 3.9 (a). A schematic depiction of the contact geometry is shown in Fig. 3.9 (b). The samples have been contacted in a Hall geometry with two wires carrying an excitation current I, two wires for the detection of the transversal voltage drop U_{Hall} and up to four wires for the longitudinal voltage drop U_{spine} and U_{edge}. Sinusoidal AC excitation currents with a frequency of 22.08 Hz and amplitudes between 100 µA rms and 4 mA rms were applied using a Keithley 6221 current source. The voltage drops across the sample were amplified using low-noise preamplifiers (see Sec. 3.2.4) and detected with a conventional lock-in technique using Stanford Research SR830 and Zurich Instruments MFLI lock-in amplifiers. Typical time constants used were between 1 and 3 s and the applied magnetic field was varied with a constant slow sweep rate between 30 and 50 mT/min.

3.3.2 Cantilever-based torque magnetometry

In our study of the de Haas-van Alphen (dHvA) effect, we used cantilever-based torque magnetometry with a capacitive readout. A schematic view of the setup is shown in Figure 3.10. The sample is placed on a metallic cantilever and fixed with GE varnish or vacuum grease. Under the influence of an externally applied, uniform magnetic field B, the magnetization M is induced in the sample. Since the oscillatory magnetization arising from the dHvA effect reflects the Fermi surface anisotropy, it is in general not parallel to B, except when the external magnetic field is applied exactly along a high-symmetry direction of the crystal lattice. For an arbitrary direction of the applied magnetic field, a torque τ is induced on the magnetic moment of the sample resulting in a deflection of the cantilever. In the dHvA effect this torque is given by [121]

$$\tau = \tilde{M}_{\perp} B V \ , \tag{3.3}$$

where $\tilde{M}_{\perp}$ is the oscillatory magnetization perpendicular to the applied magnetic field B, given in Eq. (2.26), and V the sample volume.

The cantilever and a fixed counter electrode are arranged into a plate capacitor configuration. The resulting capacitance is given by

$$C_0 = \frac{\epsilon_0 A}{d} \ , \tag{3.4}$$

where ϵ_0 is the vacuum permittivity, A the area, and d the distance between the plates. The deflection of the cantilever leads to a change in distance Δd, which, in turn, causes a change in capacitance ΔC. To first order the change in capacitance is given by

$$\Delta C = \frac{\epsilon_0 A}{d} \Delta d \ . \tag{3.5}$$

For small elastic deflection of the cantilever the change in distance Δd is proportional to the torque and thus

$$\Delta C \propto \tau \propto M_{\perp} \ , \tag{3.6}$$

thereby providing a measure for the magnetization of the sample perpendicular to the applied field. Since we only compared oscillation amplitudes relative to each other, we report the measured change in capacitance ΔC directly, rather than converting it to a torque or magnetization. A photograph of the cantilever setup used in our laboratory is depicted in Figure 3.10 (b).

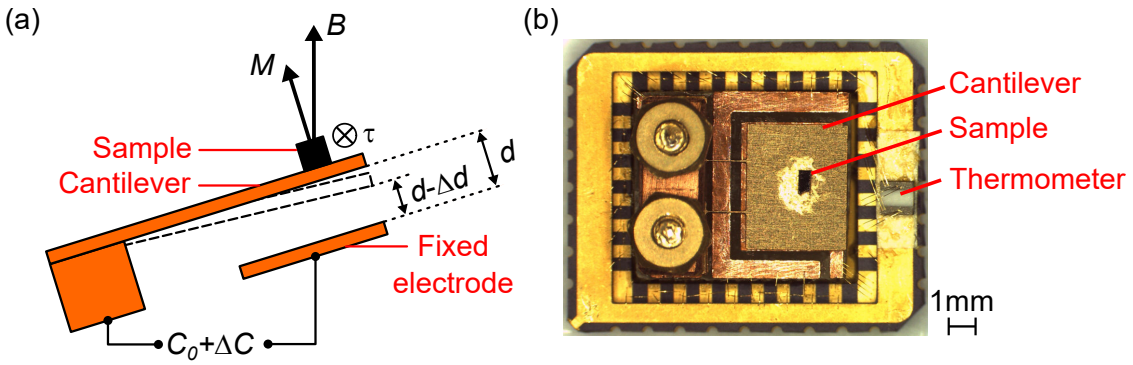

Figure 3.10: Cantilever magnetometry. (a) Schematic side view of the cantilever setup. The external magnetic field B results in a torque τ on a magnetized sample. The torque deflects the cantilever thereby changing the distance d between the cantilever and a fixed electrode. The change in distance Δd can be detected via a change in capacitance ΔC between the cantilever and the fixed electrode. (b) Photograph of the cantilever with an attached sample. The setup is fixed onto an chip carrier that provides electrical connections.

3.3.3 Vibrating sample magnetometry

The second method we employed to probe the magnetization of our samples is vibrating sample magnetometry (VSM). In contrast to torque magnetometry, which is sensitive to the part of the magnetization perpendicular to the applied magnetic field, VSM probes the magnetization parallel to an axis determined by the geometry of the specific setup used.

A magnetic sample, which is moved through a detection coil, produces a change of magnetic flux Φ in the coil, that is proportional to the magnetization M and volume V of the sample. The change in flux induces a voltage U_{ind} in the coil given by

$$U_{\text{ind}} = \frac{d\Phi}{dt} \propto MV \ . \tag{3.7}$$

In VSM, the sample is moved in a sinusoidal motion around the center of the detection coil, thereby inducing an AC voltage signal, which can be recorded using standard lock-in techniques. The use of multiple detection coils in a gradiometer geometry suppresses signals induced by the change of the externally applied field. Calibration of the setup using a reference sample allows for a quantitative analysis of the magnetization. For the setups we used, the axis of the detection coils is parallel to the direction of the applied magnetic field. Thus, the part of the magnetization parallel to the applied magnetic field is detected.

The data presented in this thesis were recorded in two commercially available Quantum Design measurement systems. Data recorded up to 14 T were obtained from a PPMS [193] with the standard VSM option. Data recorded up to 7 T were recorded in an MPMS 3 [194], which uses a superconducting quantum interference device (SQUID) in its detection electronics, providing a higher sensitivity. Both setups were used without in situ sample rotation and data was recorded for one specific orientation of the applied magnetic field only.

3.4 Data analysis

In the following, we discuss how the data obtained from different experiments was analyzed with regard to its oscillatory components. We illustrate the procedure on an exemplary dataset and explain the effects of two standard methods, zero padding and windowing functions, which are commonly used in the analysis of finite periodic signals [195–197].

Figure 3.11 (a) shows a typical dataset of a resistivity measurement as function of the applied magnetic field. It exhibits a monotonically increasing, non-oscillatory component superposed by oscillations at high magnetic fields. The non-oscillatory component of the resistivity was approximated by fitting a polynomial to the data. The order of the polynomial was chosen as low as possible to avoid artificially introducing low-frequency components and as high as necessary to efficiently remove the non-oscillatory background. For the data presented in this thesis polynomials between fifth and eighth order have been used. The polynomial fit was then subtracted from the raw data to obtain the oscillatory part of the signal. Typical $1/B$-periodic oscillations are depicted in Fig. 3.11 (b). Because data points were typically recorded in equidistant steps in B, while the oscillations are periodic in $1/B$, the data was interpolated on an equidistant set of points in $1/B$ prior to the frequency analysis. The spacing was chosen to match the spacing of the data points recorded at the highest fields.

Before analyzing the frequency spectrum with a Fast Fourier Transform (FFT), the following steps were taken in order to reduce effects of the finite field range, in which quantum oscillations are detected. First, the data range $1/B$ was padded with zeros on both sides. While these zeros do not add any information to the signal, the artificially increased data range increases the sampling rate of the FFT algorithm, thereby allowing for a more precise determination of the oscillation frequencies. An illustration of this effect is shown in Fig. 3.11 (c). We note that the width of the

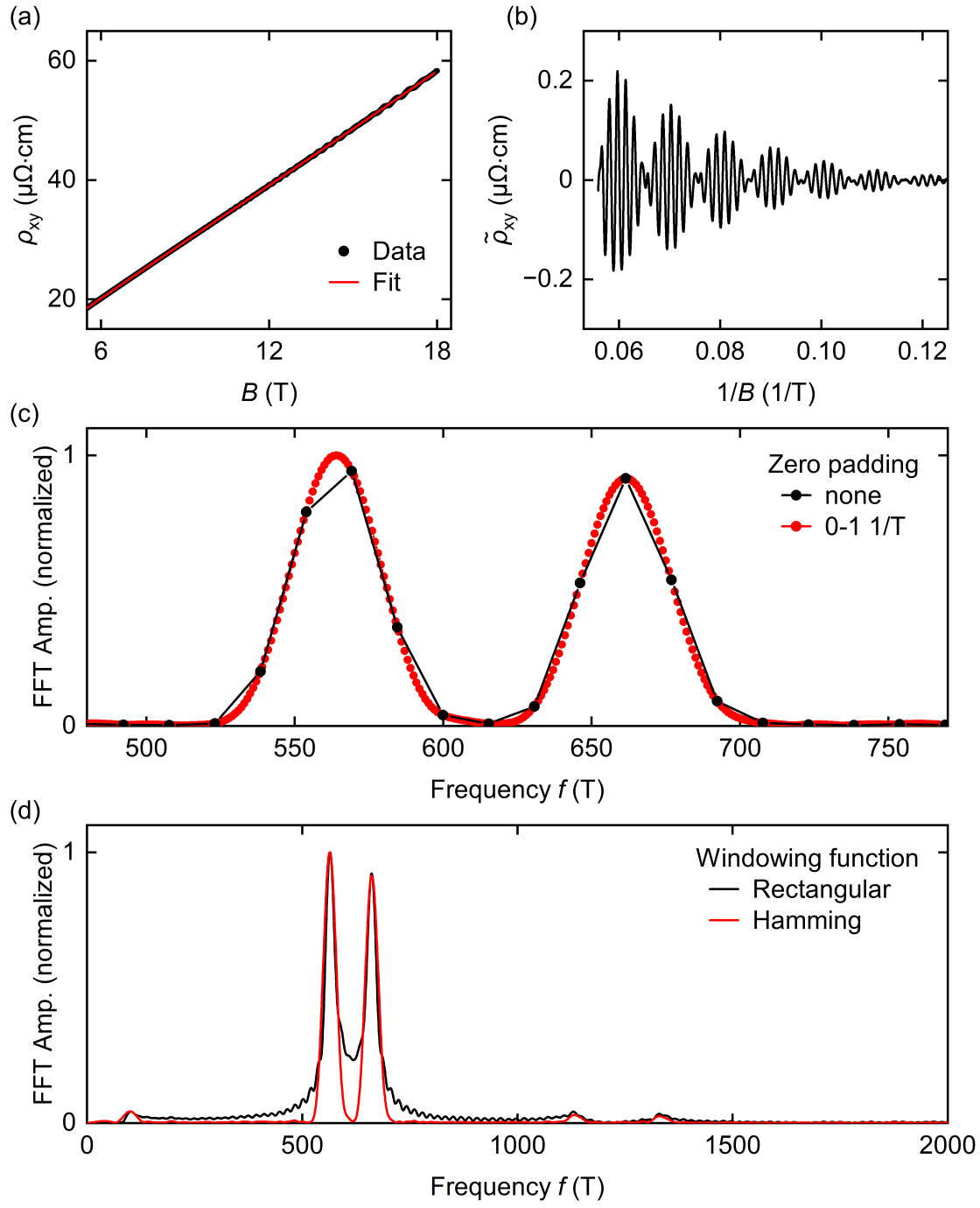

Figure 3.11: Data analysis. (a) Typical data set of the Hall resistivity ρ_{xy} as a function of the applied magnetic field B. The monotonically increasing, non-oscillatory part of the signal is approximated by a polynomial fit. (b) Oscillatory part of the resistivity $\tilde{\rho}_{xy}$ as a function of inverse applied field following a subtraction of the non-oscillatory background. (c) FFT spectra of the data shown in panel b with and without zero padding. The sampling rate is increased substantially through the use of zero padding resulting in a smoother shape of the detected peaks. (d) FFT spectra of the zero-padded data shown in panel b with and without the application of a Hamming window. Through the use of a windowing function spectral leakage from the oscillation frequencies present in the signal is reduced significantly.

peaks is independent of zero padding and is determined by the number of oscillations in the field range, in which the data is analyzed. With zero padding, however, the maximum of the peaks can be identified with higher accuracy.

The second technique we employed is the use of a windowing function. At the edges of the field range, in which data was recorded, the data shown in Fig. 3.11 (b) exhibits a sharp transition to the added zeros. This results in so-called spectral leakage, that can be seen as side lobes in the Fourier spectra. The effect can be mitigated by multiplying the data with a windowing function, that smooths the sharp transitions at the boundaries of the field range. We tested different windowing functions (Hann, Hamming, Gaussian) and found the Hamming window to work best in reducing side lobes close to the main peaks, thereby allowing to resolve frequencies, which are close to each other. The suppression of spectral leakage through the use of a windowing function is illustrated in Figure 3.11 (d).

We note that the amplitudes of the peaks in the FFT spectra depend on the field range and windowing function used. Therefore, wherever amplitudes are compared between different measurements, e.g., for the analysis of the temperature damping factor R_T, the same windowing function and field range was applied to all datasets.

The peaks in the FFT spectra were fitted using Gaussians to analyze their amplitudes and frequencies. We note that the standard deviation of this fit underestimates and the full width at half maximum (FWHM) overestimates the uncertainty of the extracted frequencies. For the measurements performed in our lab, we typically recorded datasets for both increasing and decreasing magnetic field at a particular set of parameters. Therefore, a comparison of the values obtained from both measurements can be used as an estimate for the uncertainty. In our high-field experiments only one measurement, either for increasing or decreasing magnetic field, was performed for a given set of parameters and the uncertainty of the extracted QO amplitudes and frequencies was estimated from the noise floor of the FFT close to the analyzed peak.

The following steps have been taken to differentiate weak frequency contributions from noise. The data obtained under increasing and decreasing magnetic field were compared. Only features that were consistently detected in both sweep directions were considered as intrinsic contributions originating from the sample. Polynomials of different degree have been subtracted from the raw data. This typically alters the

FFT spectra in the low-frequency region and only peaks which do not vary with the background subtraction were considered as possible QO frequencies. Different windowing functions have been employed to rule out artifacts arising from spectral leakage. The data was analyzed for different field ranges and only peaks that increase in amplitude when the field range is shifted towards higher fields are considered as possible QO frequencies. Finally, when performing angular dependent measurements, the traceability of a specific peak over a series of adjacent angles was taken into account in the identification of frequency branches.

4 Network of Topological Charges

In the study of topological semimetals the explanation of many phenomena focuses on a description via pairs of band degeneracies with opposite chirality [18, 32]. While this approach has proven successful in a wide range of materials, there are many examples of band structures featuring an abundance of distinct topological crossings. The crossings may occur between large sets of bands making them interconnected, i.e., they are forming a network of topological charges. This raises the question of how topological charges in these systems interact and if a description via isolated pairs of degeneracies of opposite chirality adequately describes the global band topology.

The class of non-magnetic, chiral compounds crystallizing in SG 198, including CoSi, RhSi, PdGa, and PtAl [60, 73–76, 78, 88, 91], is a prime example for an intricate network of interconnected topological charges. The band structure in these materials hosts multifold, symmetry-protected band crossings located at the Γ- and the R-point of the simple cubic Brillouin zone (BZ), movable Weyl points along high-symmetry lines, accidental Weyl points located throughout the BZ [60, 73, 75, 99], and symmetry-enforced degeneracies on the BZ boundary termed nodal planes (NPs) [30, 94, 95]. The discovery of NPs in the ferromagnetic state of MnSi [100], which is described by a magnetic subgroup of SG 198, and the realization that they carry a topological charge raises the question of their relevance for the band topology in its non-magnetic counterparts.

To quantitatively calculate topological responses, a precise knowledge of the Fermi surface with respect to the location of topological degeneracies and the flux of Berry curvature between them is essential. Qualitative features, such as the existence or number of Fermi arc surface states [33, 198], can be inferred from the presence and location of topological crossings. However, for a quantitative prediction of topological effects, such as the intrinsic spin Hall effect [55, 136] or the circular photogalvanic effect [51, 90, 199, 200], integration of the flux of Berry curvature through the Fermi surface is required. In materials with multiple interconnected band degeneracies, this underscores the importance of considering the global band topology.

In the work presented in this chapter, we report on the semimetallic compound CoSi. We show an overview of the magnetic and magnetotransport properties followed by detailed studies on the Shubnikov-de Haas (SdH) and de Haas-van Alphen (dHvA) effect. We first focus on the part of the quantum oscillation spectrum related to

FS pockets around the R-point and compare it to the ab-initio calculated band structure. Then, we show results on the SdH and dHvA effect in samples with improved crystalline quality and describe the part of the spectrum arising from FS pockets located around the Γ-point. Finally, we discuss the implications of our findings for the global band topology in CoSi and the relation of topological crossings to the Fermi surface.

4.1 Magnetic and electric properties

We begin the discussion of our experimental results with an overview of the magnetic and magnetotransport characteristics of CoSi.

4.1.1 Magnetic properties

The magnetic properties of CoSi were analyzed using a vibrating sample magnetometer (VSM). All samples investigated in this thesis exhibit a qualitatively similar behavior and we focus our discussion on the most extensively characterized sample HKZ7 S1 here.

Shown in Figure 4.1 (a) is the specific moment, μ, as a function of the applied magnetic field along the [110] crystallographic direction at various temperatures between 400 K and 1.8 K. The magnetization can be described by two separate contributions. At temperatures exceeding 75 K, the curves display a tilted S-shape with a paramagnetic component at low fields, which rapidly saturates with increasing field. The second contribution is diamagnetic and dominates the magnetization at higher fields. With decreasing temperature, the diamagnetic signal weakens and eventually transitions to an increasingly strong paramagnetic response.

We first focus on the saturating part of the magnetization. A close-up view of the low-field magnetization is shown in Fig. 4.1 (b). In the entire temperature range investigated, the magnetization exhibits a hysteresis indicative of ferromagnetic or spin glass behavior. The hysteresis loop displays a clear two-step behavior and significantly broadens upon decreasing the temperature. Interestingly, the remanence is nearly temperature independent. In contrast, the coercive field increases with decreasing temperature.

The saturating part of the magnetization can be isolated within the temperature range at which the high-field response is diamagnetic. By fitting the slope of the magnetization in the field range between 4 T and 7 T, we determine the diamagnetic

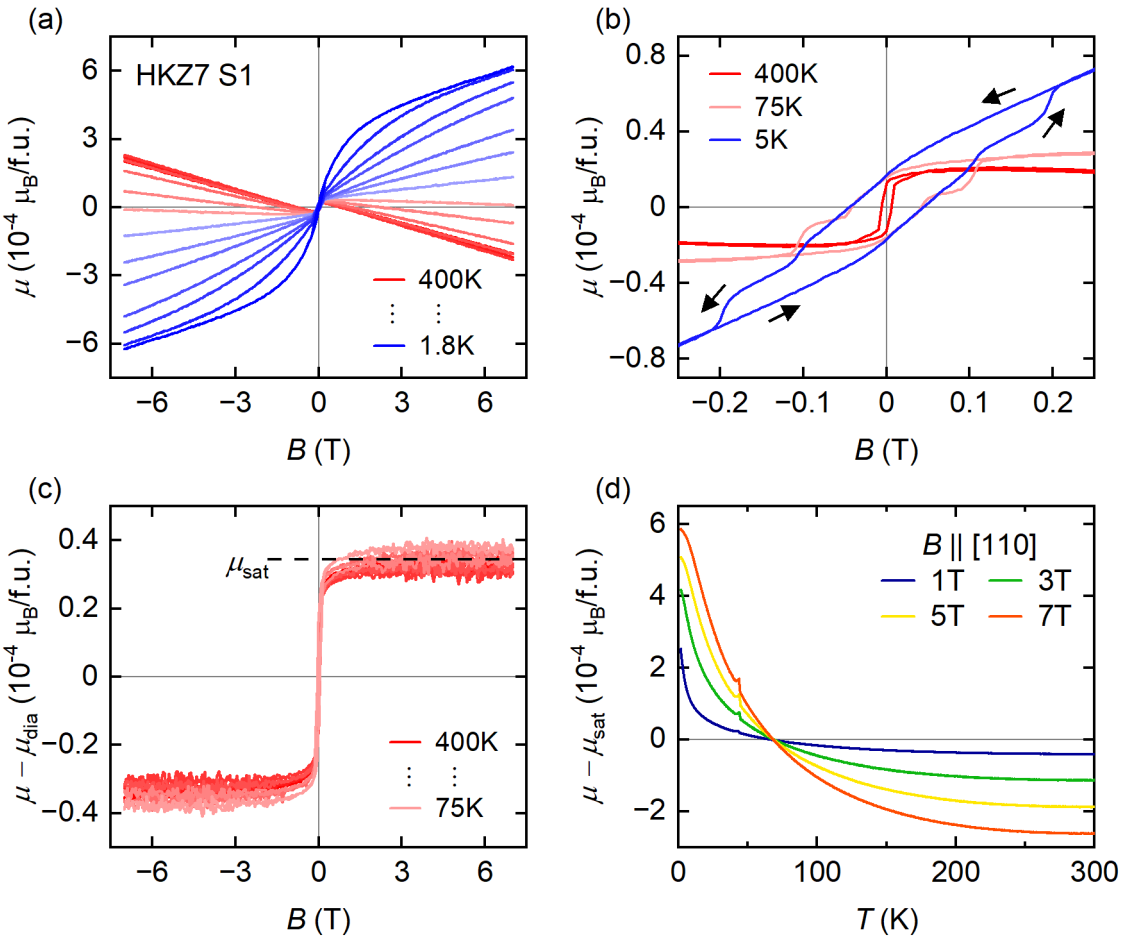

Figure 4.1: Magnetic properties of CoSi. (a) Specific moment, μ, as a function of applied magnetic field along the [110] crystallographic orientation at different temperatures. The diamagnetic response weakens with decreasing temperature and becomes paramagnetic below 70 K. (b) Close-up view of the low-field region of the data shown in (a) for selected temperatures. All curves exhibit a hysteresis loop with a step-like behavior, which broadens with decreasing temperature. While the remanent moment stays nearly constant, the coercive field increases with decreasing temperature. Arrows indicate the sweep direction. Zero-field cooled curves are not shown for clarity. (c) Specific moment, μ, after subtraction of the diamagnetic response μ_{dia} (see text for details). A temperature independent saturated moment of $\mu_{\mathrm{sat}} = 0.35 \times 10^{-4}\,\mu_{\mathrm{B}}$/f.u. is found between 400 K and 75 K. (d) Specific moment, μ, as a function of temperature for different applied magnetic fields after subtracting μ_{sat}. All curves show the change from diamagnetic to paramagnetic behavior with decreasing temperature. For the largest fields the magnetization starts to saturate below 15 K. The peak-like feature at ≈45 K is likely an experimental artifact related to trapped O_2 in the setup. All curves intersect at a temperature of 70 K, coinciding with the change from diamagnetic to paramagnetic behavior.

contribution to the moment μ_{dia}. The saturating part of the magnetization, shown in Fig. 4.1 (c), can then be obtained by subtracting μ_{dia} from the total magnetization. The hysteresis loop closes for fields above 200 mT and the signal saturates for fields above 1 T with an almost temperature independent saturated moment of $0.35 \times 10^{-4}\,\mu_{\mathrm{B}}$/f.u.. This behavior has been attributed to Fe impurities commonly found in CoSi samples [201, 202]. Using the effective magnetic moment of free Fe^{3+} ions of $5.9\,\mu_{\mathrm{B}}$, we estimate the iron impurity concentration in our sample to be on the order of 6 ppm, consistent with the expected Fe concentration based on the purity of the starting materials utilized in the crystal synthesis.

Next, we analyze the non-saturating part of the magnetization. Fig. 4.1 (d) depicts the specific moment as a function of temperature at various applied magnetic fields. All curves exhibit a diamagnetic response at elevated temperatures, which weakens with decreasing temperature. The curves intersect at 70 K, marking the transition from diamagnetic to paramagnetic behavior. At the highest recorded field, the paramagnetic response begins to saturate below 15 K. The peak-like feature observed at $\approx$45 K, visible in all curves, is likely an artifact resulting from trapped oxygen in the varnish used to attach the sample to the sample holder. A possible explanation for the change from diamagnetic to paramagnetic behavior is the formation of localized moments on crystal defects at low temperatures, as proposed in Refs. [153, 202].

4.1.2 Magnetotransport properties

To investigate the magnetotransport properties of CoSi, we recorded both the longitudinal and transverse voltage drops across our samples. This allows us to deduce the two components of the resistivity tensor, ρ_{xx} and ρ_{xy}, respectively. In the measurements presented here, the magnetic field is oriented perpendicular to the applied current, thereby probing the transverse magnetoresistance and the conventional Hall effect.

The magnetotransport properties are qualitatively similar for all samples investigated and we focus our discussion on the most extensively characterized sample HKZ7 S1. In addition to the standard six-point configuration of the Hall bar geometry, in which the voltages at the edge of the sample are recorded, we attached longitudinal voltage contacts along the center (spine) of the sample (see Sec. 3.3.1 for details). This configuration enables the investigation of potential effects arising from an inhomogeneous current distribution through the sample, commonly referred to as current jetting.

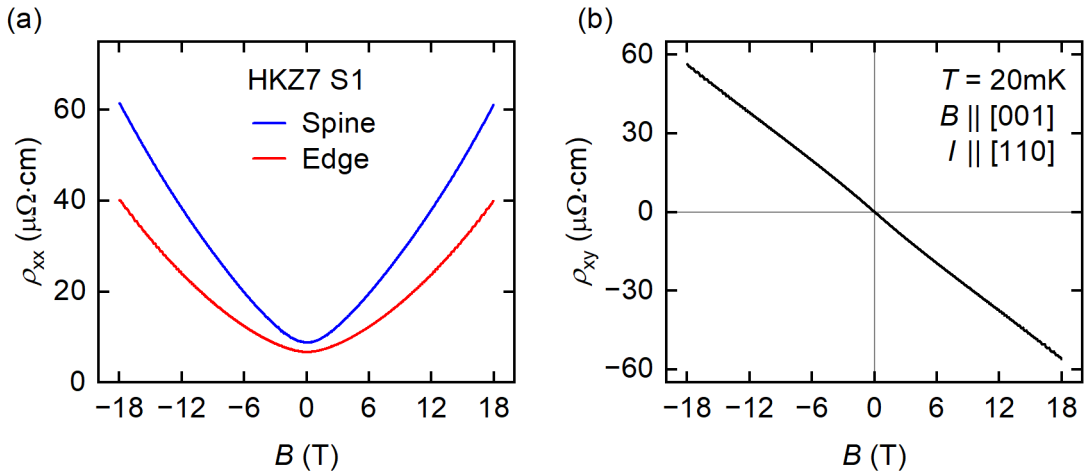

Figure 4.2: Magnetotransport properties. (a) Longitudinal resistivity, ρ_{xx}, detected at the center (spine) of the sample and close to the sample edge as a function of the applied magnetic field B. Both signals exhibit an almost quadratic, non-saturating magnetoresistance. (b) Hall resistivity, ρ_{xy}, as a function of B. The almost linear behavior exhibits a slight S-shape at low fields. The sign of ρ_{xy} indicates predominantly electron-like charge carriers. All signals exhibit pronounced quantum oscillations for fields exceeding 5 T.

Figure 4.2 (a) shows the resistivity, ρ_{xx}, as a function of the applied magnetic field B, as inferred from the recorded voltage at the spine and the edge of the sample. Both signals exhibit an almost quadratic increase with B. A slightly larger resistivity is detected at the spine of the sample at zero field and the magnetoresistance (MR) at 18 T amounts to 700 % at the spine and 600 % at the edge of the sample. This disparity may be a sign of an inhomogeneous current distribution [203], where a higher current density near the center of the sample induces a greater voltage drop and hence a higher inferred resistivity.

The Hall resistivity, ρ_{xy}, as a function of B is depicted in Fig. 4.2 (b). It displays an almost liner dependence on B with a slight S-shape at low fields. The sign of ρ_{xy} indicates predominantly electron-like charge carriers contributing to the Hall effect. Employing a simple one-carrier model to fit to the Hall conductivity $\sigma_{xy} = -\rho_{xy}(\rho_{xx}^2 + \rho_{xy}^2)^{-1} = (n_e e \mu_e^2 B)(1 + (\mu_e B)^2)^{-1}$, where e is the electron charge, yields a carrier density of $n_e = 1.48 \times 10^{20}\,\mathrm{cm}^{-3}$ and electron mobility of $\mu_e = 563\,\mathrm{cm}^2\,\mathrm{V}^{-1}\,\mathrm{s}^{-1}$, consistent with what is reported in the literature [138]. Deviations from linearity at low fields may be induced by the influence of additional hole-like charge carriers, as expected from the semi-metallic band structure of CoSi. Due to the low mobility of the hole-like quasiparticles, no reliable fits could be achieved when using a two-band model. However, the non-saturating magnetoresistance up to fields of 18 T

suggests that CoSi is an almost perfectly compensated semimetal. All signals exhibit characteristic oscillations for fields exceeding 5 T, which are analyzed in detail in the following.

4.2 Fermi surface around the R-point

Next, we analyze the oscillations observed in the longitudinal resistivity, ρ_{xx}, and Hall resistivity, ρ_{xy}, of CoSi. Here, we focus on data recorded with a sample obtained from an optical floating zone growth, exhibiting a residual resistivity ratio of 16, and two dominant QO frequencies, which arise from the Fermi surface around the R-point. First, we compare the oscillations detected from the three distinct voltage pick-ups recorded for this sample. Then, we present the temperature and angular dependence of the oscillation frequencies detected in ρ_{xx}. We match them to extremal trajectories on Fermi surface pockets around the R-point and discuss the relevance of nodal planes and SOC for the spectra.

4.2.1 Quantum oscillation spectra

All three signals depicted in Fig. 4.2 exhibit quantum oscillations for fields exceeding 5 T. To analyze the oscillations, the non-oscillatory background of the magnetoresistance and Hall resistivity was fitted with polynomials and subsequently subtracted from the data. The oscillatory component of the signal $\tilde{\rho}$ is shown in Fig. 4.3 (a). While all signals exhibit oscillations with identical frequencies and phase, the amplitudes of these oscillations vary among them. At high fields the Hall resistivity ρ_{xy} exhibits the largest oscillation amplitudes, closely followed by ρ_{xx} measured along the edge of the sample. The oscillations amplitudes detected for ρ_{xx} measured along the spine of the sample show significantly reduced oscillation amplitudes. We note that ρ_{xy} exhibits additional linear dependence on B as compared to ρ_{xx}, accounting for the larger oscillation amplitudes at high fields. Upon removal of this additional linear dependence by considering $\tilde{\rho}_{xy}/B$ instead of $\tilde{\rho}_{xy}$, the oscillation amplitudes of all signals follow the same field dependence.

The $1/B$-periodicity of the oscillations is illustrated in Fig. 4.3 (b). The oscillations exhibit a characteristic beating pattern, indicative of two close-by frequencies with similar amplitude dominating the spectrum. The oscillations are analyzed in a field range between 9 T and 18 T using a Fast Fourier Transform (FFT). Technical details are described in Section 3.4. The resulting frequency spectrum is depicted in Fig. 4.3 (c).

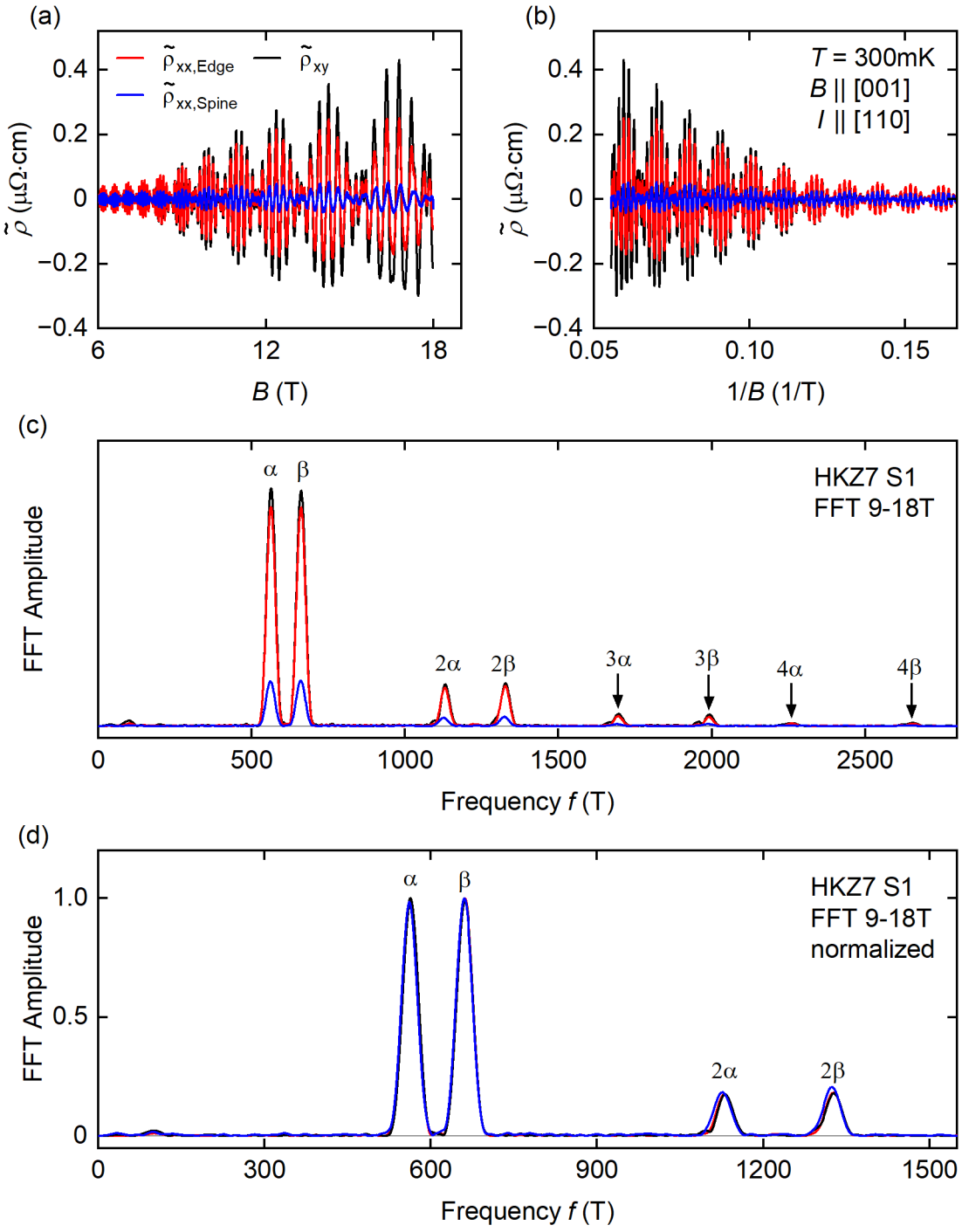

Figure 4.3: Shubnikov-de Haas oscillations. (a) Oscillatory part of the resistivity, $\tilde{\rho}$, as a function of the applied magnetic field, B, after subtraction of a polynomial from the data shown in Fig. 4.2. (b) Data shown in (a) as a function of $1/B$ exhibiting periodic oscillations. (c) Fourier spectrum of the data shown in (b) analyzed in the field range between 9 T and 18 T. Two main frequencies α and β as well as their higher harmonics are detected. (d) Data shown in (c) normalized to the highest peak detected for each signal. All curves fall almost perfectly onto each other.

All signals exhibit qualitatively identical spectra, differing only in amplitude. We illustrate this point by showing the FFT spectra normalized to the highest peak for each signal in Fig. 4.3 (d). Given that the noise level is similar for all three signals, but the oscillations are significantly weaker in the longitudinal voltage pick-ups along the spine of the sample, we focus on the Hall resistivity, ρ_{xy}, and the signal obtained from the edge contacts in the following and simply denote the latter by ρ_{xx} for better readability.

Two prominent frequencies $f_\alpha = 565\,\mathrm{T}$ and $f_\beta = 663\,\mathrm{T}$, as well as their higher harmonics (2α, 2β, ...), are detected. These frequencies have been consistently observed in various studies [138–142] and their origin is attributed to quasiparticle orbits on Fermi surface pockets around the R-point of CoSi, as discussed in detail in Sec. 4.2.2.

A slight asymmetry of the peaks, with additional weight towards the low-frequency side, is discernible for the higher harmonics. In Ref. [142], the authors attribute this asymmetry to a splitting of the main frequencies f_α and f_β on the order of 10 T. Conversely, in Ref. [138] the data was explicitly analyzed for a potential splitting of the peaks and the authors concluded that no splitting larger than 2 T is present. Upon comparison of the FFT spectra obtained from different samples varying in crystalline quality, we find that no frequency splitting is observed in samples of the highest crystalline quality (see Fig. 4.8). We therefore conclude that the asymmetry of the peaks, which has been interpreted as a splitting of the two main frequencies, is not an intrinsic property of CoSi but rather a sample-dependent phenomenon related to defects in the crystal.

Next, we analyze the temperature dependence of the oscillation amplitudes with the magnetic field applied along the crystallographic [001] direction. This orientation allows us to determine both the longitudinal and Hall resistivity simultaneously. Figure 4.4 (a) and (b) show FFT spectra obtained at selected temperatures between 20 mK and 10 K from the ρ_{xx} and ρ_{xy} data. Both signals exhibit qualitatively the same temperature-dependent damping of the oscillation amplitudes of f_α and f_β, as well as their higher harmonics. While the fundamental frequencies remain detectable up to a temperature of 8 K, their harmonics experience stronger damping, consistent with LK theory. Figure 4.4 (c) shows the extracted FFT amplitudes as a function of temperature for the ρ_{xx} data. The solid lines represent fits with the LK temperature reduction factor R_T. The obtained cyclotron masses are $m_\alpha = (0.92 \pm 0.01)\, m_e$

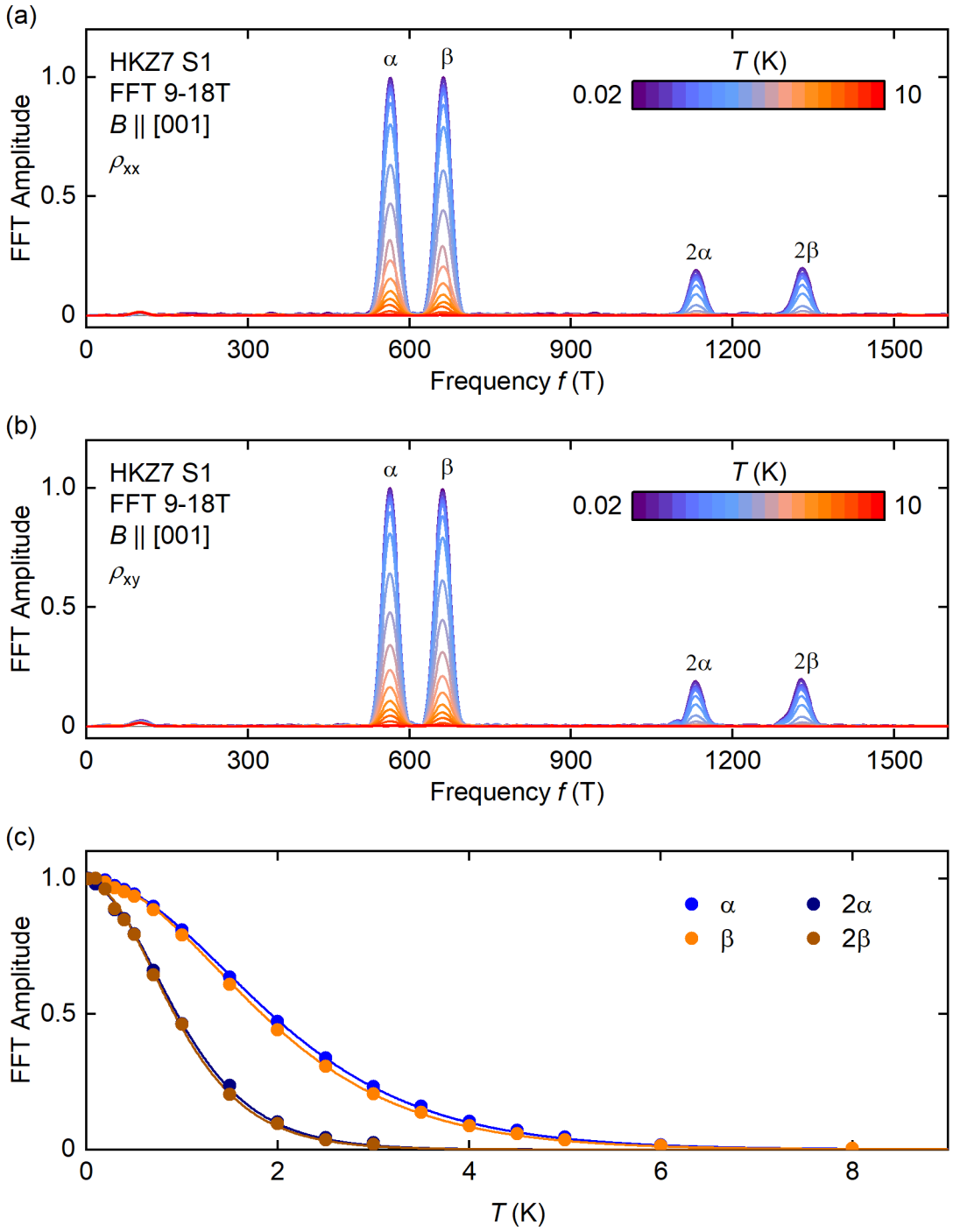

Figure 4.4: Temperature dependence of SdH oscillations. Fourier spectra of the SdH oscillations in ρ_{xx} (a) and ρ_{xy} (b) recorded at various temperatures between 20 mK and 10 K. Both signals experience nearly identical temperature dependent damping of the oscillation amplitudes. (c) FFT amplitudes of the fundamental frequencies f_α and f_β as well as their second harmonics as a function of temperature extracted from the ρ_{xx} data. Error bars are smaller than the data points. Solid lines represent fits of the LK temperature damping factor yielding cyclotron masses of $m_\alpha = (0.92 \pm 0.01)\, m_e$ and $m_\beta = (0.96 \pm 0.01)\, m_e$.

and $m_\beta = (0.96 \pm 0.01)\, m_e$ for the ρ_{xx} data and $m_\alpha = (0.92 \pm 0.01)\, m_e$ and $m_\beta = (0.95 \pm 0.01)\, m_e$ for the ρ_{xy} data. The stated uncertainties correspond to the standard errors of the fits.

An analysis of the second harmonics of f_α and f_β, taking into account the stronger damping due to the higher harmonic index p, yields consistent results within the experimental error. We note that for the harmonics of higher order, a slightly smaller cyclotron mass is obtained. This systematic deviation is explained by the finite field range in $1/B$ utilized in the analysis, as discussed in more detail in Section 3.4. For a comparison with theoretical calculations, we consider the cyclotron masses obtained from the analysis of the fundamental frequencies and estimate the uncertainty introduced by systematic errors to be approximately 5 %.

The dependency of the observed QO frequencies on the direction of the applied magnetic field provides further insights into the Fermi surface geometry. To alter the field direction with respect to the crystallographic orientation, the sample was rotated in a $(1\bar{1}0)$ plane, with the angle θ measured from the [001] direction. Given that the contact geometry was chosen such that the current I is also applied along the $[1\bar{1}0]$ direction, this arrangement allows for maintaining $B \parallel I$, thereby retaining the transverse magnetoresistance configuration for ρ_{xx}. In contrast, the geometry of the ρ_{xy} contacts changes upon sample rotation. The conventional Hall effect, where $I \perp B \perp U$, is only realized for field applied along the [001] direction (or equivalently $\theta = 0°$). Upon rotation, the voltage pick-ups are rotated towards the magnetic field direction, resulting in a $\cos(\theta)$ dependence of the ρ_{xy} signal. Therefore, ρ_{xx}, which exhibits a large signal independent of θ, was chosen in the analysis of the angular dependence of oscillation frequencies.

The resulting frequency spectra within the angular range between $-10°$ and $190°$ are presented in Fig. 4.5 (a). The frequencies f_α and f_β exhibit only small changes with the angle of the applied magnetic field. To visualize the dispersion more clearly, a colormap of the FFT amplitudes as a function of frequency and angle is depicted in Fig. 4.5 (b). While the variation of the frequencies with respect to θ is indeed small, a distinct dependence can be discerned. Frequencies f_α and f_β display global minima at $\theta = 0°$ and $180°$, maxima at $\theta = 55°$ and $35°$, and a local minimum at $\theta = 90°$. The overall symmetry is consistent with the crystalline symmetries. The largest variation of f_β amounts to 9 T, slightly exceeding the 5 T variation detected for f_α.

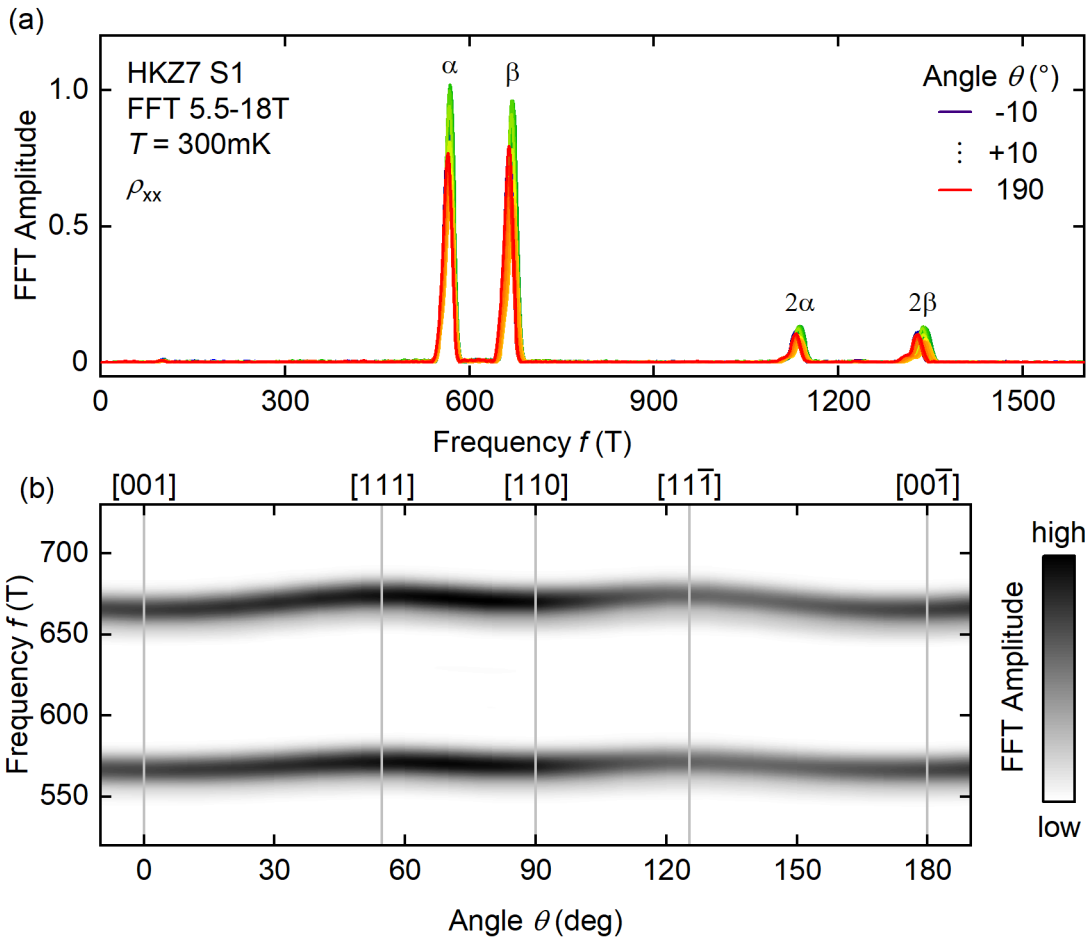

Figure 4.5: Angular dependence of the SdH oscillations. (a) Fourier spectra of the SdH oscillations in ρ_{xx} recorded in the angular range between $\theta = -10°$ and 190° at $T = 300\,\mathrm{mK}$. (b) FFT amplitudes as a function of frequency and angle shown as a colormap. Angles corresponding to high-symmetry directions of the crystal lattice are marked by vertical lines. Both frequency branches α and β exhibit only a small angular dispersion, which follows the symmetry of the crystal lattice.

4.2.2 Fermi surface trajectories

The two observed frequency branches α and β originate from the intersecting FS pockets centered around the R-point of CoSi. The cross-sectional areas of extremal trajectories on the FS are directly proportional to the observed QO frequencies via the Onsager relation (see Eq. 2.23). We consider different scenarios, for which we calculate the expected frequencies from the band structure, presented in Sec. 2.2, both with and without the inclusion of SOC and with and without consideration of the NPs on the BZ boundary. Additionally, we include the effect of magnetic breakdown. Our analysis reveals that the only scenario consistent with the experimental data requires the inclusion of SOC, NPs, and magnetic breakdown.

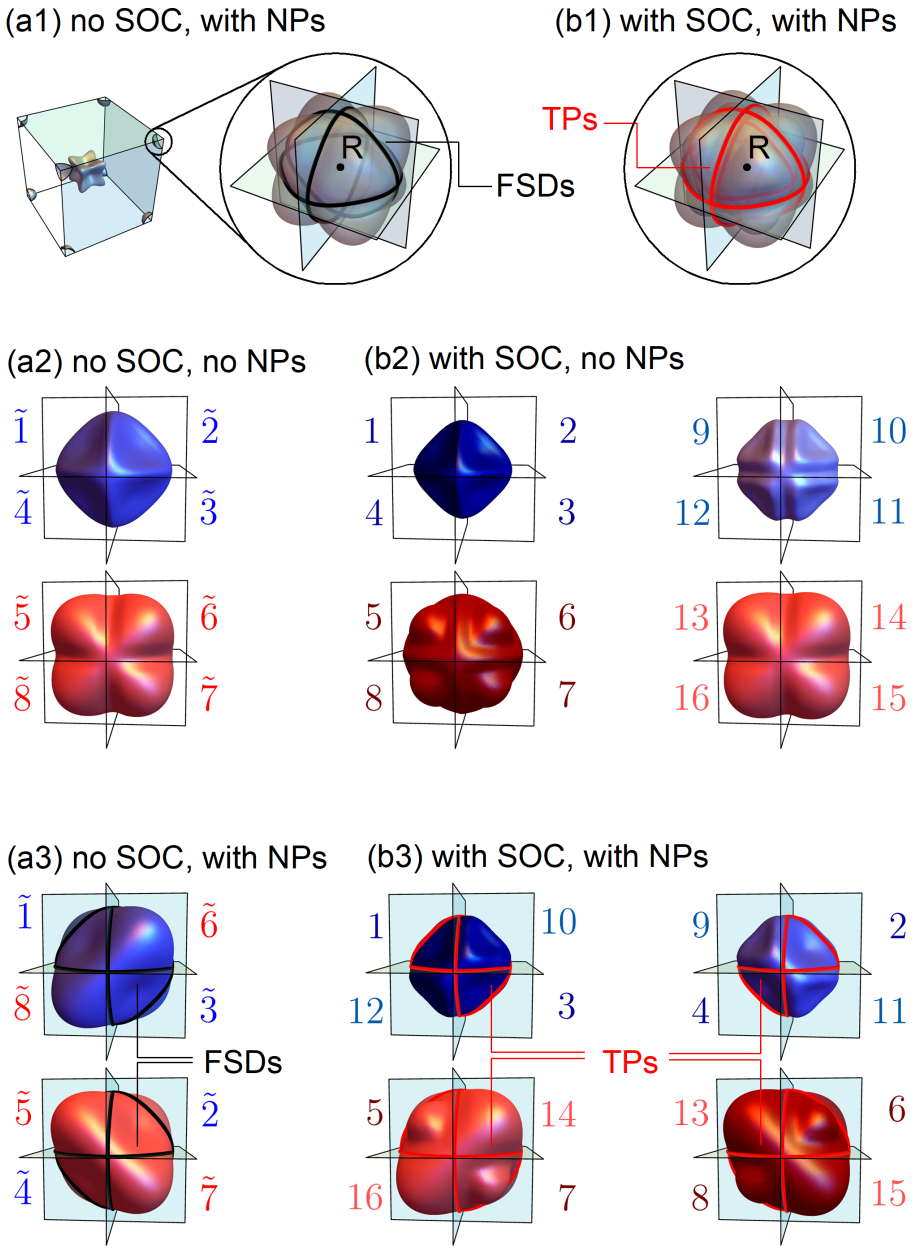

Figure 4.6: Fermi surface of CoSi centered around the R-point. FS sheets of CoSi at the R-point without (a1) and with (b1) SOC. Without SOC, there are two electron-like FS sheets intersecting each other at Fermi surface degeneracies (FSDs) on the BZ boundary. With SOC, the two sheets split into two pairs of sheets, which are pairwise degenerate on topological protectorates (TPs). (a2), (a3) Influence of nodal planes on the band connectivity in the case without SOC. If the bands are simply labeled by increasing order of energy, the resulting FS sheets are shown in (a2). However, due to the degeneracies on the NPs, the connectivity changes, such that upon crossing the BZ boundary, the band that is lower in energy on one side is connected to the band that is higher in energy on the opposite side. (b2), (b3) FS sheets around the R-point with SOC. There are two pairs of FS sheets. The degeneracy at the NPs combines them into two intersecting inner sheets (blue) and two intersecting outer sheets (red).

To illustrate the effects of SOC and the influence of NPs on the band connectivity, we show a comparison between the FS pockets for different scenarios in Figure 4.6. We first discuss the case without SOC, which can be easily generalized to the situation including SOC. The vicinity of the R-point can be described by eight octants situated in neighboring BZs. If we label the bands in order of increasing energy in each octant, we end up with the FS sheets shown in Fig. 4.6 (a2). The FS would comprise one inner and one outer sheet that touch, but do not intersect, each other on the BZ boundary. This situation would occur if there was an infinitesimally small avoided crossing of bands at the BZ boundary. However, considering the enforced degeneracy at the nodal planes, the FS sheets do intersect each other. Consequently, the sheet closer to the R-point in one octant connects to the sheet farther away from the R-point in neighboring octants, and vice versa. This situation is illustrated in Fig. 4.6 (a3). Spin-orbit coupling splits the sheets into two pairs of sheets for which the same rationale applies. The two inner sheets, depicted in blue in Figs. 4.6 (b2) and (b3), intersect at the nodal planes, as do the two outer sheets drawn in red.

Distinct differences in the quasiparticle trajectories are expected from non-intersecting FS sheets without nodal planes and the FS sheets which emerge when the enforced degeneracies on the BZ boundary are taken into account correctly. The calculated frequency branches for the various scenarios, along with their corresponding extremal FS trajectories perpendicular to the [001] and [110] direction, are shown in Figure 4.7. A rigid upwards band shift of 30 meV has been applied to the bands around the R-point to yield a better match between theory and experiment. We note that this procedure only shifts all frequencies towards lower values and has no effect on the number and only a small influence on the dispersion of predicted frequency branches. For the illustrations of the trajectories, a circle centered at the R-point has been subtracted to enhance the visibility of the small differences between them. A colormap representing the experimentally determined frequency branches is shown in the background for comparison.

We first consider the case in which both SOC and the correct band connectivity at the NPs are neglected. In this scenario, the Fermi surface (FS) would comprise two nested pockets, as illustrated in Fig. 4.6 (a2), which touch, but do not intersect, at the Brillouin Zone (BZ) boundary. The extremal FS trajectories perpendicular to the [001] direction lie in the plane where the FS pockets touch, with the inner pocket exhibiting a maximal cross-sectional area and the outer pocket exhibiting a minimal cross-sectional area. Both enclose the same cross-sectional area and therefore

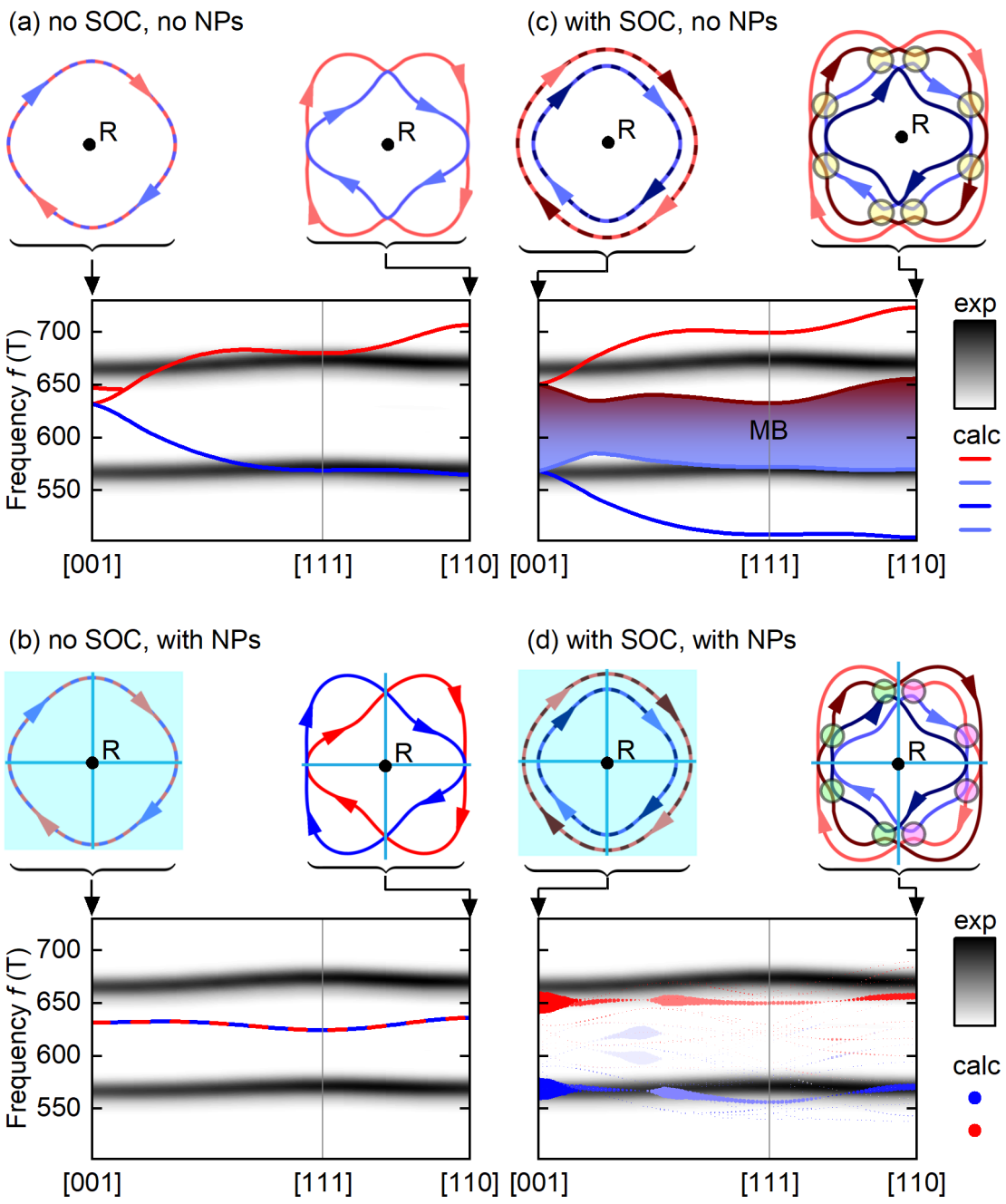

Figure 4.7: Comparison between experimentally detected and calculated QO frequencies arising from the R-point. Experimental SdH branches are shown as a colormap in the background, calculated frequencies are illustrated as colored lines. An R-centered circle was subtracted from the corresponding extremal FS trajectories for the [001] and [110] direction for better visibility. Magnetic breakdown junctions are marked by colored circles. Four different scenarios are considered: (a) Without SOC and without NPs. (b) Without SOC including NPs. The NPs are marked in cyan. (c) With SOC and without NPs. Up to 12 magnetic breakdown junctions lead to a multitude of possible breakdown frequencies in the shaded MB area. (d) Including both SOC and NPs. Here, the breakdown branches are calculated explicitly. The symbol size reflects the probability of a particular breakdown branch resulting in two strong, almost dispersionless frequency branches.

lead to the same expected QO frequency. With the magnetic field applied close to the [001] direction, the outer FS pocket has two further degenerate maximal cross sections above and below the plane containing the R-point. They would give rise to a slightly larger QO frequency, as can be seen in the small splitting of the predicted frequency branch shown in red in Fig. 4.7 (a). Upon field rotation, both pockets exhibit a single maximal cross section that varies with the angle of the applied field. Therefore, two dispersive frequency branches would be expected away from the [001] direction. Over a limited angular range, this case resembles what is seen in experiment, explaining why some earlier studies, that have not taken into account the NPs [138, 139], considered SOC to be irrelevant in CoSi. Upon closer examination, however, this scenario fails to consistently explain the experimental data across the entire angular range.

Next, we discuss how the NPs change the predicted frequency branches in the absence of SOC. The corresponding FS pockets are depicted in Fig. 4.6 (a3). Importantly, these pockets do not comprise an inner and outer pocket, but rather two symmetry-related intersecting pockets. The extremal trajectories perpendicular to the [001] direction are still located in the plane at which both pockets intersect, i.e., the NP, resulting in a single QO frequency. No additional extremal orbits are anticipated above or below the NP. Upon rotation of the field, each FS pocket gives rise to one extremal orbit. However, due to their symmetry, both trajectories enclose identical cross-sectional areas, as illustrated for the [110] direction in Fig. 4.7 (b). Consequently, across the entire angular range, a single frequency branch would be expected from the two intersecting FS pockets, which contradicts the experimental observations.

Incorporating SOC in the band structure calculations results in a splitting of the two FS pockets around the R-point into four distinct pockets. If the band connectivity at the NPs is not taken into account correctly, a small splitting of the highest frequency branch close to the [001] direction would be expected, as in the case neglecting SOC. Upon rotation of the field, the four FS pockets would give rise to four extremal trajectories enclosing different areas, thereby yielding four distinct QO frequencies. The trajectories on the two FS pockets in between the innermost and outermost pocket closely approach each other at several points within the BZ. These points are highlighted by yellow circles in Fig. 4.7 (c) and allow for a magnetic field-induced tunneling of quasiparticles from one orbit to another, called magnetic breakdown (MB). Given the FS geometry consisting of multiple nested pockets, MB leads to breakdown trajectories enclosing an area in between the area of the

participating orbits. Consequently, additional breakdown branches situated between the two intermediate frequency branches would be anticipated in the predicted frequency spectrum, as indicated by the shaded region. However, neither four distinct frequency branches nor two outer frequency branches accompanied by multiple magnetic breakdown branches in between are experimentally observed.

Finally, we consider the case where both SOC is included and the band connectivity at the NPs is correctly taken into account. This situation is illustrated in Fig. 4.7 (d). With the magnetic field applied along the [001] direction, the extremal orbits on the four FS sheets shown in Fig. 4.6 (b3) reside directly on the nodal plane, resulting in pairwise degeneracy. Consequently, they give rise to two expected oscillation frequencies. Upon rotation of the field, the extremal orbits comprise two sets of orbits intersecting at the NPs. The two inner orbits (depicted in blue) and the two outer orbits (depicted in red) pairwise enclose the same cross-sectional areas, thereby yielding a total of two frequency branches across the entire angular range, consistent with experimental observations. However, the anticipated dispersion of the two frequency branches is larger than observed experimentally. Accounting for the proximity of the inner and outer sets of orbits at MB junctions, we find additional breakdown trajectories producing frequencies lying between those expected for the orbits without MB. We explicitly calculate the probabilities for each breakdown trajectory, as indicated by the symbol size of the predicted frequencies in Fig. 4.7 (d). The largest probability lies on two almost dispersionless frequency branches, consistent with the experimental observations. We note that in Ref. [140] the authors calculate the angular dispersion assuming complete MB at every breakdown junction and obtain consistent results.

In summary, the understanding of the quantum oscillation spectrum of CoSi arising from FS pockets around the R-point requires SOC and the presence of NPs. The small dispersion of the two observed frequency branches is explained by MB at further points along the quasiparticle trajectories.

4.3 Fermi surface around the Γ-point

In this section, we report on quantum oscillations in a sample exhibiting an improved crystalline quality. We first show oscillations in the Hall resistivity. Then, we present oscillations of the magnetization probed by vibrating sample and cantilever-based torque magnetometry. Previously undetected oscillation frequencies are then linked to FS pockets centered around the Γ-point of CoSi.

4.3.1 Quantum oscillation spectra

The second sample we investigated was synthesized via flux growth and exhibits a residual resistivity ratio of 25. This sample was contacted in a conventional 6-point configuration. Its magnetotransport properties are similar to the first sample with additional features in the SdH spectra. In the analysis presented here, we focus on the Hall resistivity, due to its larger oscillation amplitudes and correspondingly better signal-to-noise ratio.

Figure 4.8 (a) shows the Hall resistivity, ρ_{xy}, as a function of the applied magnetic field B in the temperature range up to 700 mK. In comparison to the first sample investigated the absolute Hall resistivity is slightly larger and the SdH oscillations are approximately twice as strong. The oscillatory part of ρ_{xy}, shown in Fig. 4.8 (b), displays a more complex structure, indicating that there are additional contributions to the signal. The Fourier spectrum is shown in Fig. 4.8 (c). The strongest oscillations are again detected at f_α and f_β, but in this sample higher harmonics of these frequencies up to the ninth order are visible in the spectrum. Additionally, there are further peaks at low frequencies. A zoom-in view of the low frequency region is shown in Fig. 4.8 (d). The large peak towards zero frequency varies with the background subtraction and is therefore excluded from the analysis. A peak at $f_{\beta-\alpha}$ at approximately 100 T is identified as the difference between f_α and f_β. Furthermore, two additional frequencies, f_ϵ and f_ϕ, are detected.

The temperature dependence of all fundamental frequencies is shown in Fig. 4.8 (e). Their temperature dependent damping is analyzed by fitting the amplitudes with the LK temperature reduction factor R_T. The results of the fits are indicated by solid lines. The extracted cyclotron masses of the two dominant frequencies are $m^*_\alpha = (0.92 \pm 0.01)\, m_e$ and $m^*_\beta = (0.99 \pm 0.01)\, m_e$, consistent with the values obtained from our other sample and the literature [138–141]. The additional frequencies f_ϵ and f_ϕ exhibit a stronger temperature dependent damping yielding cyclotron masses of $m^*_\epsilon = (2.5 \pm 0.1)\, m_e$ and $m^*_\phi = (3.1 \pm 0.1)\, m_e$. $f_{\beta-\alpha}$ exhibits only a slight decrease in amplitude in this temperature range consistent with the LT behavior shown in Fig. 5.5 (c).

Next, we turn to the angular dependence of the oscillation frequencies. FFT spectra recorded at different angles θ of the applied magnetic field are shown in Figure 4.9 (a). Because we use the Hall signal, ρ_{xy}, in this analysis, we compensate for the reduction of oscillation amplitudes upon rotation of the sample away from the ideal Hall

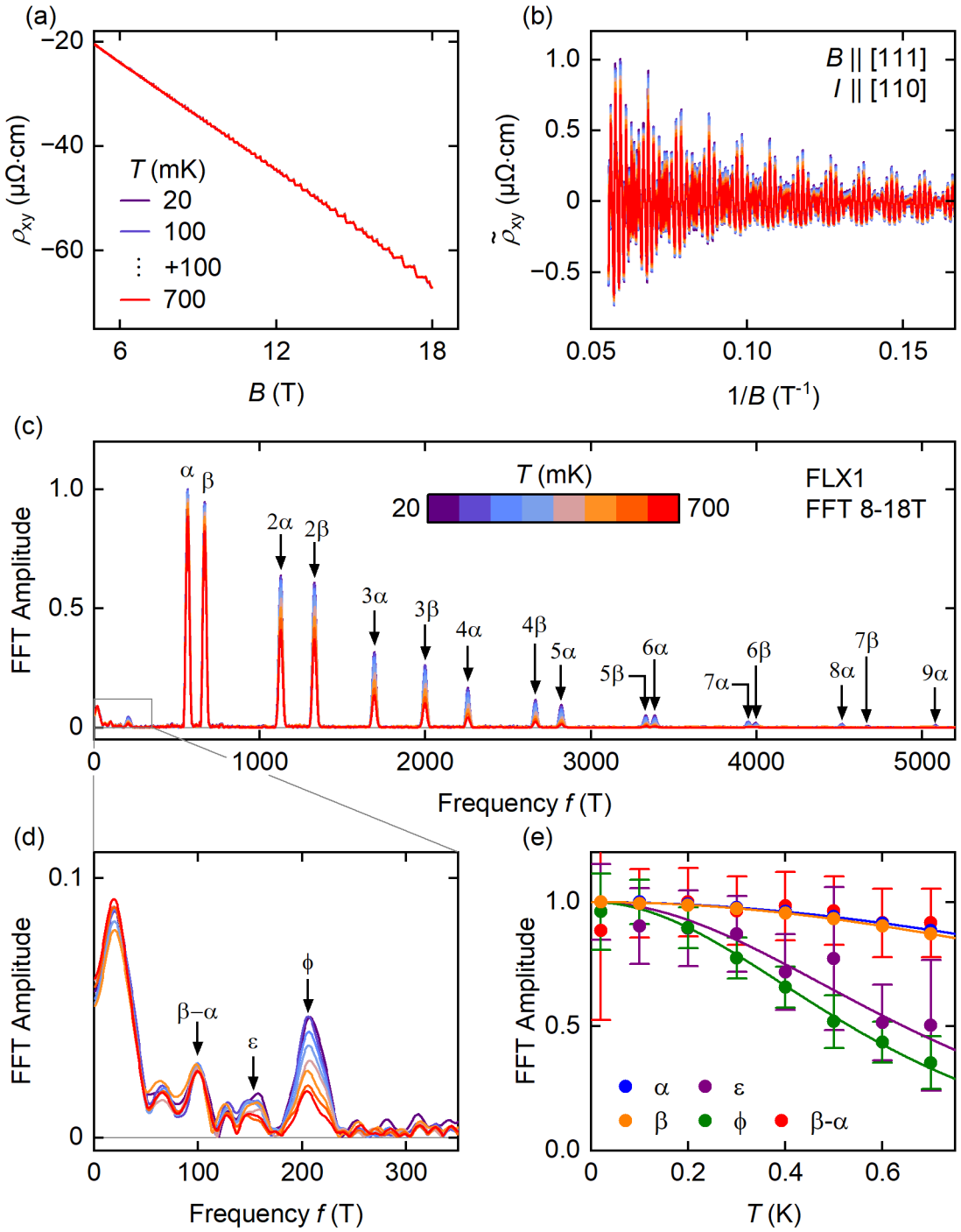

Figure 4.8: Temperature dependence of SdH oscillations in sample FLX1. (a) Hall resistivity, ρ_{xy}, as a function of the applied magnetic field B. (b) Oscillatory part of the Hall resistivity, $\tilde{\rho}_{xy}$, as a function of $1/B$. (c) Fourier spectra of the data shown in (b). Harmonics of the frequencies α and β up to the ninth and seventh order, respectively, can be identified. (d) Close-up view of the low frequency region. Additional peaks labeled δ, ϵ and ϕ are detected. (e) Fourier amplitude as a function of temperature T. The lines represent fits of the LK temperature reduction factor R_T yielding effective masses of $m^*_\alpha = (0.92 \pm 0.01)\, m_e$, $m^*_\beta = (0.99 \pm 0.01)\, m_e$, $m^*_\epsilon = (2.5 \pm 0.1)\, m_e$, and $m^*_\phi = (3.1 \pm 0.1)\, m_e$. The difference frequency amplitude exhibits a slight decrease in amplitude for increasing temperatures consistent with the LT behavior shown in Fig. 5.5 (c).

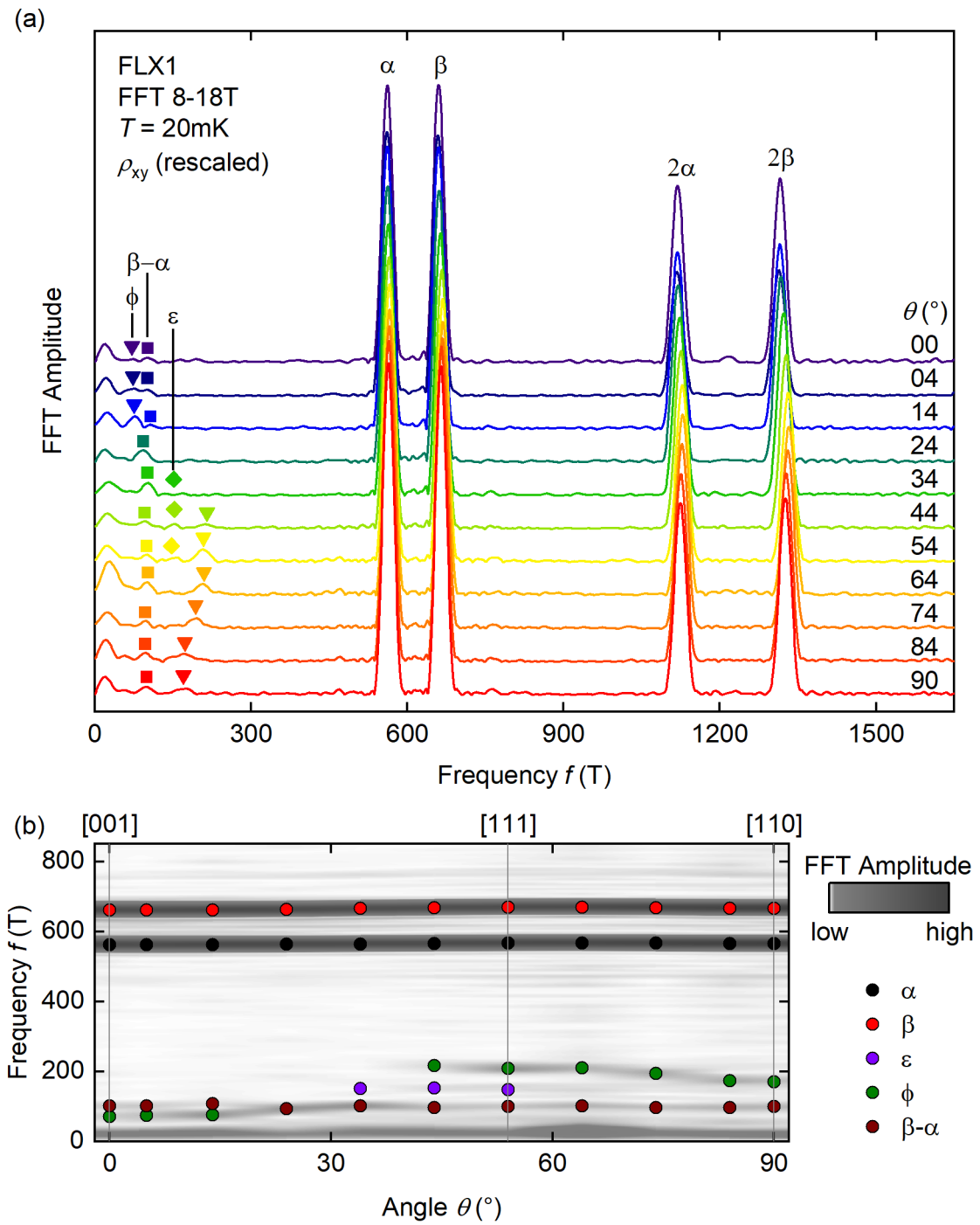

Figure 4.9: Angular dependence of SdH oscillations in sample FLX1. (a) Fourier spectra of the oscillations in ρ_{xy} recorded at different angles θ of the applied magnetic field. The signal has been scaled with a cosine factor to account for the reduced transversal voltage pickup when rotating the field away from the [111] direction. Curves are offset for clarity. In addition to frequency branches α and β, three further branches ϕ, $\beta - \alpha$ and ϵ can be identified. The peak positions at each angle are marked by solid symbols. (b) Fourier amplitudes as a function of angle and frequency shown as a colormap. The extracted frequencies at each angle are shown as colored dots with the colors representing different frequency branches.

geometry by rescaling them. In order to follow the frequency branches more easily, a colormap of the FFT amplitudes as a function of frequency f and angle θ is shown in Fig. 4.9 (b). At each angle, at which a measurement has been performed, the peaks are analyzed individually by fitting them with Gaussians and the determined frequencies are marked by colored points.

Frequency contributions α, β, and $\beta - \alpha$ are detected over the whole angular range and show almost no dispersion. Frequency branch ϵ is only detected in a narrow angular range around the [111] direction. There are two further branches, which can be followed over a finite angular range. They both originate from a continuously evolving FS orbit around the Γ-point, as discussed in Sec. 4.3.2, and are therefore identified as belonging to the same frequency branch ϕ. At angles $\theta < 20°$ the frequency of this branch rises slightly with increasing angle. For angles between 20° and 40° it cannot be followed conclusively. At angles above 40° it reemerges at a frequency of about 210 T, decreases slightly with increasing angle and can be followed up to $\theta = 90°$. There might be additional contributions at frequencies below 50 T. However, because for these sets of measurements the FFT amplitudes at low frequencies vary strongly with the parameters of the data analysis, possible oscillations in the low frequency range cannot be determined reliably.

Next, we report on the oscillations in the magnetization of CoSi. We probed the magnetization at our laboratory in two different setups using vibrating sample magnetometry. The small size of our samples rendered it a challenge to obtain a clean signal above the noise level. The data shown here was recorded with the largest sample HKZ7 S2, for which the best signal-to-noise ratio was achieved. The two different setups utilized cover a similar temperature range but differ in the maximum available field and minimal detectable magnetic moment. In comparison to the setup using conventional detection coils the SQUID magnetometer has a sensitivity about an order of magnitude higher. The maximum applicable field, however, is only half of what can be used in the conventional setup, making the overall signal and especially the superposed quantum oscillations considerably smaller. Here, we show data recorded in both setups and discuss their similarities and differences.

First, we show the data recorded in the setup using conventional detection coils in Figure 4.10. The magnetization as a function of applied magnetic field along the [001] crystallographic orientation at selected temperatures between 2 K and 9 K is shown in Fig. 4.10 (a). The paramagnetic response exhibits an almost linear dependence on B

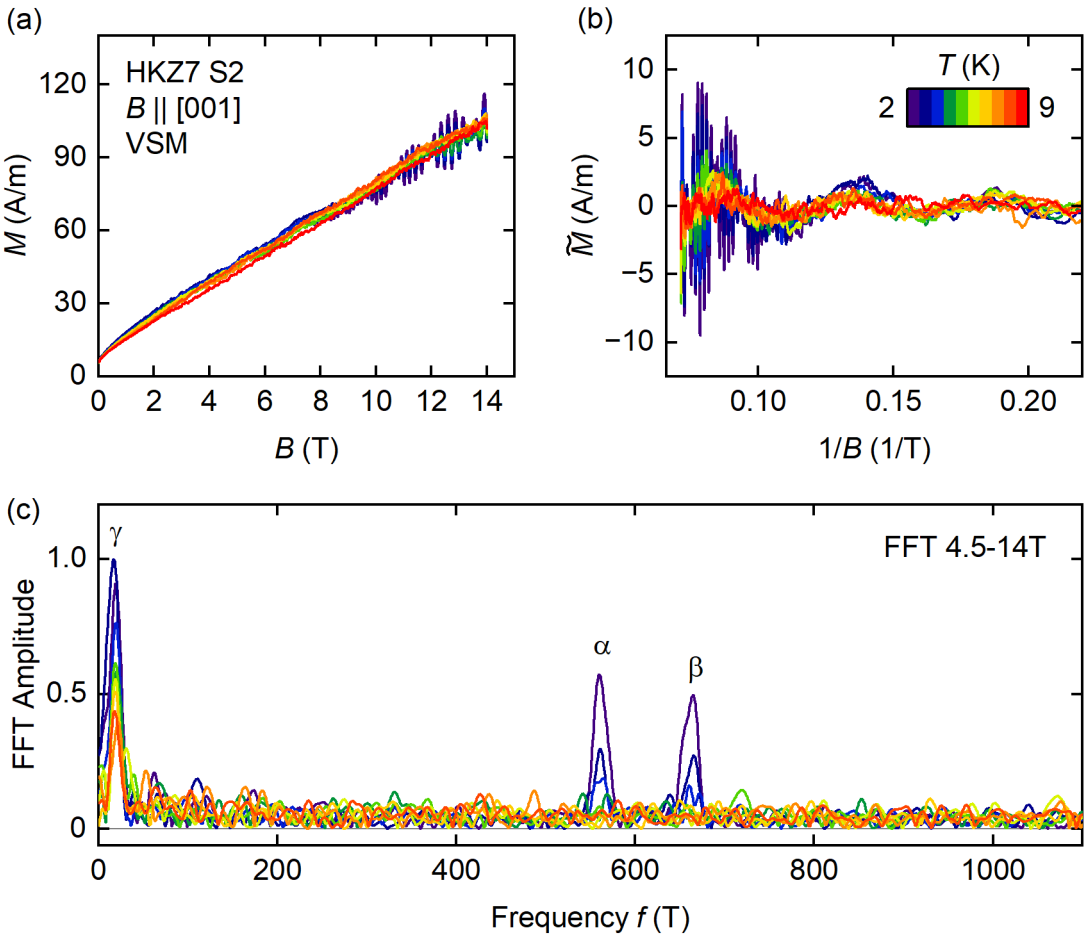

Figure 4.10: Vibrating sample magnetometry. (a) Magnetization, M, as a function of the magnetic field, B, applied along the [001] direction recorded at different fixed temperatures between 2 K and 9 K. (b) Oscillatory part of the data shown in (a) as a function of the inverse applied field. In addition to the fast oscillations present at the lowest temperatures a slow oscillation component is visible. (c) Normalized FFT spectra of the data shown in (b). The slow oscillations correspond to the peak at $f_\gamma \approx 20\,\mathrm{T}$.

superposed by characteristic de Haas-van Alphen oscillations at large magnetic fields. In the temperature range up to 9 K the non-oscillatory part of the signal decreases only slightly with increasing temperature. The oscillatory part of the magnetization, after subtraction of a smooth background, as a function of inverse field is shown in Fig. 4.10 (b). Slow oscillations may be discerned for fields above 5 T (below $0.2\,\mathrm{T}^{-1}$) and are only weakly dampened by temperature. Fast oscillations are only visible at the lowest temperatures and for fields larger than 8 T (smaller than $0.125\,\mathrm{T}^{-1}$). The Fourier spectrum evaluated in a field range between 4.5 T and 14 T is shown in Fig. 4.10 (c). The fast oscillations correspond to frequency contributions $f_\alpha \approx 560\,\mathrm{T}$ and $f_\beta \approx 664\,\mathrm{T}$ and are consistent with the frequencies detected in the SdH effect.

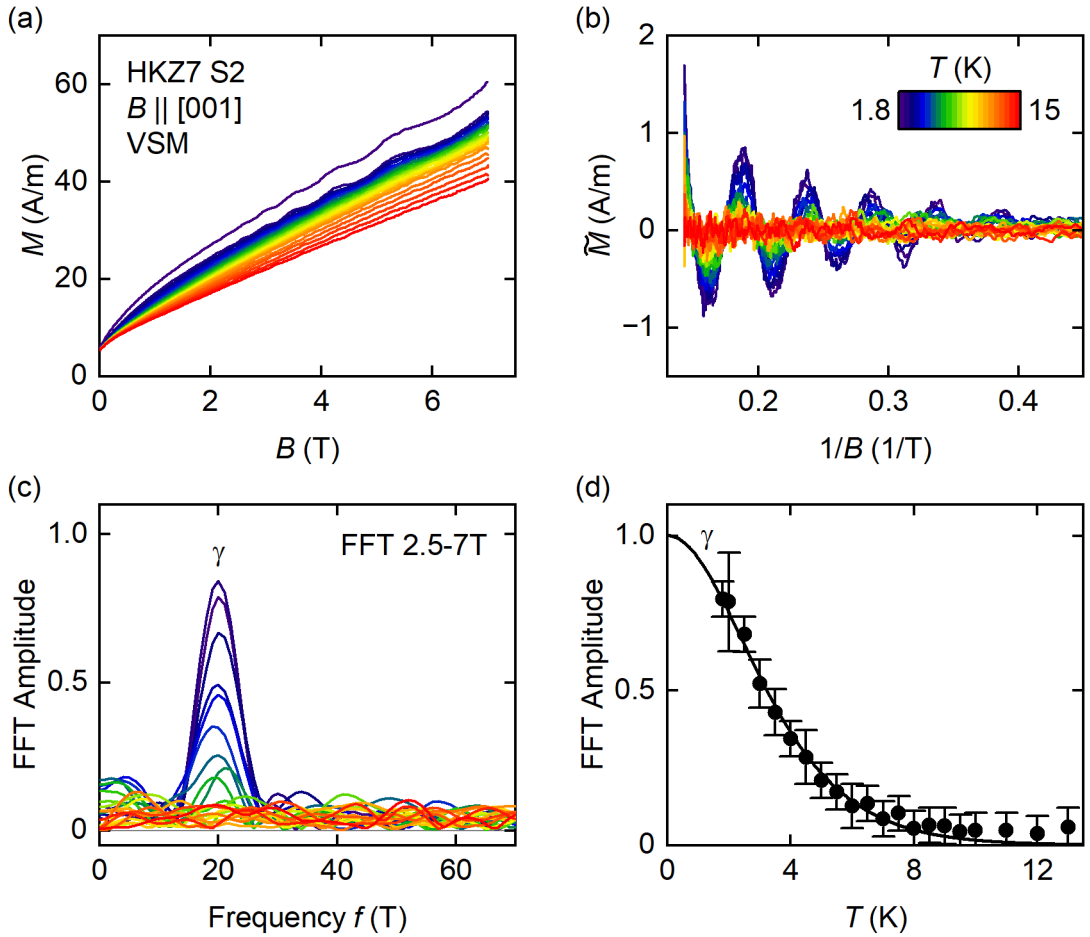

Figure 4.11: SQUID vibrating sample magnetometry. (a) Magnetization, M, as a function of the applied magnetic field, B, detected with a SQUID magnetometer at selected temperatures. (b) Oscillatory part of the signal as a function of inverse applied field. Up to the highest field of 7 T available only slow oscillations are visible. (c) FFT spectra of the data shown in (b). The only detected contribution corresponds to the frequency f_γ at (20 ± 1) T. (d) FFT amplitude of the γ peak as a function of temperature. A LK R_T fit is indicated by the solid line and yields an effective mass of $m_\gamma = (0.17 \pm 0.01)\, m_e$.

The peak at $f_\gamma \approx 20$ T corresponds to the slow oscillations and was not resolved in our SdH experiments. Its weak damping with increasing temperature is visible in the slow decrease of its Fourier amplitude. For temperatures above 9 K the data recorded in the conventional setup was too noisy to identify clear features in the FFT spectra and is thus not shown here.

To further analyze the temperature dependence of the frequency contribution f_γ we performed additional experiments on the same sample in a setup using a SQUID magnetometer which has a better signal-to-noise ratio but a lower maximal applicable field of 7 T. The magnetization as a function of the applied field at selected

temperatures between 1.8 K and 15 K is shown in Figure 4.11 (a). The data agrees well with the measurements shown in Fig. 4.10 but exhibits a much lower noise level. A clear tendency of the non-oscillatory paramagnetic contribution to the signal weakening with increasing temperature can be seen and is consistent with the magnetic properties shown in Fig. 4.1. The oscillatory part of the magnetization, shown in Fig. 4.11 (b), exhibits slow oscillations discernible for magnetic fields above 2.5 T (below $0.4\,\mathrm{T}^{-1}$), which can be resolved more clearly thanks to the improved sensitivity of the SQUID magnetometer. No fast oscillations are visible in the field range up to 7 T. Consequently, the only frequency contribution visible in the FFT spectra shown in Fig. 4.11 (c) corresponds to the slow oscillations with a frequency of $f_\gamma \approx 20\,\mathrm{T}$. The amplitudes of the FFT peaks as a function of temperature are shown in Figure 4.11 (d). They follow the behavior expected from the LK temperature reduction factor $\mathrm{R_T}$ involving an effective mass of $m_\gamma = (0.17 \pm 0.01)\, m_e$, as indicated by the solid line. The origin of the frequency contribution f_γ is a small Fermi surface pocket centered around the Γ-point of CoSi and is further explained in Section 4.3.2.

Next, we present data recorded at the high-field magnetic laboratory LNCMI in Grenoble, France. We used cantilever-based torque magnetometry with a capacitive readout to probe the dHvA effect in sample FLX1 in magnetic fields up to 31.4 T and at dilution refrigerator temperatures.

Figure 4.12 shows a typical dataset obtained at a temperature of $T < 50\,\mathrm{mK}$ and a specific angle of the applied magnetic field. The capacitance change ΔC is directly proportional to the perpendicular magnetic moment of the sample with respect to the applied field and can therefore be used as a probe for the dHvA effect. Fig. 4.12 (b) depicts the oscillatory component of the capacitance as a function of inverse applied field after subtraction of a polynomial background. The corresponding frequency spectrum is shown in Fig. 4.12 (c). As in the measurements presented above, frequency components f_α and f_β are detected, albeit with less harmonic frequencies resolved as compared to our SdH study on the same sample. The peak at f_ϕ matches well with the corresponding frequency component in our SdH spectra, exhibiting a larger normalized amplitude in the high-field torque magnetometry data. The difference in amplitudes is attributed to the different measurement techniques and field ranges used in the experiments.

We recorded torque magnetometry data in the angular range between $\theta = 4°$ and 84° measured from the [001] crystallographic direction in a $(1\bar{1}0)$ rotation plane. The

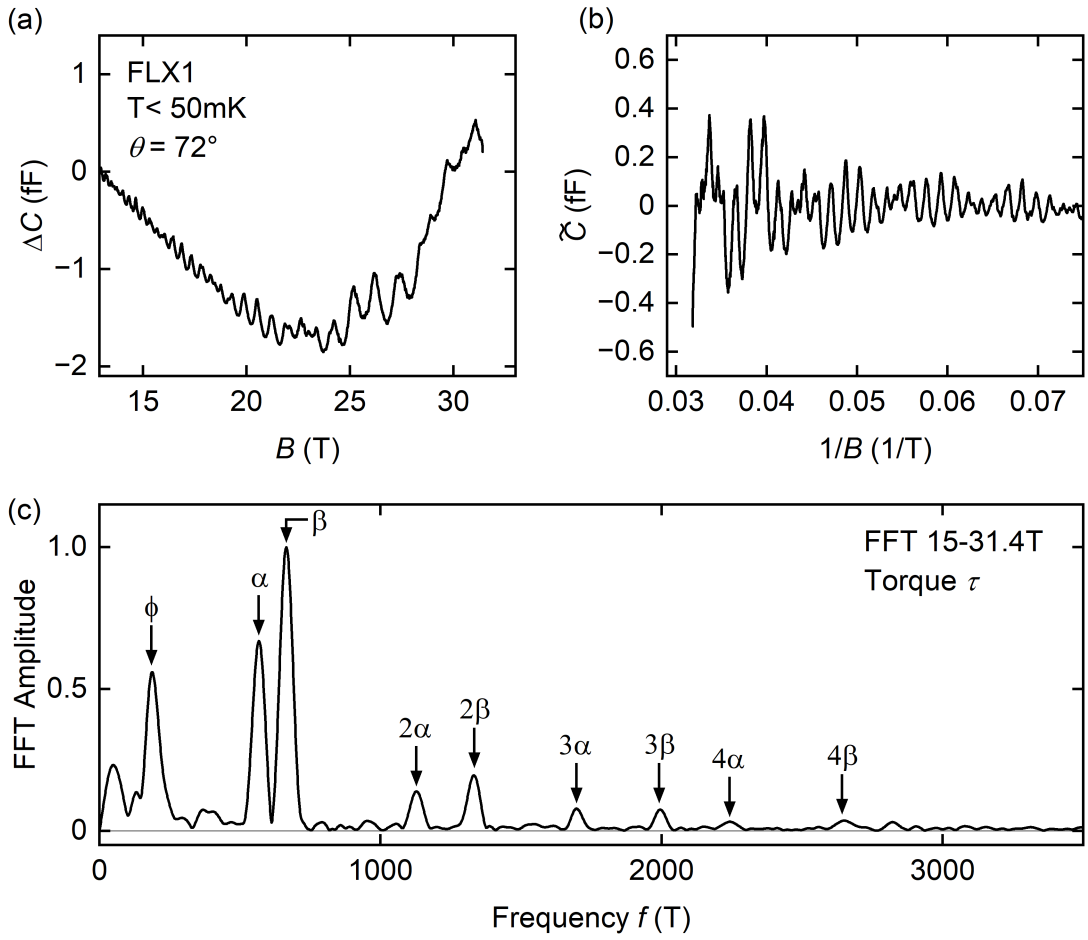

Figure 4.12: High-field torque magnetometry. (a) Capacitance change, ΔC, of the magnetometer as a function of the applied magnetic field, B, for an exemplary dataset recorded at $\theta = 72°$. The change in capacitance is proportional to the magnetic torque, τ, created by the sample and therefore a measure for the perpendicular component of its magnetization $M_\perp$. (b) Oscillatory part of the capacitance after subtraction of a smooth background. (c) FFT spectrum of the data shown in (b) analyzed in the filed range between 15 T and 31.4 T. Frequencies f_α, f_β, their higher harmonics, and f_ϕ can be identified.

resulting frequency spectra are shown in Figure 4.13. Frequencies f_α and f_β are observed over the whole angular range. The signal strength for all oscillation frequencies weakens close to the high-symmetry directions due to the torque factor described in Eq. (2.26). f_ϕ is discernible for angles above $\theta = 40°$ with an increasing amplitude towards larger angles. While this frequency branch might evolve towards lower frequencies for lower angles, it is not possible to clearly separate it from artifacts arising from an imperfect background subtraction for angles $\theta < 40°$. An additional weaker frequency contribution labeled f_η is detected in the frequency range between 700 T and 800 T in two datasets recorded at $\theta = 20°$ and 24°.

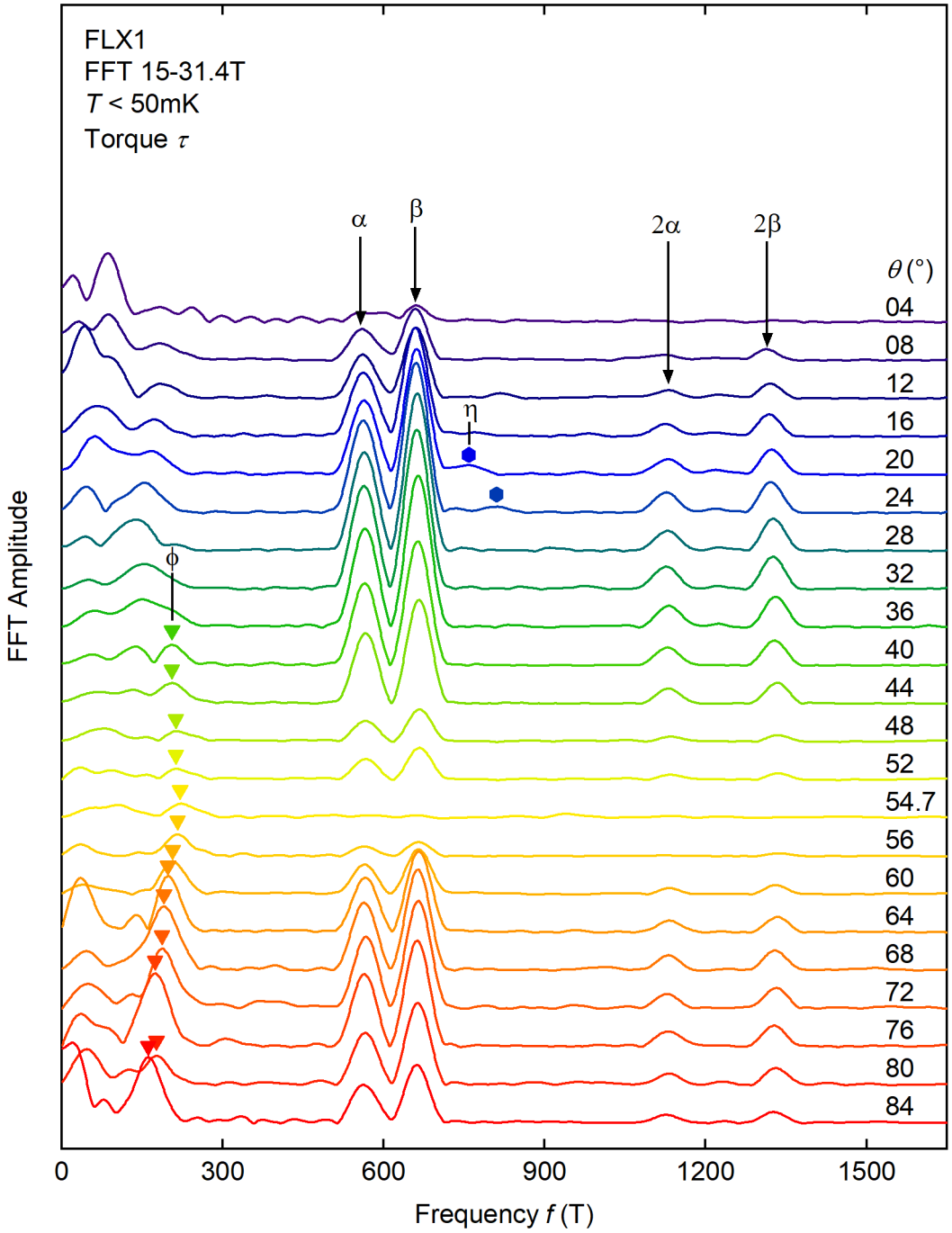

Figure 4.13: Angular dependence of the high-field torque magnetometry data. FFT spectra obtained from the high-field torque magnetometry measurements recorded at different angles of the applied magnetic field. Curves are offset for clarity. The FFT amplitudes vary with the angle of the applied magnetic field and vanish for high-symmetry directions. Several frequency branches can be identified. α and β as well as its higher harmonics show almost no angular dispersion. Frequency branch ϕ can be followed over the angular range between $\theta = 40°$ and 84°. A further weak frequency contribution η is identified in the spectra recorded at $\theta = 20°$ and 24°. A more detailed investigation of this angular range is shown in Fig. 4.14.

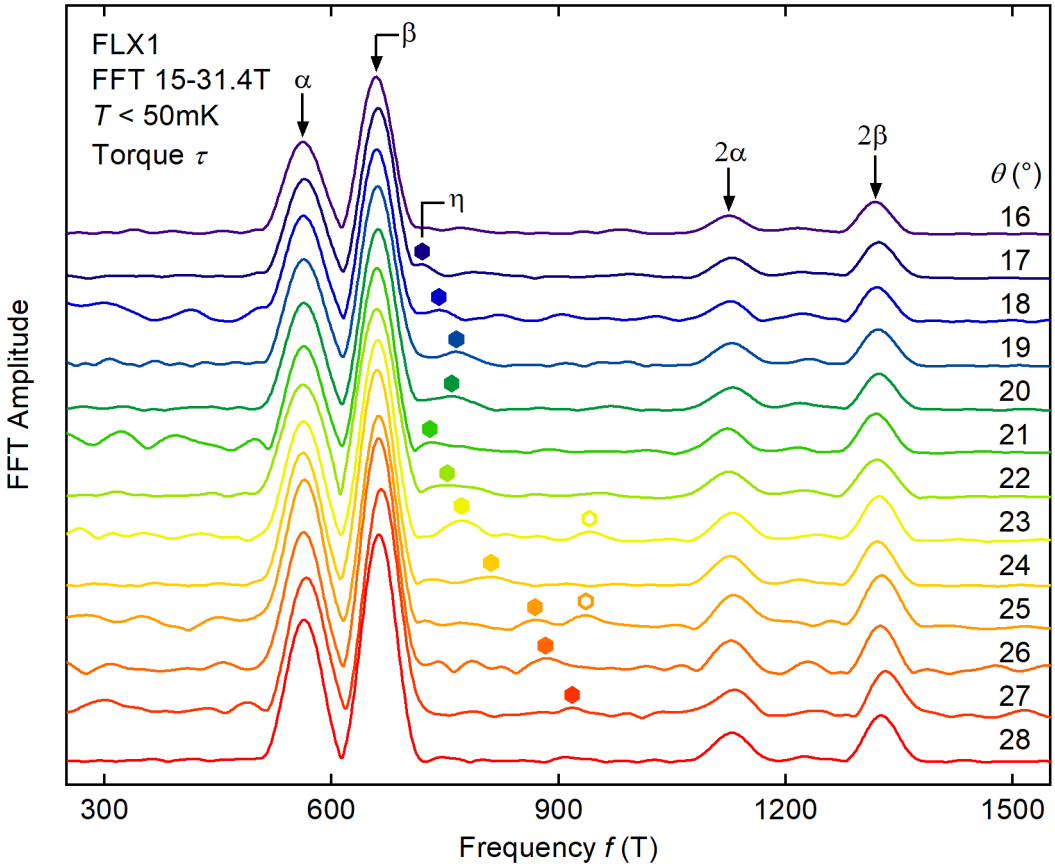

Figure 4.14: Angular dependence of the η-branch in the high-field torque magnetometry data. FFT spectra in the angular range between $\theta = 16°$ and 28°. Apart from the dominant frequency branches α and β and their higher harmonics, the frequency branch η can be followed over most of the angular range shown here. Clearly identifiable peaks are marked with solid symbols. Open symbols indicate additional frequency contributions detected at $\theta = 23°$ and 25°, which are consistent with a splitting of the η-branch, but cannot be traced conclusively.

To further investigate the frequency contribution f_η, we performed additional measurements in small angular steps in the region between $\theta = 16°$ and 28°. The corresponding oscillation spectra are depicted in Figure 4.14. The η-peak can be traced over most of this angular range and is marked by solid symbols. We followed the criteria described in Sec. 3.4 in order to differentiate this weak frequency contribution from random noise on the data. Additionally, there are further peaks in this frequency range in the spectra recorded at $\theta = 23°$ and 25° marked by open symbols. They are consistent with a splitting of the η-branch, but cannot be traced conclusively and are therefore not considered further in the analysis.

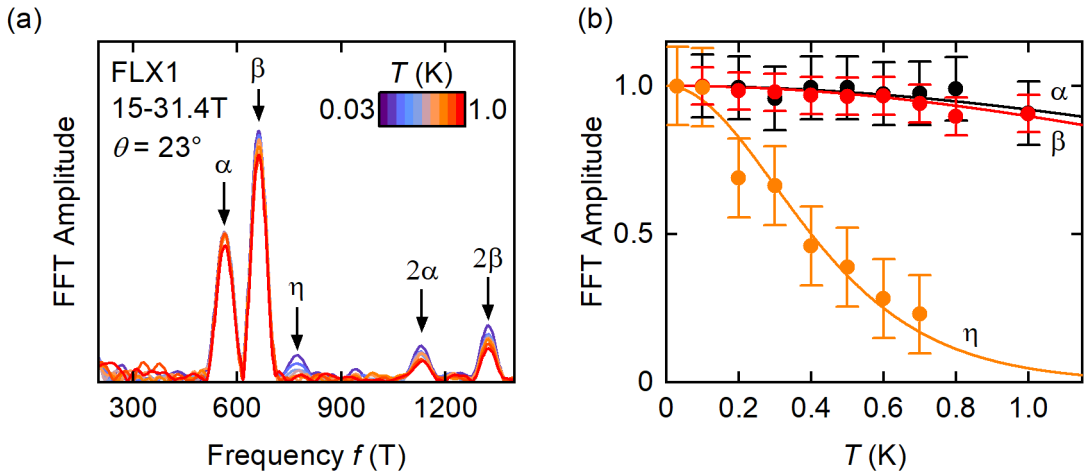

Figure 4.15: Temperature dependence of the high-field torque magnetometry data. (a) FFT spectra of the dHvA oscillations recorded at $\theta = 23°$ and different selected temperatures. Frequencies α and β as well as their higher harmonics and the frequency η exhibit clear peaks. Contributions below 300 T cannot be clearly identified and are therefore excluded from the analysis. (b) FFT amplitudes of the detected frequencies as a function of temperature T. The solid lines indicate fits with the LK temperature reduction factor R_T yielding effective masses of $m_\alpha = (1.0 \pm 0.1)\, m_e$, $m_\beta = (1.1 \pm 0.1)\, m_e$, and $m_\eta = (7.5 \pm 0.4)\, m_e$.

We performed temperature dependent measurements at $\theta = 23°$, at which the η peak exhibits the largest amplitude. The FFT spectra recorded in the temperature range between 30 mK and 1 K are shown in Figure 4.15 (a). The FFT amplitudes as a function of temperature are shown in Fig. 4.15 (b). In the field range analyzed the frequency contributions f_α and f_β show only a small reduction in amplitude below 1 K. The solid lines indicate fits of the LK temperature reduction factor R_T yielding cyclotron masses close to 1 m_e, consistent with results from our other experiments and the literature [138–141]. We note that, due to the small damping of these frequency contributions in the temperature range investigated, the determination of cyclotron masses from these experiments is less accurate as compared to our studies at lower fields. In contrast, the frequency contribution f_η is damped strongly with increasing temperature and only detectable up to 0.7 K. A fit with the LK reduction factor yields a cyclotron mass of $(7.5 \pm 0.4)\, m_e$.

4.3.2 Fermi surface trajectories

In this section, we match the experimentally observed frequencies to extremal trajectories on the FS of CoSi. As explained in Sec. 4.2.2, the quantum oscillation spectra arising from the FS around the R-point unambiguously show a spin-orbit coupling induced splitting of the bands. All calculations presented here consequently are

performed on the relativistic band structure depicted in Figure 2.4 (b)-(d). We begin with a comparison to the predicted quantum oscillation frequencies from the DFT band structure as calculated. We then show that the application of small rigid band shifts, while conserving overall charge neutrality, leads to an improved match between experiment and theory, implying that an empirical correction to the calculated band structure is needed to accurately describe the Fermi surface geometry in CoSi.

Figure 4.16 (a) depicts the predicted frequency branches as calculated from DFT overlayed by the experimentally determined quantum oscillation frequencies extracted from the experiments presented in Sec. 4.3.1. The width of the lines represents the predicted QO amplitudes. A description of which amplitude factors have been considered can be found in Sec. 2.3. The corresponding FS pockets around the Γ- and R-point are shown in Fig. 4.16 (b) and (c), respectively.

Small shifts of the bands with respect to the Fermi level have been employed to yield a better match between experiment and theory. This approach may be used to partially correct inaccuracies in the calculated band structure arising, e.g., from correlations, which are not fully captured by DFT. The predicted frequency spectrum after shifting the bands overlayed by the experimentally detected frequencies is shown in Fig. 4.16 (d). The corresponding FS is depicted in Fig. 4.16 (e) and (f).

We begin with the assignment of frequency branches α and β and their second harmonics. As explained in detail in Sec. 4.2.2, there are two almost dispersionless frequency branches expected from the intersecting Fermi surface pockets centered around the R-point. With the Fermi energy as calculated by DFT, the frequencies are expected to be 720 T and 820 T for the fundamentals and 1440 T and 1640 T for the second harmonics, as indicated by the gray lines in Fig. 4.16 (a). This implies that the calculated FS pockets are larger than in reality. An upward shift of the bands around the R-point by 30 meV reduces the size of these pockets while leaving their shape almost invariant. The frequency branches predicted from the corrected Fermi surface shown in Fig. 4.16 (d) match the experimentally detected frequencies very well.

We note that the band shift reduces the occupied BZ volume of the electron-like pockets at the R-point from 2 % as calculated to ≈1.5 %. In order to conserve overall charge neutrality, the predominantly hole-like bands around the Γ-point have to be

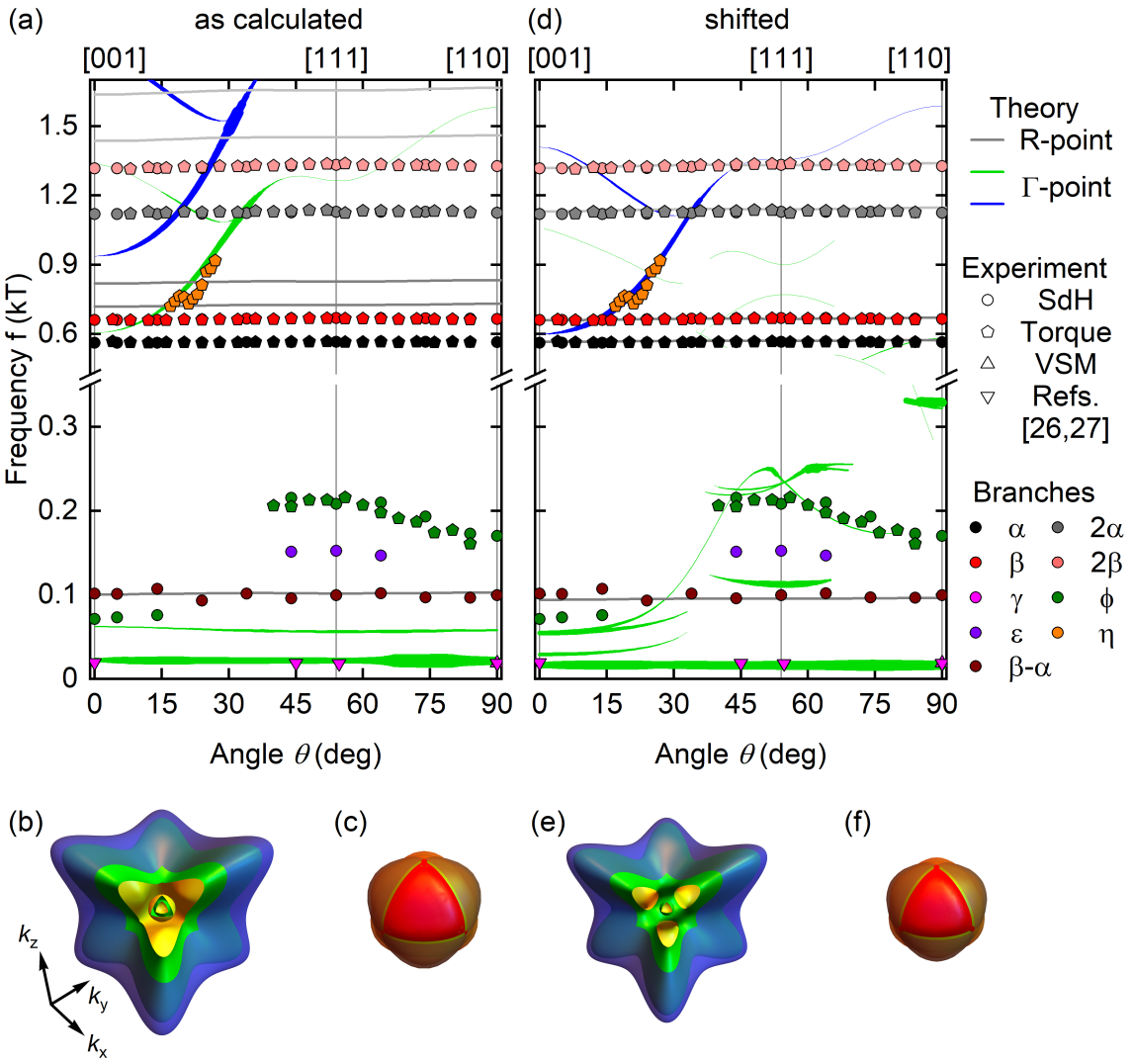

Figure 4.16: Comparison between calculated and experimentally detected frequencies. (a) Experimentally detected (solid symbols) and predicted (colored lines) frequency branches. Symbol shapes indicate the technique used. Symbol colors represent an assignment to a distinct frequency branch. VSM data on frequency branch γ at different angles are included from Refs. [141, 142]. Predicted frequencies from the FS around the R-point, explained in detail in Section 4.2.2, are indicated by gray lines. Predicted frequencies arising from the FS around the Γ-point are marked by colored lines, where the band color represents the band index. The linewidth represents the expected oscillation amplitude (see Sec. 2.3 for details). (b) Close-up view of the Fermi surface around the Γ-point as calculated from the DFT. Part of the FS sheets has been cut out and the outermost sheet is drawn semi-transparent to allow for a view of the inner pockets. (c) Fermi surface around the R-point as calculated. (d) Frequency branches as in (a) after applying small rigid band shifts. The frequency branches closely match the experimental observations. (e), (f) Fermi surface around the Γ- and R-point after applying the band shifts. All pockets shrink in size and the inner pockets around the Γ-point significantly change their shape giving rise to distinct differences in the predicted QO spectra.

shifted downwards. Considering the larger density of states due to the higher band masses, a shift on the order of 7 meV is expected for the bands around the Γ-point.

The difference frequency branch $\beta - \alpha$, detected in our SdH study, can be explained by oscillations of the quasiparticle lifetime. This frequency branch is analyzed in detail in Chapter 5 and arises due to a coupling between the extremal trajectories giving rise to frequencies α and β. Because the difference frequency is not related to a distinct extremal cross section on the FS via the Onsager relation, it does not reveal new information about the FS geometry and we therefore focus on the conventional quantum oscillation frequencies in the following. It is, however, interesting to note that the frequency $f_{\beta-\alpha}$ depends only weakly on the the chemical potential and therefore remains at ≈100 T after applying the band shift to the band structure around the R-point.

Next, we discuss the branches γ, ϕ, ϵ, and η, which arise from the FS sheets centered around the Γ-point. We start with a description of the FS from the DFT band structure as calculated followed by a comparison with the FS after small band shifts have been applied. All experimentally detected frequencies are then assigned to the adapted FS based on their frequency, angular dispersion, detectable angular range, and cyclotron masses.

The FS around the Γ-point arising from the band structure as calculated by DFT is depicted in Fig. 4.16 (b). It comprises multiple nested pockets arising from two bands. Band 3 (shown in green) gives rise to multiple FS pockets. The innermost pocket has hole-like character and would be expected to give rise to an almost dispersionless frequency branch at ≈22 T. It is surrounded by an electron-like FS sheet that would give rise to a frequency branch at ≈60 T. The same band crosses the Fermi level again further away from the Γ-point resulting in a cuboid-shaped FS sheet with elongations along the Γ-R lines. For B close to [001] there are one minimal and two degenerate maximal cross sections on this FS sheet, which would be expected to give rise to two oscillation frequencies at 0.6 kT and 1.3 kT, respectively. Upon field rotation, the extremal trajectories merge resulting in a single expected oscillation frequency for angles larger than 35°. The second band that crosses the Fermi level in the vicinity of the Γ-point is band 4 (shown in blue). It gives rise to a single hole-like FS pocket, which resembles the outermost pocket of band 3, but is slightly larger. Consequently, the expected frequency branches follow the same angular dispersion, albeit at slightly larger frequencies.

While the lowest experimentally detected frequency branch γ agrees well with the dispersionless branch expected from the innermost hole pocket, no signs of the surrounding electron pocket at ≈60 T, that should be easily detected in experiment, have been observed. Additionally, the experimentally detected frequency branches ϕ and ϵ cannot be explained by the FS from the DFT results as calculated, implying that an empirical correction is needed.

The experimental observations can be described consistently if the bands around the Γ-point are shifted downwards by 4 meV for band 3 and by 7 meV for band 4. Taken together with the band shifts applied to the R-point, overall charge neutrality is approximately conserved. The resulting FS is shown in Fig. 4.16 (e). As a result of the small shifts the innermost pocket shrinks in size but maintains its almost spherical shape. The intermediate electron pocket arising from band 3 merges with the outer hole-like pocket, which together form a single cuboid-shaped FS sheet with apertures along the Γ-X directions. The outermost FS sheet arising from band 4 shrinks in size but keeps its overall shape. Frequency branches γ, ϕ, ϵ, and η can now be assigned to the adapted FS geometry.

To better illustrate which extremal trajectories give rise to which frequency branches, we show the FS pockets arising from the shifted bands together with extremal trajectories perpendicular to the [001] and [111] direction in Figure 4.17. Panels (a) and (b) depict the Fermi surface sheets arising from band 3. The dispersionless frequency branch γ is attributed to the innermost spherical pocket. The absence of this frequency branch in our torque magnetometry study is attributed to its almost perfect isotropy. Its absence in our SdH data indicates that this part of the Fermi surface contributes only little to the resistivity.

Frequency branch ϕ matches well with extremal orbits through the apertures of the cuboid-shaped FS pocket. For magnetic fields close to the [001] direction they result in a frequency of ≈70 T matching well with low frequencies detected in our SdH data below $\theta = 15°$. Upon field rotation these trajectories pass over the elongations of the cuboid with a maximum for the extremal cross section for magnetic field applied close to [111]. In the strongly dispersive angular region up to $\theta = 40°$ the ϕ-branch was not resolved in experiment. For larger angles the enclosed extremal area is predicted to reduce towards the [110] direction, which is in good agreement with the behavior of the experimentally detected dispersion.

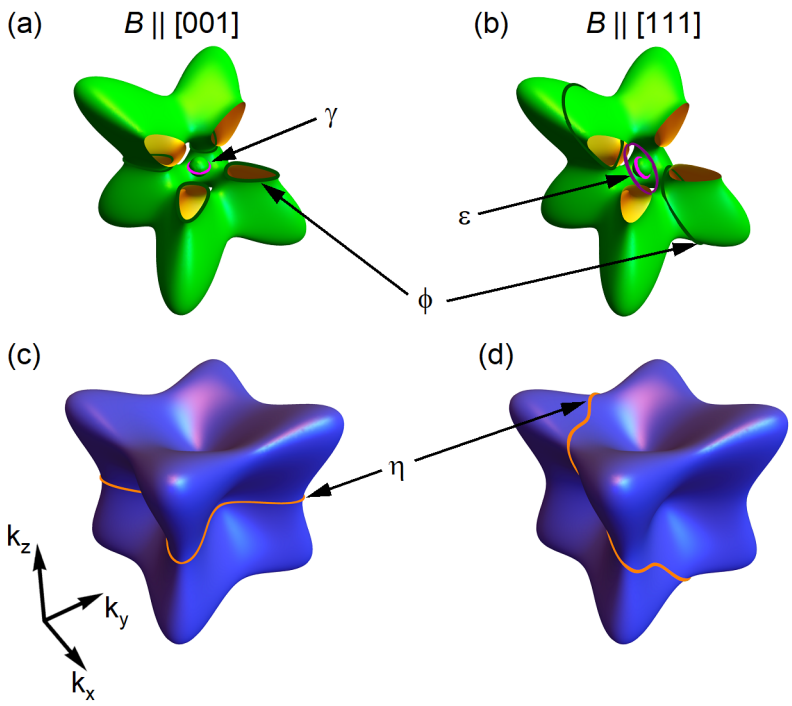

Figure 4.17: Extremal trajectories on the Fermi surface around the Γ-point. (a), (b) Fermi surface of band 3 shifted downwards by 4 meV. To enhance visibility, part of the outer pocket has been excluded. The γ branch is attributed to the small hole-like sphere located at the center. The ϕ orbits traverse through the apertures of the outer pocket. The ϵ orbit travels along the inner surface of the same pocket and only exists in a limited angular range perpendicular to the [111] direction. (c), (d) FS originating from band 4 shifted downwards by 7 meV. The η branch is associated with the extremal orbit exhibiting a minimal cross section.

A further extremal trajectory running along the inside of this FS sheet is expected for magnetic fields close to the [111] direction. For other field directions this orbit does not exist because of the apertures along the Γ-X directions. The experimentally detected frequency branch ϵ in our SdH spectra matches well with this behavior. The slightly higher frequency observed in experiment indicates a real FS trajectory that is slightly larger than shown in Fig. 4.17 (b).

In the angular region in which it is observed, the η-branch matches well with the minimal orbit expected from the FS arising from band 4 shifted down by 7 meV. The corresponding Fermi surface trajectories are depicted in Fig. 4.17 (c) and (d). The experimental observation of this frequency branch over only a narrow angular range can be explained by a combination of different factors. It is the heaviest orbit observed experimentally, reducing the amplitudes of quantum oscillations in terms of both cyclotron energy and the temperature reduction factor R_T. Additionally, since

Frequency branch	m_{exp} (m_e)	m_{calc} (m_e)	Field angle θ (°)
γ	0.17 ± 0.01	0.13	90 [110]
ϵ	2.5 ± 0.1	2.6	54.7 [111]
ϕ	3.1 ± 0.1	4.3	54.7 [111]
η	7.5 ± 0.4	7.2	23

Table 4.1: Cyclotron masses. Experimentally determined and calculated cyclotron masses at angles for which temperature dependent measurements have been performed.

the orbit is only detected in our high-field torque magnetometry experiments, the torque reduction factor given in Eq. (2.33) is expected to give rise to the largest oscillations amplitudes in the strongly dispersive frequency region, in which the η-branch is actually observed. Towards larger angles the increasing size of this orbit reduces its expected amplitude again through the Dingle damping factor $\mathrm{R_D}$.

Apart from the oscillation frequencies and angular dispersion, the cyclotron mass is an important indicator for matching experimental frequency branches to predictions from DFT. A comparison between the experimentally determined and calculated cyclotron masses for selected field orientations is shown in Table 4.1. The cyclotron masses of γ, ϵ, and η match very well between experiment and theory. The experimentally observed cyclotron mass of ϕ is $\approx$25 % smaller than predicted. We note that in the calculations the cyclotron mass of this frequency branch close to the [111] direction is highly sensitive to the exact angle and band shape. Therefore, the small deviation to the experimentally observed value is considered to arise from limitations in the accuracy of our calculations. The good match between the observed and predicted cyclotron masses further validates the assignment of the frequency branches presented above.

Additional frequency branches are expected from the complex Fermi surface geometry of the outer pocket shown in Fig. 4.17 (a) and (b). They are expected to exhibit a low amplitude due to their large cyclotron masses and curvature factors [cf. Fig. 4.16 (d)], explaining their absence in experiment.

With the frequency branches detected in our studies an unambiguous assignment of oscillation frequencies to the calculated FS including small band shifts is achieved. Our results indicate that an empirical correction of the band structure, using the band shifts reported here, is necessary. A more detailed understanding of the Fermi surface of CoSi is expected to facilitate more precise calculations of its response

functions, thereby enabling a better comparison between experimental results and theory in the search for signatures of topological features in its band structure.

4.4 Band topology

The band structure of CoSi forms a network of topological charges beyond the simplified picture focusing solely on the multifold degeneracies located at the Γ- and R-point. The Berry curvature contributions arising from further degeneracies are expected to markedly influence topological response functions. Their energetic distance from the Fermi level, or correspondingly their distance from the Fermi surface in reciprocal space, is crucial for their impact on the material properties. The closer topological crossings are located to the Fermi surface, the more significant their influence is expected to be. The experimental identification of nodal plane degeneracies and the refined knowledge about the Fermi surface resulting from our studies allows us to infer general features of the global band topology and comment on the location of all topological degeneracies with respect to the Fermi surface.

Our comprehensive explanation of the quantum oscillation spectrum arising from extremal trajectories around the R-point unambiguously confirms the existence of nodal planes and a SOC-induced splitting of the band in CoSi. Taken together with an analysis of topological crossing points located in the interior of the BZ, the NPs are enforced to carry a topological charge. A complete description of the band topology of CoSi necessitates the consideration of an entire network of interconnected topological defects, including nodal planes, multifold degeneracies at the R- and Γ-point, and Weyl points located throughout the BZ.

The distribution of topological crossings in the vicinity of the Γ- and R-point is depicted in Figure 4.18. While the multifold crossings at the Γ- and R-point carry a large topological charge, they are located a considerable distance away from the FS. In contrast, Weyl points along high-symmetry lines are located very close to the FS around the Γ-point. Furthermore, the topological protectorates located around the R-point are the intersection of a topological defect, i.e., the nodal planes, with the Fermi surface. The charge of the nodal planes is enforced by SOC and predicted to have no upper limit [91]. Consequently, the topological protectorates provide a mechanism to pin a large Berry curvature directly to the Fermi level.

In general, the response functions depend in a nontrivial way on the flow of Berry curvature through the Fermi surface and explicit integrations have to be performed.

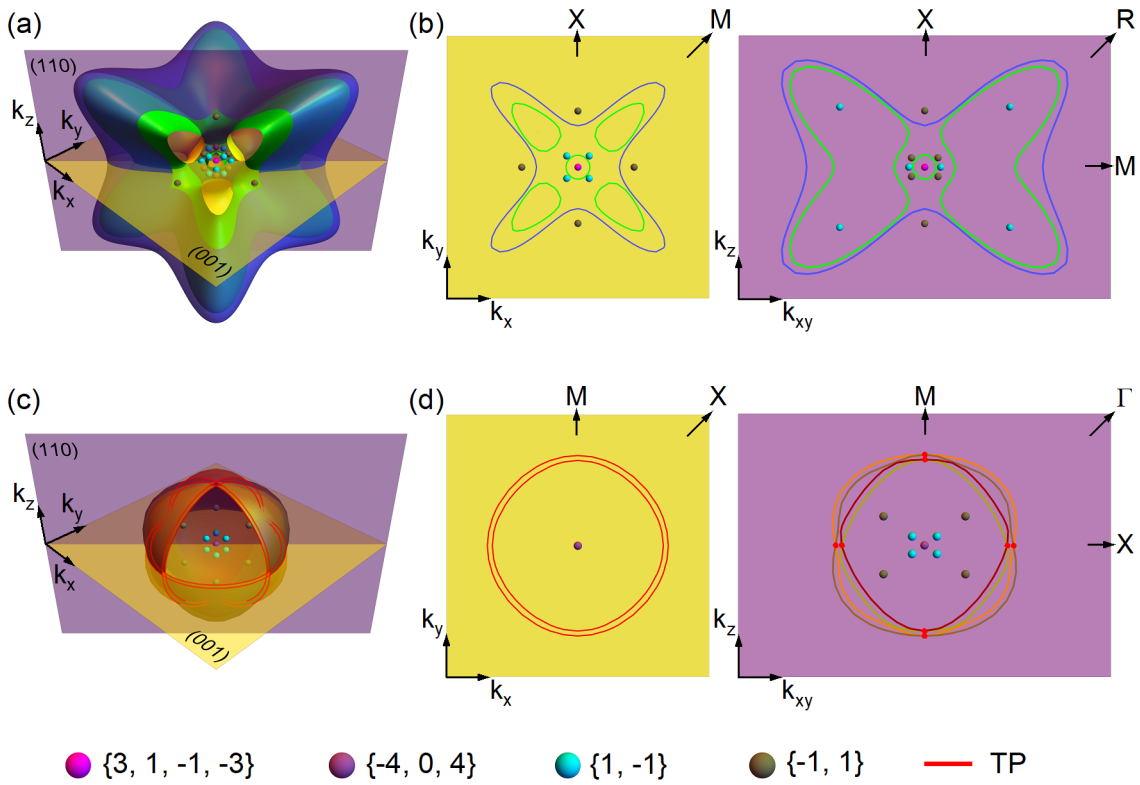

Figure 4.18: Location of topological crossings with respect to the Fermi surface. (a), (c) Perspective views of the FS pockets centered around the Γ- and R-point. Part of the FS has been left out to allow for a view of the crossing points located inside the pockets. (b), (d) FS contours on high-symmetry planes around the Γ- and R-point. The position of topological crossing points is indicated by colored dots. The charge of the bands involved in the crossing is given in curly brackets in order of increasing band energy. Red lines denote topological protectorates (TPs) at which the nodal planes on the BZ boundary cross the Fermi energy.

However, the net flow of Berry curvature through the Fermi surface does in some specialized cases, e.g., the quantized circular photogalvanic effect [50, 83] determine the topological responses. We therefore summarize the topological charge enclosed by the FS pockets in the following.

We begin with the FS pockets around the Γ-point, shown in Fig. 4.18 (a) and (b). The innermost spherical pocket encloses only the multifold crossing point and consequently a net charge of +3. The Weyl points surrounding this pocket are not surrounded by any closed part of the Fermi surface from the underlying bands and therefore do not contribute a quantized flux through it. The outer FS pocket arising from band 3 around the Γ-point encloses Weyl points along the Γ-R line contributing a topological charge of $(1 \times 8) = 8$. The outermost FS sheet, depicted in blue shading,

arises from band 4. It encloses the fourfold crossing at the Γ-point as well as the Weyl points located along Γ-R leading to a net charge of $(1 \times 1 - 1 \times 8) = -7$.

Next, we focus on the FS around the R-point arising from bands 5, 6, 7, and 8. No quantized charge for the sixfold crossing at the R-point can be assigned to any single band because it resides on a nodal plane. We therefore use the non-Abelian Berry curvature [75] to calculate the charge enclosed by pairs of bands, yielding $\{-4, 0, 4\}$ for band pairs (3,4), (5,6), and (7,8). Although the nodal planes carry topological charges of $\{-5, 5\}$ for bands 5 and 6 and $\{-1, 1\}$ for bands 7 and 8, they do not contribute a quantized charge through the Fermi surface because they are not fully enclosed by it. Weyl points in the vicinity of the R-point contribute a quantized charge to a band pair if the crossing does not take place between the bands forming the pair because its topological charge then simply compensates itself. This is the case for the Weyl points depicted in cyan color in Fig. 4.18 (c). We find a net charge of $(1 \times 0 + 1 \times 8 - 1 \times 8 - 1 \times 8) = -8$ enclosed by the FS arising from band pair (5,6) with no contribution from the multifold crossing at R, the Weyl points between bands 5 and 6 compensating themselves, and further Weyl points on the Γ-R line between bands 6 and 7 contributing a charge of (-1×8). Band pair (7,8) encloses a total charge of $(1 \times 4 + 1 \times 8) = +12$ from the multifold crossing point and the Weyl points located along Γ-R.

4.5 Summary and outlook

In summary, the detailed quantum oscillatory studies reported in this chapter unambiguously confirm the existence of topological nodal planes and the relevance of spin-orbit coupling in CoSi. We reconciled open questions about the interpretation of the remarkably simple quantum oscillation spectrum related to the FS around the R-point and advanced the understanding of the Fermi surface of CoSi around the Γ-point through the observation of previously undetected oscillation frequencies. Our results reveal a network of interconnected topological charges comprising multifold crossing points, nodal planes on the Brillouin zone boundary, and further Weyl points located throughout the BZ. A comprehensive picture, taking into account all topological charges beyond isolated degeneracies, is expected to improve the calculation of response functions and lead to a better understanding of the topological properties of this material and further compounds with the same structure.

Further compounds within the same material class including PdGa and AlPt have been synthesized in our group and are the subject of ongoing studies. The larger

atomic masses of their constituent elements leads to a stronger SOC-induced splitting of the bands that significantly changes the band structure and resulting Fermi surface. Both compounds feature large pockets around the R-point, a complex FS structure around the Γ-point and additional pockets around the M-point. Because the M-point is located at the BZ boundary, quantum oscillations arising from the FS around it also show signatures of the nodal plane degeneracies. Furthermore, the detection of combination frequencies in the SdH spectra of CoSi reported in Chapter 5 suggests that frequencies arising from the same mechanism might also be present in related compounds. However, the complex Fremi surfaces of PdGa and AlPt and the many resulting frequencies in their quantum oscillation spectra render a clear identification of combination frequencies challenging. Another interesting question is the relevance of near-degeneracies for the FS pockets around the R-point [140, 204]. Since the size of these pockets increases from CoSi, over AlPt to PdGa, the trajectories giving rise to quantum oscillations reside in different regions of k-space. A comparison between the different compounds might provide a way to test the general relevance of quasi-symmetries [140] for the existence of near-degeneracies in this material class.

Part of the work presented in this chapter has been published in Refs. [152] and [205]. Preliminary measurements have been performed as part of a preceding Master's thesis [188].

5 Quantum Oscillations of the Quasiparticle Lifetime

Quantum oscillations have proven to be a powerful tool in the determination of the electronic structure of metallic systems. Physical properties, such as the magnetization or conductivity, exhibit $1/B$-periodic oscillations due to Landau quantization of the electronic states. The oscillation frequencies are linked to the semi-classical motion of quasiparticles on extremal Fermi surface trajectories perpendicular to the applied magnetic field, as described by the famous Onsager relation [128]. Further properties, such as the cyclotron mass of charge carriers or the phase of the oscillations, provide valuable information on electronic correlations [206–208] or the topological properties of the underlying bands [43, 209–211]. The description of complex Fermi surfaces featuring multiple orbits relies on the independent-band picture, in which the total response is a superposition of the contributions arising from different parts of the FS. Interactions between bands are typically only accounted for by a renormalization of band properties.

The finite lifetime of quasiparticles is commonly treated within the relaxation time approximation. Each individual band is assigned a constant relaxation time τ, that broadens the Landau levels and damps oscillation amplitudes through the well-known Dingle damping factor [212]. However, as we will demonstrate below, this method has limitations. The effects of interactions between quasiparticles are much richer and the lifetime itself can exhibit quantum oscillations. If there is a significant coupling between multiple orbits, these lifetime oscillations may lead to distinct features in the quantum oscillation spectra beyond a simple renormalization of contributions from independent bands.

In this chapter, we report on the detection of combination frequencies in the Shubnikov-de Haas (SdH) spectra of CoSi. We confirm their identification as combination frequencies through their angular dispersion and analyze the temperature dependent damping of their oscillation amplitudes. Then, we discuss mechanisms that are known to give rise to combination frequencies in quantum oscillation spectra and show that they cannot account for our experimental findings. Finally, we explain how the observed combination frequencies can be attributed to oscillations of the quasiparticle lifetime and discuss the general relevance of the proposed mechanism.

5.1 Detection of combination frequencies

In this section, we analyze the SdH oscillations in the longitudinal and Hall resistivity of CoSi in more detail. The most prominent feature in the quantum oscillation spectra, i.e., the two oscillation frequencies arising from quasiparticle trajectories on FS sheets centered around the R-point, are described in detail in Sec. 4.2 and are only briefly recapitulated here. The focus of this chapter is on the detection of combination frequencies. We observe these frequencies in all three samples investigated and focus on the data obtained from the most extensively characterized sample, HKZ7 S1, in the following. We show the angular dispersion and temperature dependence of the SdH spectra and discuss the behavior of the combination frequencies in detail.

We probed the magnetotransport properties of CoSi by recording both the magnetoresistivity, ρ_{xx}, and Hall resistivity, ρ_{xy}, simultaneously. Figure 5.1 (a) shows an exemplary dataset at $T = 300\,\mathrm{mK}$ with the magnetic field applied along the [001] crystallographic direction. Fig. 5.1 (b) shows the oscillatory part of the data after subtraction of a polynomial background. Both signals display characteristic $1/B$-periodic SdH oscillations with a beating pattern, indicating two nearly identical frequencies dominating the signal. The corresponding normalized FFT spectra, analyzed in the field range between 9 T and 18 T, are shown in Fig. 5.1 (c). Two strong frequencies f_α and f_β and their higher harmonics are detected. A detailed discussion of these oscillations frequencies and their origin in extremal trajectories on the FS pockets centered around the R-point is given in Section 4.2. There are two further frequency components visible in the spectra. They exhibit a significantly smaller amplitude than the main frequencies f_α and f_β, but can be clearly detected above the noise floor. Close-up views of the regions containing the additional frequencies are shown in Fig. 5.1 (b) and (c). These frequencies correspond to the difference $f_{\beta-\alpha}$ and sum $f_{\alpha+\beta}$ of f_α and f_β. While the combination frequencies are detectable in both the longitudinal and Hall resistivity, the difference frequency is more pronounced in the ρ_{xy} signal and the sum frequency is stronger in the ρ_{xx} signal. Remarkably, these frequencies cannot be explained by extremal trajectories on the FS of CoSi or conventional mechanisms, that are known to lead to combination frequencies in QO spectra. Especially the difference frequency $f_{\beta-\alpha}$ is forbidden in the picture of semi-classical quasiparticle trajectories.

To further investigate the correspondence between f_α and f_β and the additional frequencies detected, we conducted angular-dependent measurements of the SdH oscillations at 300 mK. The field was rotated in a $(1\bar{1}0)$ plane and the angle θ is

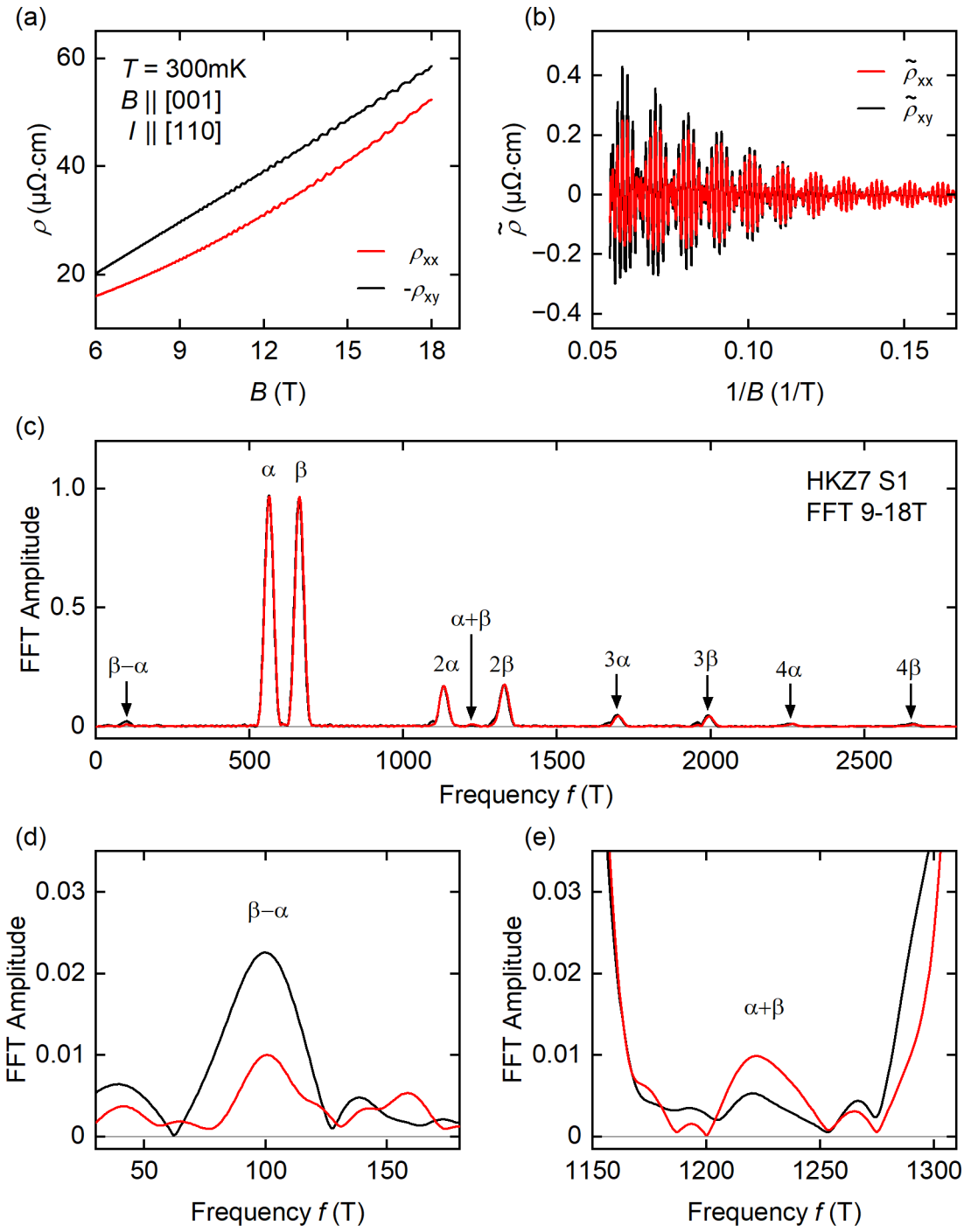

Figure 5.1: Combination frequencies in the SdH oscillations. (a) Magneto- and Hall resistivity at $T = 300\,\mathrm{mK}$ as a function of the applied magnetic field B along the [001] direction. (b) Oscillatory part of the resistivity as a function of inverse field after subtraction of a polynomial background. (c) Normalized FFT spectra of the data shown in (b). There are two dominant frequencies f_α and f_β as well as their higher harmonics visible in the spectrum. Additionally, frequency contributions can be discerned at the difference $f_{\beta-\alpha}$ and sum $f_{\alpha+\beta}$. (d) Close-up view of the frequency region containing the difference frequency. (e) Close-up view of the frequency region containing the sum frequency. The peaks to the left and right of the sum frequency are the 2nd harmonics of f_α and f_β. The amplitudes of the combination frequencies differ for the different signals recorded.

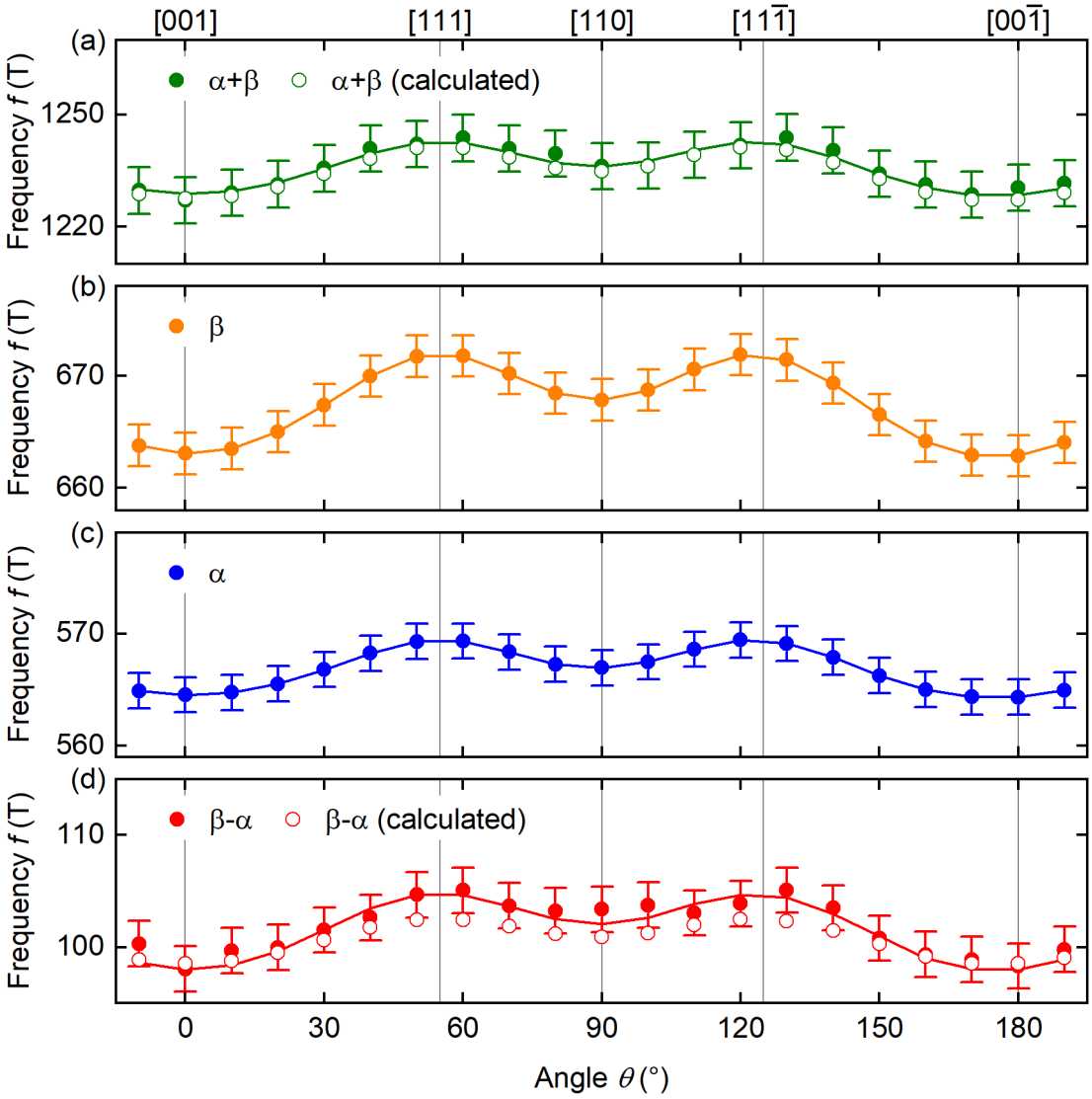

Figure 5.2: Angular dependence of SdH frequencies. (a)-(d) Oscillation frequencies extracted from the SdH oscillations in ρ_{xx} as a function of the angle of the applied magnetic field θ. Open circles denote the calculated sum and difference of frequencies α and β. The experimentally extracted values of $\alpha + \beta$ and $\beta - \alpha$ closely follow the calculated values over the whole angular range. Error bars are derived from a comparison of datasets recorded at increasing and decreasing magnetic fields. Lines are drawn as a guide to the eye.

measured from the crystallographic [001] direction. Because the contact geometry of the ρ_{xy} signal changes with the orientation of the sample and the signal vanishes for certain field directions, we used the ρ_{xx} signal to track the frequencies in the FFT spectra. The peaks have been fitted with Gaussians and the uncertainty of the extracted frequencies was estimated by comparing the values obtained from measurements for increasing and decreasing magnetic field. The frequencies as a function of θ are shown in Fig. 5.2. All detected frequencies exhibit a small but

distinct angular dispersion. It follows the same behavior for all frequencies with maxima for fields along the [111] direction and local minima for fields along the [001] and [110] direction. The frequency variations of f_α and f_β amount to 5 T and 9 T, respectively. Consequently, the calculated sum and difference between the two, shown as open symbols, also exhibit a distinct angular dispersion. A comparison between the calculated combination frequencies and the experimentally determined frequencies $f_{\alpha+\beta}$ and $f_{\beta-\alpha}$ shows that they closely follow each other over the entire angular range investigated. This provides compelling evidence that the detected frequencies indeed correspond to the sum and difference of f_α and f_β.

Next, we analyze the temperature dependence of the oscillation amplitudes with the magnetic field applied along the crystallographic [001] direction. This direction allows us to detect the oscillations in both ρ_{xx} and ρ_{xy} with full signal strength. Figure 5.3 shows the FFT spectra recorded at different temperatures ranging from 20 mK to 70 K. An overview of the FFT spectra obtained from the ρ_{xx} signal is shown in Fig. 5.3 (a). f_α and f_β are detectable up to a temperature of about 8 K. Their higher harmonics exhibit a stronger temperature dependent damping and are detected up to a temperature of 2.5 K. The behavior of f_α, f_β and their higher harmonics is almost identical in the FFT spectra obtained from the ρ_{xy} signal.

The frequency regions containing combination frequencies are shown in panels (b) and (c) for the ρ_{xx} signal and in panels (d) and (e) for the ρ_{xy} signal. While both combination frequencies are clearly discernible in both signals, there are subtle differences we discuss in the following. The difference frequency $f_{\beta-\alpha}$ is the strongest combination frequency detected, exhibiting an amplitude amounting to $2-2.5\,\%$ of the main frequencies f_α and f_β at the lowest temperatures. It shows a slightly larger amplitude in the ρ_{xy} data as compared to ρ_{xx}. Remarkably, it exhibits only a small temperature dependent damping and is detectable up to temperatures of about 50 K in both signals, at which all other frequency components are completely suppressed. There are small differences in the low-temperature behavior of $f_{\beta-\alpha}$ between the ρ_{xx} and ρ_{xy} signal, that are described in more detail further below. The sum frequency $f_{\alpha+\beta}$ exhibits a slightly larger amplitude in the ρ_{xx} signal as compared to the ρ_{xy} signal. Its amplitude amounts to about 1 % of the main frequencies at 20 mK. It exhibits strong damping with increasing temperature and is detectable above the noise floor up to a temperature of about 1 K in both signals.

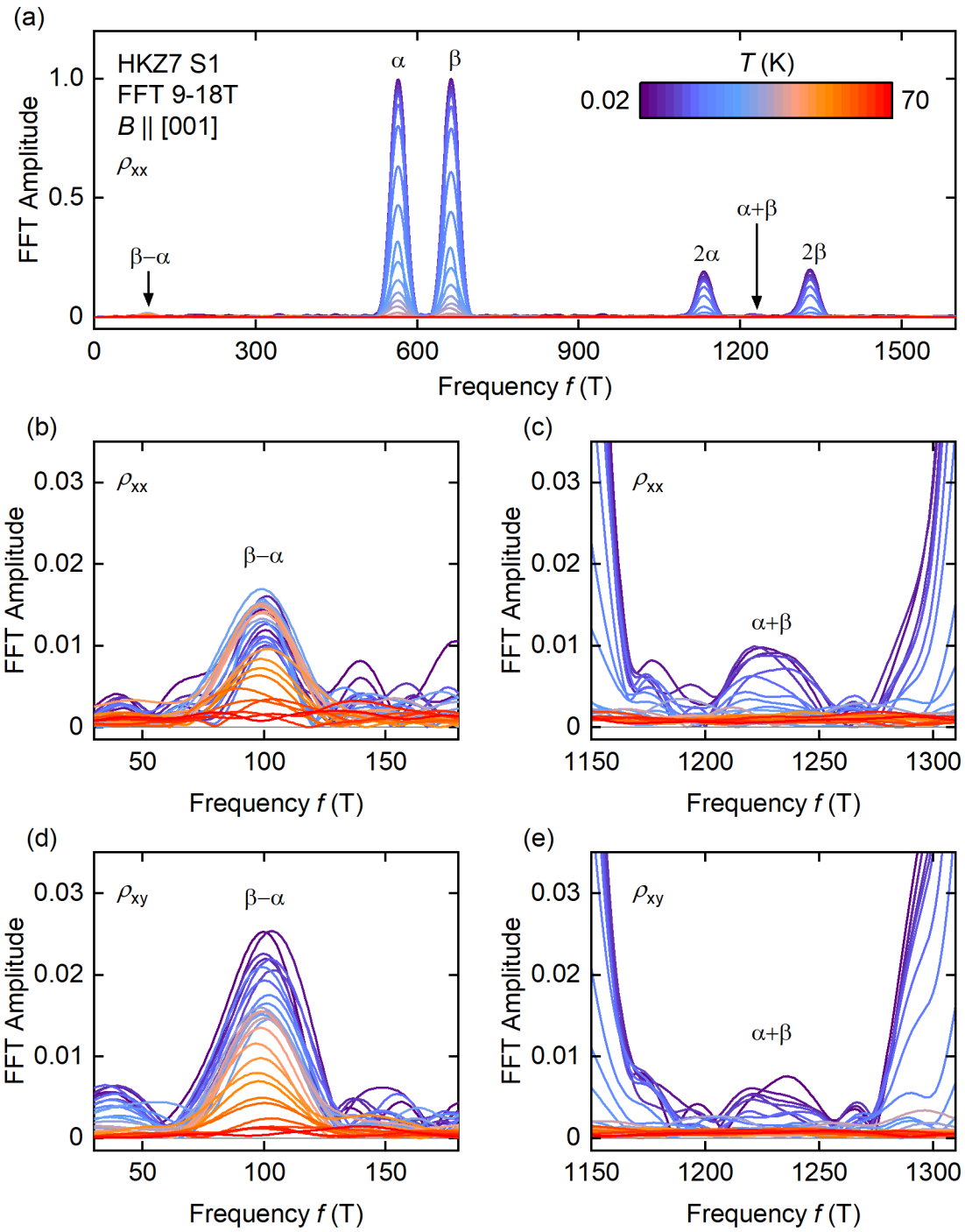

Figure 5.3: Temperature dependence of the FFT spectra. (a) Fourier spectra of the SdH oscillations in the magnetoresistance ρ_{xx} recorded at different temperatures between 20 mK and 70 K. (b), (c) Close-up views of the frequency regions containing the difference and sum frequency for ρ_{xx}. The difference frequency contribution is detected up to a temperature of 50 K at which all other frequencies are completely suppressed. (d), (e) Close-up views of the frequency regions containing the difference and sum frequency for ρ_{xy}. While the overall behavior is similar to the oscillations in ρ_{xx}, subtle differences are present in the amplitudes of the combination frequencies and the low-temperature behavior of the difference frequency.

We further illustrate the remarkable temperature stability of the difference frequency in Fig. 5.4 (a), in which the oscillatory part of ρ_{xx} as a function of $1/B$ is shown at elevated temperatures. The curves are offset by a constant for better visibility. At 2.5 K the signal is dominated by fast oscillations with a superimposed beating pattern, corresponding to the frequencies f_α and f_β. At higher temperatures the fast oscillations are no longer present in the signal and smaller slow oscillations are clearly visible. These oscillations correspond to the difference frequency $f_{\beta-\alpha}$. By comparing the phase of the oscillations, we find that the minima of the slow oscillations coincide with the nodes of the beating pattern of the fast oscillations, which are marked by vertical lines. This fixed phase relation is a further indicator that the origin of $f_{\beta-\alpha}$ lies in frequencies f_α and f_β.

The cyclotron masses for each frequency can be determined by analyzing the temperature dependent damping of oscillation amplitudes within the LK formalism. The FFT amplitudes were extracted from Gaussian fits of the individual peaks. Figure 5.4 (b)-(d) shows the amplitudes of the different frequency components as a function of temperature. The solid lines represent fits with the LK temperature reduction factor $\mathrm{R_T}$. The amplitudes of frequencies f_α and f_β exhibit a very similar temperature dependent damping yielding cyclotron masses of $m^*_\alpha = (0.92 \pm 0.01)\, m_e$ and $m^*_\beta = (0.96 \pm 0.01)\, m_e$. The sum frequency $f_{\alpha+\beta}$ shows a stronger temperature dependence involving an effective mass of $m^*_{\alpha+\beta} = (1.9 \pm 0.4)\, m_e$. The difference frequency $f_{\beta-\alpha}$ exhibits an almost constant amplitude below 1 K, followed by a slight increase of amplitude in the range between 1 K and 5 K and a LK-like behavior at temperatures above 5 K. The data was fitted with the temperature reduction factor $\mathrm{R_T}$ in the range between 2 K and 60 K and the extracted effective mass is $m^*_{\beta-\alpha} = (0.06 \pm 0.01)\, m_e$. The effective masses of $f_{\beta-\alpha}$ and $f_{\alpha+\beta}$ correspond to the difference and sum of the individual effective masses of f_α and f_β within the experimental error.

A similar behavior is observed for the oscillations in ρ_{xy}. Figure 5.5 (a) illustrates the oscillatory part of ρ_{xy} as a function of $1/B$. The minima of the slow oscillations, which are again clearly visible at elevated temperatures, coincide with the same field values observed for the ρ_{xx} signal and correspondingly again align with the nodes in the beating pattern of the fast oscillations, visible at lower temperatures. The oscillation amplitudes as a function of temperature are shown in Fig. 5.5 (b)-(d). The behavior of frequencies f_α, f_β and $f_{\alpha+\beta}$ is almost identical, yielding the same effective masses within the experimental uncertainty. There is, however, a

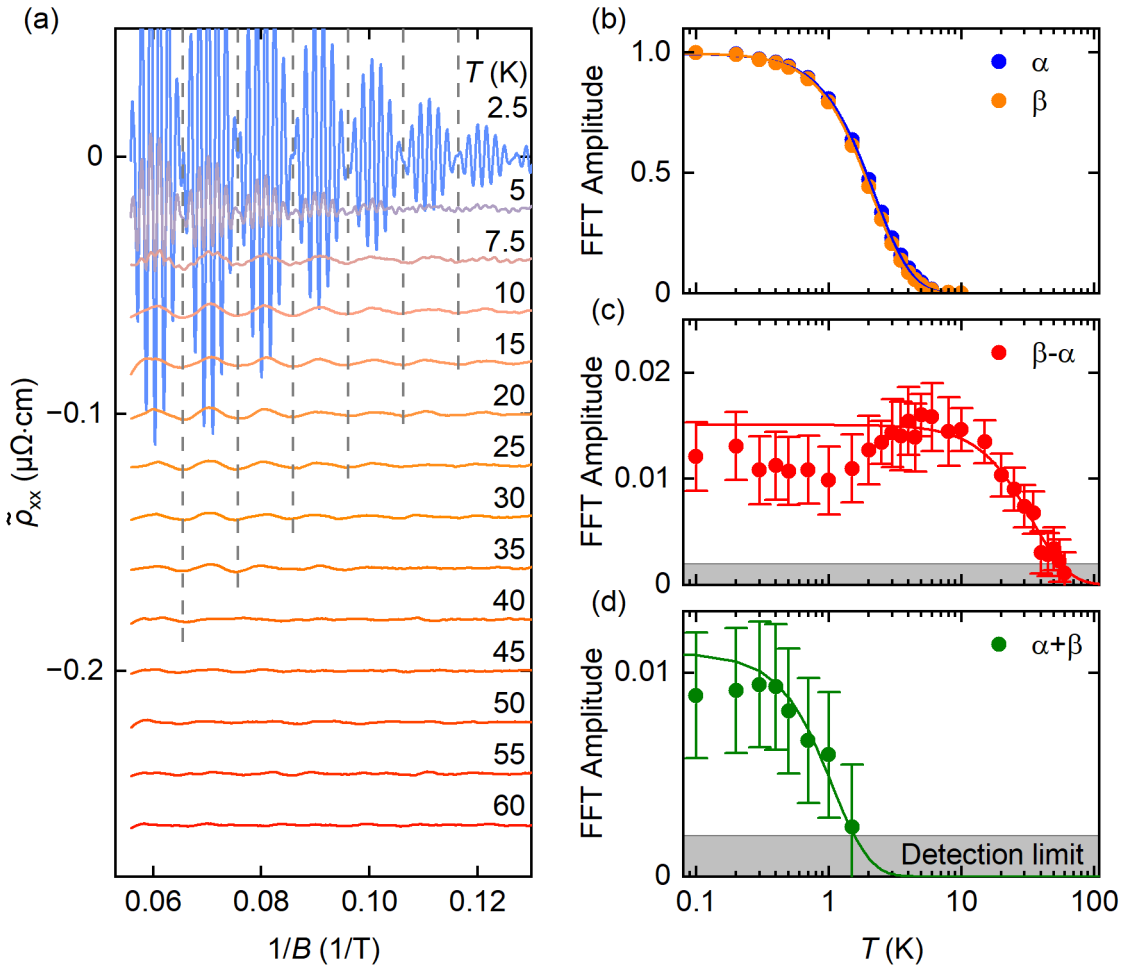

Figure 5.4: Temperature dependence of SdH oscillations in the magnetoresistance. (a) Oscillatory part of the longitudinal resistivity $\tilde{\rho}_{xx}$ as a function of the inverse applied magnetic field $1/B$ recorded at different fixed temperatures. Curves are offset for clarity. The slow oscillations visible at temperatures above 5 K correspond to the frequency $\beta - \alpha$. Their fixed phase relation with regard to the fast oscillations visible at 2.5 K is indicated by the vertical lines. (b) FFT amplitudes of frequencies α and β as a function of temperature T. The lines represent fits of the LK temperature reduction factor $\mathrm{R_T}$ yielding effective masses of $m^*_\alpha = (0.92 \pm 0.01)\, m_e$ and $m^*_\beta = (0.96 \pm 0.01)\, m_e$. Error bars are smaller than the data points. (c) FFT amplitudes of the difference frequency $\beta - \alpha$. A fit of the data between 2 K and 60 K with $\mathrm{R_T}$ yields an effective mass of $m^*_{\beta-\alpha} = (0.06 \pm 0.01)\, m_e$. (d) Oscillation amplitudes of the sum frequency $\alpha + \beta$. The line represents a LK fit yielding an effective mass of $m^*_{\alpha+\beta} = (1.9 \pm 0.4)\, m_e$.

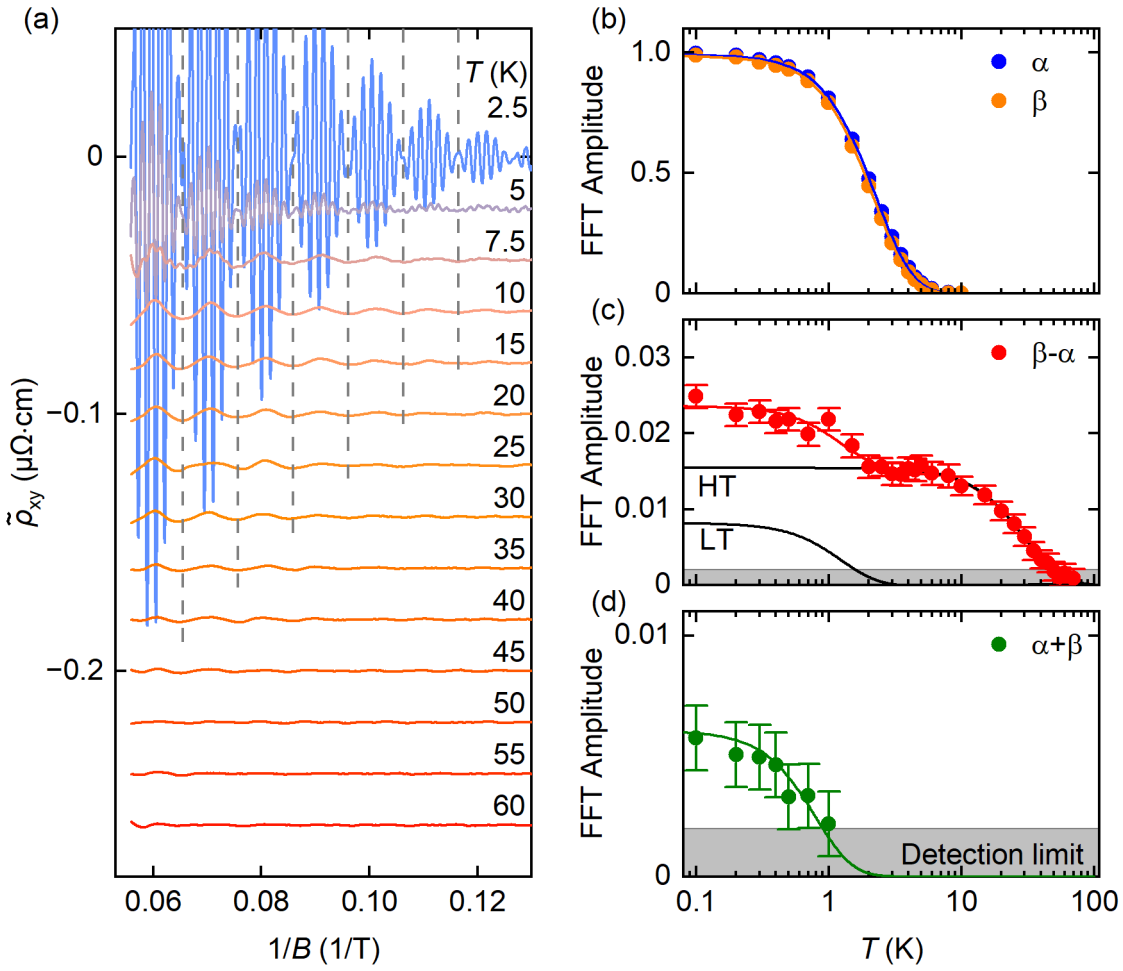

Figure 5.5: Temperature dependence of SdH oscillations in the Hall resistivity. (a) Oscillatory part of the Hall resistivity $\tilde{\rho}_{xy}$ as a function of the inverse applied magnetic field $1/B$ recorded at different fixed temperatures. Curves are offset for clarity. The fixed phase relation between the fast oscillations at low temperatures and the slow oscillations at elevated temperatures is indicated by vertical lines. (b) FFT amplitudes of frequencies α and β as a function of temperature T. The lines represent fits of the LK temperature reduction factor $\mathrm{R_T}$ yielding effective masses of $m^*_\alpha = (0.92 \pm 0.01)\, m_e$ and $m^*_\beta = (0.95 \pm 0.01)\, m_e$, consistent with the values obtained from the oscillations in ρ_{xx}. Error bars are smaller than the data points. (c) Oscillation amplitudes of the difference frequency $\beta - \alpha$. The temperature dependent damping is analyzed as a two component $\mathrm{R_T}$ fit yielding effective masses of $m^*_{\mathrm{LT}} = (1.6 \pm 0.3)\, m_e$ for the low temperature regime (LT) and $m^*_{\mathrm{HT}} = (0.07 \pm 0.01)\, m_e$ for the high temperature regime (HT). The individual components of the fit are shown as black lines. (d) Oscillation amplitude of the sum frequency $\alpha + \beta$. A fit of the temperature reduction factor $\mathrm{R_T}$ yields an effective mass of $m^*_{\alpha+\beta} = (2.6 \pm 0.4)\, m_e$.

difference in the behavior observed in the temperature dependence of the difference frequency. Although the relative oscillation amplitudes and their damping are nearly identical in the high-temperature range, a distinct upturn in oscillation amplitudes is observed with decreasing temperature below 5 K. This behavior can be described by a two-component LK fit, comprising a high-temperature (HT) part and a low-temperature (LT) part. The extracted effective masses are $m^*_{\mathrm{LT}} = (1.6 \pm 0.3)\, m_e$ and $m^*_{\mathrm{HT}} = (0.07 \pm 0.01)\, m_e$. Our findings suggest that there is an additional contribution to the difference frequency oscillations at low temperatures that manifests differently in ρ_{xx} and ρ_{xy}.

5.2 Comparison to conventional mechanisms

The main experimental observations reported in this chapter that need to be explained theoretically are as follows. First, we detect frequency contributions in the SdH spectra of CoSi which are combinations of the frequencies arising from the FS around the R-point. Second, the difference frequency exhibits a very weak temperature dependent damping whose high-temperature part can be described by a LK damping factor involving the difference of the cyclotron masses of the underlying frequencies. The temperature damping of the oscillations at the sum frequency is consistent with a LK temperature reduction factor $\mathrm{R_T}$ involving the sum of the underlying cyclotron masses.

Conventional mechanisms that are known to lead to combination frequencies in quantum oscillatory are described in Sec. 2.4. Here, we compare the experimentally observed characteristics of the combination frequencies in CoSi with each mechanism and conclude that the behavior deviates from the theoretical expectations for magnetic breakdown, magnetic interaction, and chemical potential oscillations and that the conditions required for quantum interference are not met.

Magnetic breakdown (MB) could theoretically explain the existence of a sum frequency. However, as discussed in detail in Sec. 4.2.2, the calculated frequencies arising from MB between the pockets located around the R-point of CoSi lie on two frequency branches with frequencies in between the frequencies that would be expected without MB due to the nested nature of the pockets. For a sum frequency, the amplitude would be expected to exhibit a pronounced angular dependence with a diminishingly small amplitude for certain field directions, e.g., when the magnetic field is applied along the [001] direction. Furthermore, a difference frequency arising from MB is only possible in the case of a mixed electron and hole orbit [213]. However, all FS pockets

around the R-point of CoSi are all electron-like. Hence, a MB breakdown orbit leading to a difference frequency is semi-classically forbidden, as part of the trajectory would involve quasiparticles moving against the direction dictated by Lorentz force [compare Fig. 5.7 (b)]. Moreover, for a breakdown trajectory between an electron and hole orbit, which can yield a difference frequency, one would anticipate a temperature-dependent damping involving the sum of the cyclotron masses of the individual orbits [175]. This is in contrast to the very weak temperature-dependent damping we observe for the difference frequency oscillations in CoSi. We conclude that magnetic breakdown cannot explain the existence of a difference frequency at any angle and does not allow for the explanation of a sum frequency when the magnetic field is applied along the [001] direction.

The next mechanism under consideration is magnetic interaction (MI). In our study of the magnetization oscillations of our samples using vibrating sample magnetometry we find that $|\mathrm{d}\tilde{M}/\mathrm{d}H|$ is on the order of 10^{-4}, much smaller than what would be necessary for a significant MI effect. Moreover, the oscillations in the magnetization are strongly damped by temperature and entirely suppressed above 10 K. Combination frequencies arising from MI are expected to vanish even faster than the underlying frequencies, which is in stark contrast our observation of a difference frequency persisting up to almost 50 K.

Chemical potential oscillations, mostly known from (quasi-)two-dimensional materials, can give rise to combination frequencies. However, in three-dimensional materials CPOs are suppressed due to a large reservoir of unquantized electronic states along the field direction, which do not contribute to the oscillations and act as a reservoir, keeping the chemical potential nearly constant. Given the three-dimensional FS of CoSi, which hosts several FS pockets far away from the quantum limit, CPOs are expected to be vanishingly small. Moreover, CPOs are expected to be suppressed by temperature stronger than the oscillations in other thermodynamic properties. Consequently, the combination frequencies should also display a temperature dependent damping similar to their constituent frequencies, which is in contrast to the temperature stability of the difference frequency observed.

The last mechanism, exhibiting very similar characteristics to the ones observed in CoSi, is quantum interference. However, it requires FS trajectories connected by partial magnetic breakdown junctions, contrasting the situation found in CoSi. For the FS trajectories around the R-point of CoSi, no MB is expected if the field is

applied along the [001] direction. For other field directions the observed oscillation frequencies imply that there is complete magnetic breakdown at every breakdown junction in the field range in which quantum oscillations are observed. Consequently, for almost all field orientations, there are no partial magnetic breakdown trajectories that could realize the requisite interferometer geometry. Thus, we conclude that the observation of combination frequencies over the whole angular range investigated rules out quantum interference as the underlying mechanism.

5.3 Quasiparticle lifetime oscillations

In this section, we propose a mechanism that explains the existence and unusual behavior of the observed combination frequencies through oscillations in the quasiparticle lifetime (QPL). First, we describe the Fermi surface geometry around the R-point of CoSi and present a minimal model that captures its essential features. Then, we examine the implications of oscillations in the density of states on the QPL and explain its influence on the QO spectra. We show that oscillations of the QPL give rise to combination frequencies in the presence of interorbit coupling. Finally, we describe how the effects of finite temperature are taken into account in the LK formalism and how it can be extended to frequencies stemming from quasiparticle lifetime oscillations.

We note that the proposed mechanism is a generalization of the theory describing magneto-intersubband oscillations (MISOs). They have been detected and explained in two-dimensional electron systems [214–218] and quasi-two-dimensional materials [219–221]. However, to the best of our knowledge neither their relevance for three-dimensional materials nor the formulation via oscillations of the quasiparticle lifetime has been appreciated in these studies.

5.3.1 Minimal model

The Fermi surface of CoSi around the R-point consists of four electron-like pockets resulting from four spin-split bands intersecting on nodal planes located at the BZ boundary. These pockets give rise to two almost dispersionless frequency branches f_α and f_β. A detailed explanation of how this surprisingly simple quantum oscillation spectrum, featuring just two frequencies, can be explained is provided in Section 4.2. Here, we briefly summarize the key points and show how the extremal trajectories can be described by a minimal model of two linearly dispersing bands.

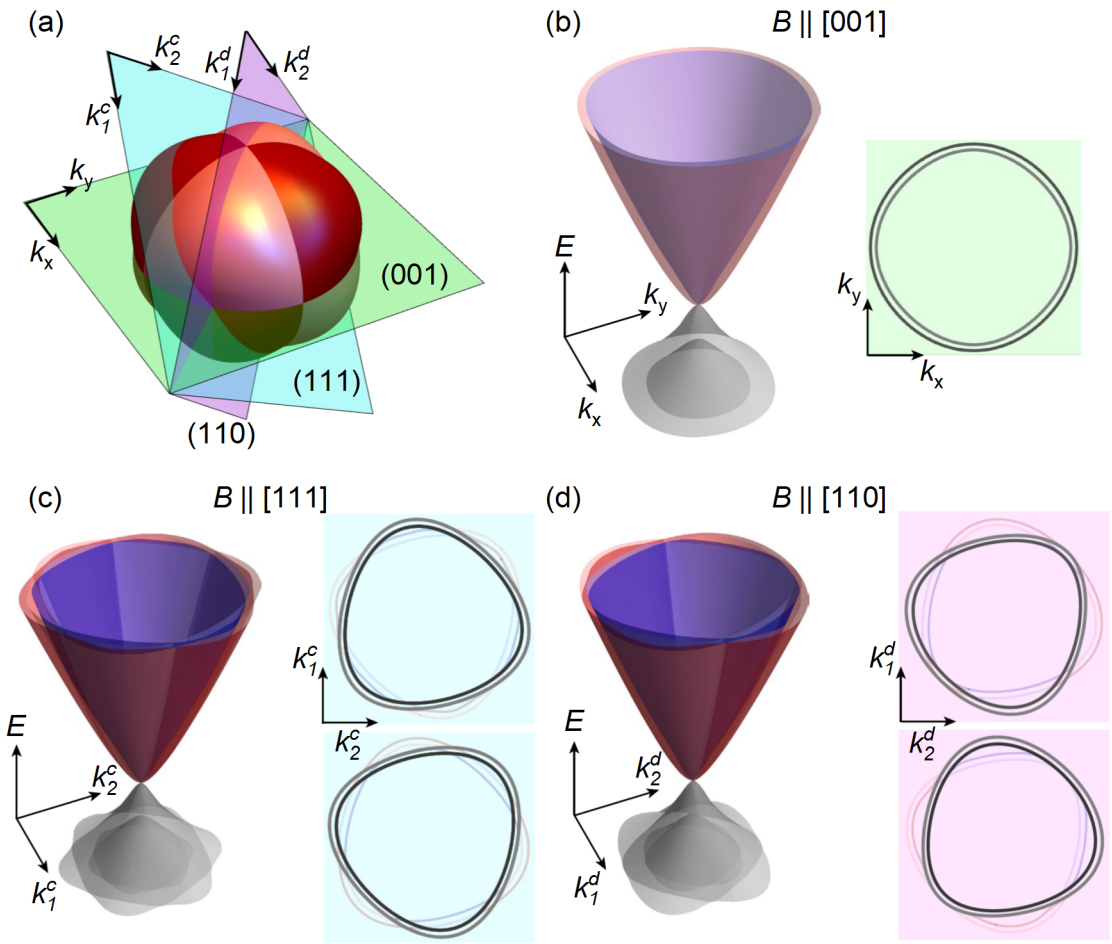

Figure 5.6: Fermi surface pockets around the R-point of CoSi. (a) The FS around the R-point of CoSi consists of four electron-like pockets that intersect each other at the nodal planes. In order to visualize the extremal orbits in planes perpendicular to the applied magnetic field, we show cross sections of the pockets in the (001), (111) and (110) plane. (b) Energy dispersion of the band structure of CoSi around the R-point for $B \parallel [001]$ and extremal orbits in the (001) plane. Because the extremal orbits lie on a nodal plane, they are pairwise degenerate and form two almost circular trajectories. (c), (d) Energy dispersion and extremal orbits of CoSi around the R-point for $B \parallel [111]$ and $B \parallel [110]$. The extremal orbits for both field directions consist of two sets of copies that pairwise enclose the same cross-sectional area. They can therefore be considered as two copies of the situation shown in (b).

Illustrated in Figure 5.6 (a) is the FS of CoSi centered around the R-point. It comprises two pairs of nested pockets. For each pair the Fermi surface pockets intersect at the BZ boundary due to degeneracies enforced by the nodal planes. This degeneracy can also be seen in the band dispersion depicted in Fig. 5.6 (b). The bands are shown in the (001) plane which crosses the R-point and coincides with the BZ boundary. Consequently, the four spin-split bands are pairwise degenerate resulting in two

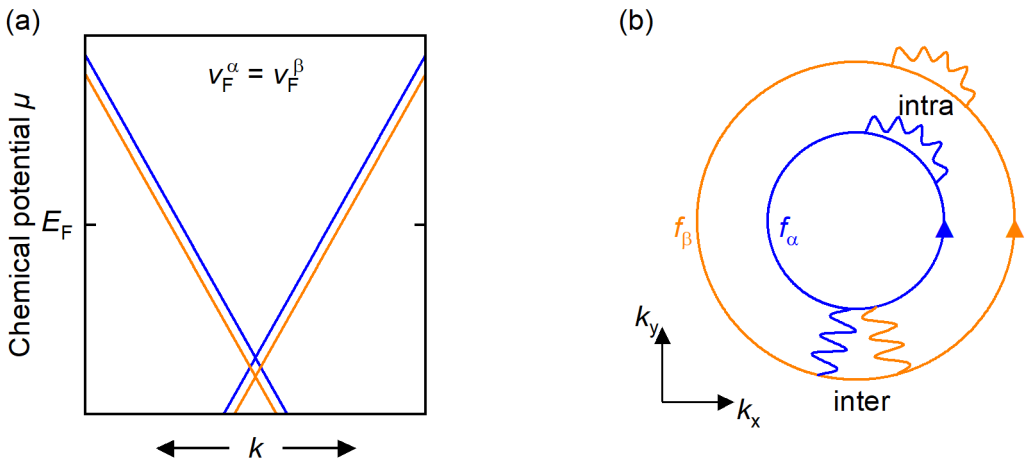

Figure 5.7: Minimal model of the band structure around the R-point of CoSi. (a) Energy dispersion of two linear bands with identical Fermi velocities and an energy offset. This minimal model closely resembles the situation for the bands around the R-point of CoSi at the Fermi energy. (b) The bands give rise to two extremal FS trajectories with cross-sectional areas corresponding to oscillation frequencies f_α and f_β. Scattering can lead to intra- and interband transitions.

bands emerging from the multifold crossing point located ≈200 meV below the Fermi level. In the vicinity of the Fermi level, up to which the dispersion is shown, the bands are almost parallel. The extremal FS trajectories depicted on the right-hand side of Fig. 5.6 (b) consist of two nearly circular orbits with cross-sectional areas corresponding to the experimentally observed frequencies f_α and f_β. The situation is more intricate if we consider FS trajectories perpendicular to magnetic fields tilted away from the [001] direction. The band dispersions and extremal orbits perpendicular to the [111] and [110] direction are presented in Fig. 5.6 (c) and (d), respectively. These orbits no longer exhibit degeneracy along the entire trajectory but intersect each other at the points where they cross the BZ boundary. Moreover, the inner and outer pair of orbits come close to each other at further points along their trajectory. At magnetic field strengths where quantum oscillations are observed, complete magnetic breakdown occurs at these points. Both effects combined yield the trajectories shown on the right-hand side of Fig. 5.6 (c) and (d). They consist of two sets of orbits that pairwise enclose the same cross-sectional areas, again giving rise to the two frequencies f_α and f_β. Therefore, the situation for magnetic fields tilted away from the [001] direction can be understood as two copies of the scenario shown in Fig. 5.6 (b).

A model describing the Fermi surface around the R-point of CoSi needs to fulfill the following two criteria. First, it must encompass two extremal orbits giving rise to two QO frequencies. Second, the band dispersion near the Fermi energy needs to be similar for the two bands involved in order to obtain QOs with similar cyclotron masses. We consider a minimal model comprising two rotationally symmetric, linearly dispersing bands with identical Fermi velocity v_F and an energy offset W. The dispersion is illustrated in Figure 5.7 (a). The two bands give rise to two nested Fermi spheres, resulting in two circular extremal orbits for any direction of the applied magnetic field. The corresponding quasiparticle trajectories are depicted in Fig. 5.7 (b). They closely resemble the orbits around the R-point of CoSi perpendicular to the [001] direction shown in Fig. 5.6 (b). We note that the mechanism we propose also can be applied to quadratically dispersing bands with either an offset in energy or k-space.

5.3.2 DOS and lifetime oscillations

We consider scattering on randomly distributed short-range impurities that gives rise to both intra- and interband coupling. In the Lifshitz-Kosevich formalism, scattering is taken into account through the approximation of a constant relaxation time τ. The resulting Dingle damping factor $\mathrm{R_D}$ yields an exponential dependence of the QO amplitudes via

$$\mathrm{R_D} = \exp\left(-\frac{\pi}{\tau\omega_c}\right) , \tag{5.1}$$

where ω_c denotes the cyclotron frequency. Historically, the relaxation time has also been expressed in terms of the Dingle temperature $T_\mathrm{D} = \hbar/(2\pi k_\mathrm{B}\tau)$, due to the similarity of the resulting damping of QO amplitudes with a temperature reduction factor involving $T^* = T + T_\mathrm{D}$. The Dingle damping factor can then be formulated as

$$\mathrm{R_D} = \exp\left(-\frac{2\pi^2 k_\mathrm{B} T_\mathrm{D}}{\hbar\omega_c}\right) . \tag{5.2}$$

Next, we discuss how oscillations in the density of states (DOS) naturally lead to oscillations of the quasiparticle lifetime or, equivalently, the Dingle temperature. We then distinguish between intra- and interband scattering events and explain their influence on the QO spectra.

The DOS of a Landau quantized two-dimensional system at two magnetic fields $B_1 < B_2$ is depicted in Fig. 5.8 (a). The following discussion can easily be extended to three-dimensional systems, albeit the effect is expected to be more pronounced in two dimensions. With increasing magnetic fields, the Landau level separation and

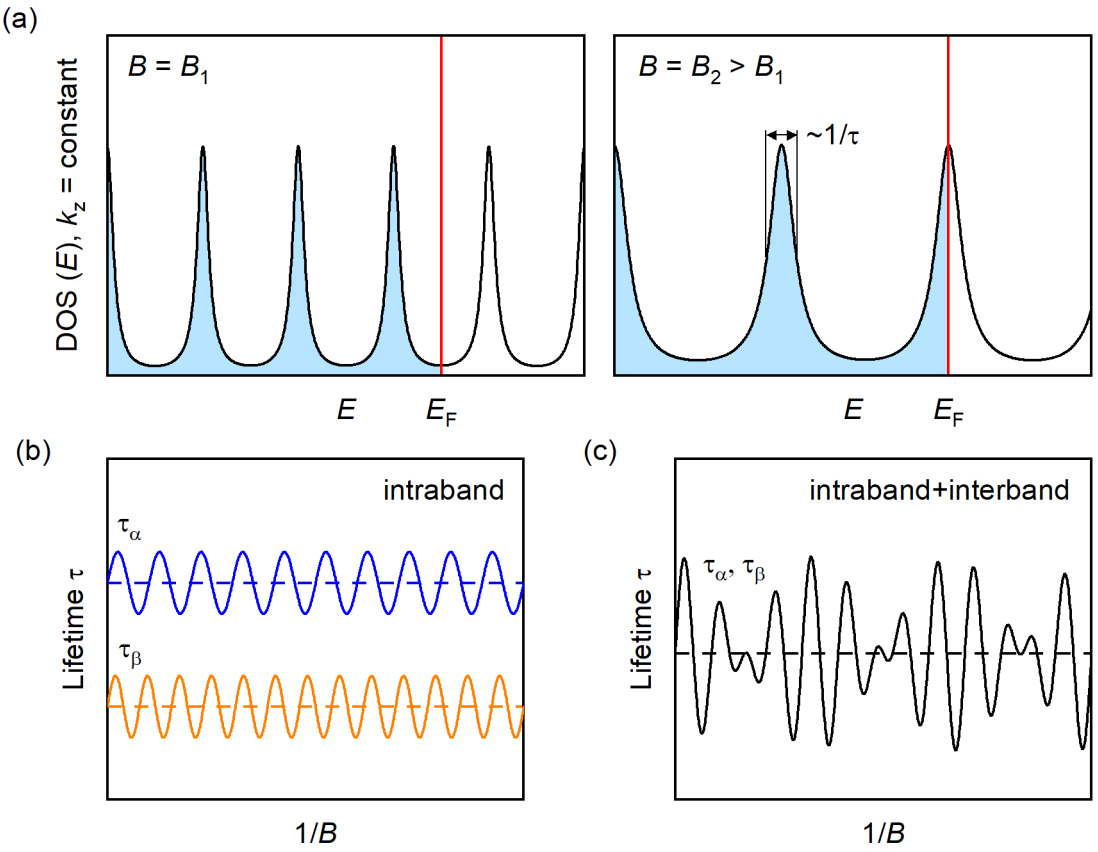

Figure 5.8: DOS and lifetime oscillations. (a) Density of states (DOS) as a function of energy for constant k_z in the presence of Landau quantization. For $B_2 > B_1$ the separation between Landau levels increases leading to oscillations of the DOS at the Fermi energy E_F. The Landau levels are broadened due to the finite quasiparticle lifetime τ. The inverse lifetime is expected to vary with the DOS. (b) If there are purely intraband scattering events present, the lifetime of quasiparticles on one orbit oscillates only with the frequency associated with that particular orbit. (c) If there additionally is interband scattering possible between the orbits, the lifetime of a quasiparticle on one orbit oscillates with a superposition of both frequencies associated with the orbits.

degeneracy increase, leading to $1/B$-periodic fluctuations of the DOS at the Fermi energy E_F. According to Fermi's golden rule [222] the scattering probability depends on the number of states that are available for a quasiparticle to scatter into, i.e., the DOS at E_F. Hence, the scattering probability and consequently the quasiparticle lifetime τ follows the oscillations in the DOS. A well-known consequence of the finite lifetime of quasiparticles is the broadening of Landau levels, where the half-width of the peaks in the DOS is proportional to $1/\tau$. Conventionally, assuming a constant relaxation time, this broadening is reflected in the constant Dingle damping factor R_D. However, if the lifetime is considered to vary with the applied magnetic field, the broadening of Landau levels also changes, as depicted in Fig. 5.8 (a).

First, we examine the scenario involving only intraband scattering. For intraband transitions the band index is not changed by the scattering process and the quasiparticle trajectories on different bands can be treated completely independent of each other. The lifetime of quasiparticles on orbit α (β) as a function of $1/B$ is shown in Fig. 5.8 (b). The constant offset of both curves, depicted by the dashed line, depends on the contribution arising from the non-oscillating part of the DOS and corresponds to a constant Dingle damping factor. Superposed on this constant lifetime are oscillations arising from the oscillatory part of the DOS. The lifetime of a quasiparticle on orbit α (β) oscillates with the frequency f_α (f_β). Since the lifetime for each individual orbit oscillates solely with the frequency corresponding to its cross-sectional area, no mixing of oscillation frequencies is expected in the presence of only intraband scattering. However, the oscillations in the quasiparticle lifetime are expected to influence the harmonic content of the associated quantum oscillations.

If interband scattering is considered in addition to intraband scattering, the resulting coupling between different QO frequencies can give rise to combination frequencies in the QO spectra. They exhibit distinct characteristics which offer a clear experimental signature for QPL oscillations. For first-order interband scattering processes the initial and final state have different band indices. As these processes are suppressed by a factor $T_\mathrm{D}/W \ll 1$, the relevant terms in the evaluation are second-order processes, in which two interband scattering events couple the two orbits but leave the initial and final band index invariant. Remarkably, the lifetimes of quasiparticles on either orbit in the presence of intra- and interband scattering oscillate with both frequencies f_α and f_β. This situation is schematically depicted in Fig. 5.8 (c). We can express these oscillations in terms of a Dingle temperature as

$$\frac{1}{\tau_\alpha} \propto T_{\mathrm{D},\alpha} \propto T^0_{\mathrm{D},\alpha} + A_\alpha \cos\left(\frac{2\pi f_\alpha}{B}\right) + A_\beta \cos\left(\frac{2\pi f_\beta}{B}\right) \ , \tag{5.3}$$

where A_α and A_β are prefactors determined by the strength of intra- and interband scattering, respectively.

Intraband scattering may be induced by any defect in the crystal lattice, such as impurities, vacancies, or domain boundaries between areas with different chirality. The interband scattering in CoSi may be related to ferromagnetic impurities, whose presence has already been discussed in the description of the magnetic properties of our samples in Sec. 4.1.1. The Fermi surface around the R-point of CoSi exhibits a distinct spin texture, where the spin of orbit α (β) is antiparallel (parallel) to

its momentum [140, 223–225]. Points on the trajectories shown in Fig. 5.7 (b) that are close to each other in k-space consequently possess opposite spin orientations. Therefore, enhanced interband scattering is expected if the impurities break time-reversal symmetry and its influence is anticipated to be more pronounced.

In general, QOs of the QPL are relevant for all physical properties since they manifest themselves in an oscillating Dingle damping factor $\mathrm{R_D}(T_\mathrm{D})$. In the electrical conductivity σ, there is an additional linear dependence on T_D, which amplifies effects arising from lifetime oscillations. It can be expressed as

$$\sigma \propto T_\mathrm{D} \left[\cos\left(\frac{2\pi f_\alpha}{B}\right) + \cos\left(\frac{2\pi f_\beta}{B}\right) \right] \mathrm{R_D}(T_\mathrm{D}) \ , \tag{5.4}$$

where the term in square brackets describes the conventional quantum oscillations. If we insert the oscillatory Dingle temperature from Eq. (5.3) and ignore $\mathrm{R_D}(T_\mathrm{D})$ for the moment, we obtain terms of the form

$$\left[\cos\left(\frac{2\pi f_\alpha}{B}\right) \cdot \cos\left(\frac{2\pi f_\beta}{B}\right) \right] + \cos^2\left(\frac{2\pi f_{\alpha,\beta}}{B}\right) \tag{5.5}$$

in addition to the conventional QO frequencies. Using trigonometric identities the term in square brackets can be rewritten as

$$\frac{1}{2}\left[\cos\left(\frac{2\pi(f_\beta - f_\alpha)}{B}\right) + \cos\left(\frac{2\pi(f_\alpha + f_\beta)}{B}\right) \right] + \cos^2\left(\frac{2\pi f_{\alpha,\beta}}{B}\right) \ , \tag{5.6}$$

explaining the combination frequencies observed in experiment. Moreover, the fixed phase relationship between the fundamental QO frequencies and the difference frequency $f_{\beta-\alpha}$, illustrated in Figures 5.4 and 5.5, is consistent with this derivation.

The $\cos^2$ term in Eq. (5.6) arises purely from intraband scattering and, as mentioned above, only alters the harmonic content of the conventional QO frequencies. Further combination frequencies, such as $2f_\alpha - f_\beta$, $2f_\beta - f_\alpha$, $2(f_\beta - f_\alpha)$, $3f_\alpha - f_\beta$, $3f_\beta - f_\alpha$ and so on, are obtained if we additionally consider the oscillatory nature of $\mathrm{R_D}(T_\mathrm{D})$. However, their amplitudes are expected to be weaker than that of $f_{\beta-\alpha}$ and $f_{\alpha+\beta}$, rendering their experimental detection challenging.

5.3.3 Temperature dependence

Next, we discuss the effects of finite temperature on the oscillation amplitudes of frequencies arising from QPL oscillations. We begin by recapitulating how a

finite temperature is taken into account in the LK formalism. At $T > 0$, the sharp transition between occupied an unoccupied states is smeared out in a region $k_{\mathrm{B}}T$ around the Fermi level, as illustrated in the upper panel of Fig. 5.9. Conventional quantum oscillation frequencies are determined by the area A_k of extremal orbits on the Fermi surface that varies as a function of the chemical potential μ. The smeared-out Fermi surface can be described by an averaging over extremal orbits at different energies weighted by the negative derivative of the Fermi-Dirac distribution $-n_{\mathrm{FD}}(E)/\mathrm{d}E$. If there is a large frequency variation δf in an area $k_{\mathrm{B}}T$ around the Fermi energy, the quantum oscillations are strongly suppressed by temperature. This suppression directly scales with the cyclotron mass $m^* = \hbar^2/(2\pi)\partial A_k/\partial E$ through the temperature damping factor.

The same rationale applies to the combination frequencies $f_{\beta-\alpha}$ and $f_{\alpha+\beta}$, despite not having an extremal FS cross section associated with them. Nevertheless, their frequencies vary as a function of the chemical potential due to changes in the underlying frequencies f_α and f_β. We evaluate their frequency variation around the Fermi energy for our minimal model and find effective masses of

$$m^*_{\beta-\alpha} = \frac{\hbar^2}{2\pi}\frac{\partial(A_{k,\beta} - A_{k,\alpha})}{\partial E} = m^*_\beta - m^*_\alpha \tag{5.7}$$

and

$$m^*_{\alpha+\beta} = \frac{\hbar^2}{2\pi}\frac{\partial(A_{k,\alpha} + A_{k,\beta})}{\partial E} = m^*_\alpha + m^*_\beta \ . \tag{5.8}$$

The damping of difference frequency oscillations is expected to follow a temperature reduction factor $\mathrm{R_T}$ involving the difference of the cyclotron masses of the underlying frequencies. This agrees well with the experimental observations and explains the persistence of the difference frequency at notably higher temperatures than its constituent frequencies. It also serves as an experimental signature distinguishing QO frequencies from QPL oscillations from combination frequencies associated with other mechanisms like magnetic breakdown or magnetic interaction. In contrast, the damping of sum frequency oscillations is anticipated to follow a temperature reduction factor involving the sum of the cyclotron masses of f_α and f_β. This theoretical prediction matches our experimental findings but renders it more challenging to distinguish it from oscillations frequencies arising from conventional mechanisms which scale with a similar effective mass.

In our experimental evaluation of the oscillation amplitudes, we observed an additional contribution to the amplitude of difference frequency oscillations at low

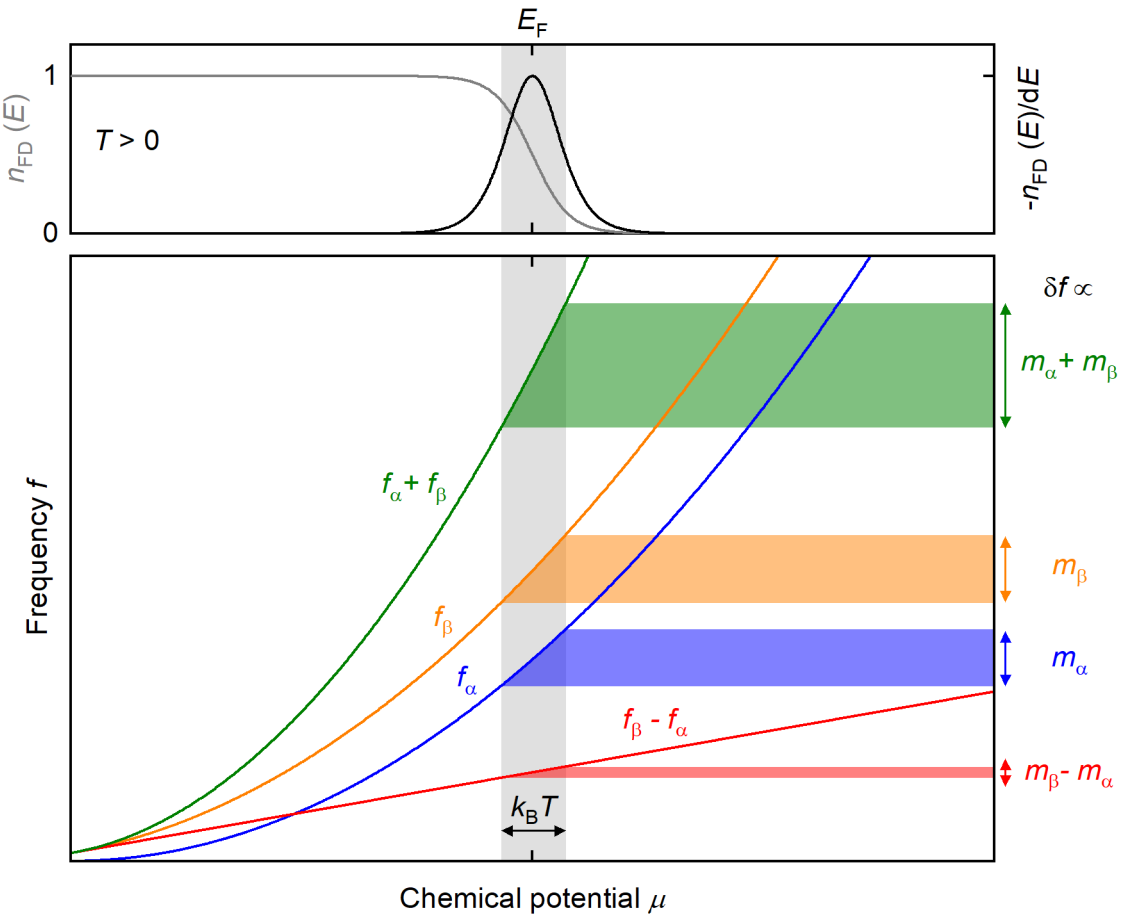

Figure 5.9: Temperature dependence of the QPL oscillations. At finite temperatures the Fermi-Dirac distribution n_{FD} smears out the transition between occupied and unoccupied states in an interval $k_{\mathrm{B}}T$ around the Fermi energy E_{F}. The fundamental QO frequencies f_α and f_β are associated with extremal cross-sectional areas on the Fermi surface A_k and depend on the location of the Fermi level. Consequently, the combination frequencies $f_{\beta-\alpha}$ and $f_{\alpha+\beta}$ also vary as a function of E_{F}. The damping of QO amplitudes is described by an averaging of QO frequencies over different values of E_{F} weighted by $-\mathrm{d}n_{\mathrm{FD}}/\mathrm{d}E$. The frequency variation δf in an interval $k_{\mathrm{B}}T$ around the Fermi level is proportional to the cyclotron mass m in the LK temperature reduction factor $\mathrm{R_T}$. The almost parallel dispersion of frequencies f_α and f_β leads to a nearly complete suppression of the dispersion of $f_{\beta-\alpha}$ explaining its remarkable temperature stability.

temperatures beyond a simple $\mathrm{R_T}(m^*_\beta - m^*_\beta)$ behavior. In the magnetoresistance, shown in Fig. 5.4 (c), a slight decline in oscillation amplitudes is noticeable at temperatures below 5 K. The deviation is even more pronounced in the Hall resistivity, shown in Fig. 5.5 (c), for which a clear increase in oscillation amplitudes towards lower temperatures is detected below 2 K. The origin of these additional contributions is currently not fully understood and will be an interesting topic for further studies. Potential explanations may involve further coupling mechanisms, such as

Coulomb repulsion, which has recently been proposed to influence QO frequencies in quasi-two-dimensional systems [226].

5.3.4 Generality

The only precondition for QO of the QPL giving rise to combination frequencies is some form of non-linear coupling between two extremal FS orbits. Possible mechanisms underlying this coupling include impurity scattering, electron-electron interaction, scattering on stochiometric or structural defects, or collective excitations. As mentioned above, the effect we describe is well known in two-dimensional materials [214–221, 227]. Given its rather simple preconditions, it is surprising that its relevance has not been appreciated for three-dimensional materials so far. Combination frequencies exhibiting characteristics consistent with expectations from QPL oscillations have been detected in three-dimensional materials already [160, 175, 228, 229], but not been described as such. We summarize the observations of these studies briefly in the following.

In Refs. [160, 175] the authors report on SdH oscillations in the topological nodal-line semimetals HfSiS and ZrSiS. There are two conventional oscillation frequencies observed, which are attributed to a hole- and an electron-like pocket. Additionally, the sum and the difference of these frequencies is detected. The authors explicitly note that the sum frequency is semi-classically forbidden. In HfSiS the temperature dependence of the sum frequency was analyzed and it exhibits a weak temperature dependent damping involving an effective mass roughly equal to the difference of the masses of the underlying frequencies. In ZrSiS the sum frequency is detected in transport measurements but visibly absent in the dHvA spectra. The existence and behavior of the sum frequency is consistent with its origins in QOs of the QPL coupling the electron and hole orbits in these materials.

Ref. [228] reports on SdH oscillations in the kagome semimetal $Co_3Sn_2S_2$ featuring multiple hole- and electron-like FS pockets. Again, a sum frequency is observed, although the underlying frequencies are attributed to a hole and an electron orbit. The authors explicitly mention that magnetic breakdown can only explain a difference frequency. At 20 K the sum frequency becomes the dominant contribution to the spectrum, suggesting a larger temperature stability than its underlying frequencies. The temperature stable sum frequency might be explained by a coupling of the hole and electron orbits.

In Ref. [229] the authors report on SdH oscillations in the topological semimetals $MoSi_2$ and WSi_2. Both materials feature an elongated hole pocket around the Γ-point. The warping of this pocket leads to a minimal and two maximal orbits giving rise to two oscillations frequencies. Additionally, a pronounced difference frequency with an amplitude amounting to about 10 % of the fundamental frequencies in $MoSi_2$ and 20 % in WSi_2 is detected. In contrast to the underlying frequencies, it is observed up to 25 K with only little reduction in oscillation amplitude. The authors attribute the difference frequency to magnetic interaction, but note that MI is typically observed only at much lower temperatures. Interestingly, here the difference frequency arises from two orbits on the same Fermi surface pocket, suggesting that interorbit coupling on the same band may give rise to it. The observed behavior of the difference frequency is highly suggestive of QOs of the QPL as its underlying mechanism.

In studies on the iron-based superconductors $FeSe_{1-x}S_x$ [125, 230] a small oscillation frequency with light effective mass emerges below the transition to a nematic phase. The Fermi surface in the tetragonal phase does not feature an orbit that could explain this small frequency. The authors therefore propose, that the Fermi surface gets reconstructed upon entering the nematic phase and a new Fermi surface pocket emerges through a Lifshitz transition. Interband scattering between FS trajectories, which are degenerate in the tetragonal phase, but split up in the nematic phase, might provide an alternate explanation [231]. Our findings motivate to revisit these studies to assess whether the spectra can be reconciled without the need to invoke a Lifshitz transition.

5.4 Summary and outlook

In summary, we report on combination frequencies in the Shubnikov-de Haas spectra of CoSi, which do not correspond to semi-classical quasiparticle trajectories via the Onsager relation. The existence and unusual temperature dependence of the difference frequency is in contrast to conventional mechanisms known to give rise to combination frequencies. We show that our findings are in good agreement with quantum oscillations of the quasiparticle lifetime in the presence of finite interband coupling. The simple preconditions for the proposed mechanism and the existence of unexplained QO frequencies with a strikingly similar behavior reported in the literature indicates that lifetime oscillations may play a role in many material systems.

Given that the combination frequencies arising from QPL oscillations originate in a coupling between different FS orbits, their amplitudes may provide insights into the strength of the underlying coupling mechanisms. In fact, a recent study on twisted bilayer graphene [227] used interminivalley oscillations, which are a two-dimensional analog of the mechanism we propose, to determine the electron-electron scattering rate. The observation of QPL oscillations in CoSi and their putative existence in further three-dimensional materials suggests the possibility of using them to study the coupling between different parts of the Fermi surface in a wide range of systems.

Further studies on CoSi that have already been started in our group aim at an understanding of the additional contribution to the SdH amplitude of the difference frequency at very low temperatures and the different characteristics of this contribution in the longitudinal and Hall resistivity. Moreover, the proposed coupling mechanism in CoSi through interband scattering mediated by time-reversal breaking impurities suggests that there should be a dependence of the coupling strength on the impurity concentration. A different coupling strength should manifest itself in the amplitudes of the detected combination frequencies. A systematic study on samples with different defect concentrations has been started. It is, however, challenging to precisely determine and control the impurity concentration at the very low levels needed to observe quantum oscillations in the first place.

We also synthesized single crystals of $MoSi_2$ and WSi_2 in our group to study the difference frequency detected in their SdH spectra. First results on $MoSi_2$ show the temperature stable difference frequency along with its higher harmonics and further combination frequencies. The temperature dependence of the difference frequency oscillations features additional contributions both at low and high temperatures,

which are not fully understood up to date. The large quantum oscillation amplitudes in $MoSi_2$ and the pronounced difference frequency contribution allow for a detailed experimental investigation of their characteristics and might provide further insight in the underlying mechanism.

Part of the work presented in this chapter has been published in Ref. [232]. A detailed derivation of the theory can be found in Ref. [233]. Preliminary measurements have been performed as part of a preceding Master's thesis [188].

6 Conclusion

In this thesis, we investigated the chiral topological semimetal CoSi. We probed its electronic structure through quantum oscillations in the resistivity and magnetization and compared our findings with ab-initio band structure calculations. We collaborated with theory colleagues to establish a link between the experimental observations and the global band topology of CoSi and explain the existence of combination frequencies in the Shubnikov-de Haas spectra through oscillations of the quasiparticle lifetime.

In Chapter 4, we presented an overview of the magnetic and magnetotransport properties of CoSi confirming its semimetallic character. Two dominant quantum oscillation frequencies with almost no angular dispersion have been detected in the longitudinal and Hall resistivity as well as the magnetization. This part of the quantum oscillation spectrum has been linked to electron-like Fermi surface pockets centered around the R-point of CoSi. We provided a comprehensive explanation of this surprisingly simple spectrum via the combined effect of symmetry-enforced degeneracies on the Brillouin zone boundary, a spin-orbit coupling induced splitting of the bands, and complete magnetic breakdown at near-degeneracies in the interior of the BZ. We presented further measurements on samples with improved crystalline quality. Their quantum oscillation spectra feature additional frequencies with larger cyclotron masses. We elucidated the origin of these oscillation frequencies by demonstrating that they correspond to extremal Fermi surface trajectories situated in proximity to the Γ-point of CoSi. Our analysis revealed that the ab-initio calculated band structure requires an empirical correction, which we implemented through the introduction of small rigid shifts of the bands with respect to the Fermi energy. We discussed our findings with respect to topological crossings in the band structure, which comprise multifold crossing points located at the R- and Γ-point, nodal planes on the BZ boundary, and Weyl nodes located throughout the BZ.

Chapter 5 was concerned with the observation of combination frequencies in the Shubnikov-de Haas spectra of CoSi. A difference and a sum frequency of the two dominant quantum oscillation frequencies arising from the FS around the R-point were identified. Their correspondence to combination frequencies was verified by detailed measurements of the angular dispersion and the fixed phase relation between the oscillations provided further evidence of their connection. We conducted an analysis of the temperature dependence of all frequency components and discovered a remarkably small temperature dependent damping of the difference frequency

oscillations, which was detectable up to a temperature of approximately 50 K, at which all other oscillation frequencies were completely suppressed. The temperature dependence could be described by a temperature reduction factor involving the difference of the cyclotron masses of the underlying frequencies, with additional contributions to its amplitude at very low temperatures. The sum frequency was only detectable below 1 K and could be described by a temperature damping factor involving the sum of the underlying cyclotron masses. The experimental findings were compared to conventional mechanisms that are known to produce combination frequencies in quantum oscillation spectra. None of the known mechanisms could explain the observed behavior, especially the small temperature-dependent damping of the difference frequency, consistently. We presented a novel mechanism that involves a coupling between different parts of the FS mediated by impurity scattering. This mechanism connects the lifetime of quasiparticles on one orbit to the oscillatory density of states from another orbit, thereby introducing a mixing of the oscillation frequencies. We discussed how the proposed mechanism naturally explains the temperature dependence of the combination frequencies and commented on its generality and putative observation in further materials.

Taken together, the work reported in this thesis provides a detailed picture of the Fermi surface of CoSi. It addresses several misinterpretations about the quantum oscillation spectrum arising from FS pockets centered around the R-point. Additionally, it discusses the relevance of topological crossings in the band structure beyond the multifold crossing points, which have been the focus of previous studies. The enhanced quality of the investigated samples permitted the observation of previously undetected oscillation frequencies arising from FS pockets around the Γ-point, thereby completing the experimental determination of the Fermi surface. The detected combination frequencies and their unconventional behavior led to the development of a theory that explains their existence through quantum oscillations of the quasiparticle lifetime in systems with a finite interorbit coupling. The proposed mechanism is expected to be of general relevance and might have already been observed unknowingly in further bulk materials. The detection of combination frequencies arising from quasiparticle lifetime oscillations might provide information about the coupling between different parts of the Fermi surface in a wide range of materials, thereby paving the way to gain a deeper understanding of the involved mechanisms and construct more accurate models of their electronic structure.

References

[1] G. Grüner, *The dynamics of charge-density waves,* Reviews of Modern Physics **60**, 1129 (1988).

[2] M. D. Johannes and I. I. Mazin, *Fermi surface nesting and the origin of charge density waves in metals,* Physical Review B **77**, 165135 (2008).

[3] N. P. Armitage, P. Fournier, and R. L. Greene, *Progress and perspectives on electron-doped cuprates,* Reviews of Modern Physics **82**, 2421 (2010).

[4] J. Paglione and R. L. Greene, *High-temperature superconductivity in iron-based materials,* Nature Physics **6**, 645 (2010).

[5] N. W. Ashcroft and N. D. Mermin, *Solid State Physics* (Holt, Rinehart and Winston, 1976).

[6] H. R. Philipp and H. Ehrenreich, *Optical Properties of Semiconductors,* Physical Review **129**, 1550 (1963).

[7] S. Nakamura and M. R. Krames, *History of Gallium–Nitride-Based Light-Emitting Diodes for Illumination,* Proceedings of the IEEE **101**, 2211 (2013).

[8] H. Jones and A. M. Tyndall, *The theory of the galvomagnetic effects in bismuth,* Proceedings of the Royal Society of London. Series A - Mathematical and Physical Sciences **155**, 653 (1936).

[9] B. R. A. Nijboer, *On the theory of electronic semiconductors,* Proceedings of the Physical Society **51**, 575 (1939).

[10] P. Hohenberg and W. Kohn, *Inhomogeneous Electron Gas,* Physical Review **136**, B864 (1964).

[11] M. V. Berry, *Quantal phase factors accompanying adiabatic changes,* Proceedings of the Royal Society of London. A. Mathematical and Physical Sciences **392**, 45 (1984).

[12] D. J. Thouless, M. Kohmoto, M. P. Nightingale, and M. den Nijs, *Quantized Hall Conductance in a Two-Dimensional Periodic Potential,* Physical Review Letters **49**, 405 (1982).

[13] M. Kohmoto, *Topological invariant and the quantization of the Hall conductance,* Annals of Physics **160**, 343 (1985).

[14] R. D. King-Smith and D. Vanderbilt, *Theory of polarization of crystalline solids,* Physical Review B **47**, 1651 (1993).

[15] J. Shi, G. Vignale, D. Xiao, and Q. Niu, *Quantum Theory of Orbital Magnetization and Its Generalization to Interacting Systems,* Physical Review Letters **99**, 197202 (2007).

[16] M.-C. Chang and Q. Niu, *Berry curvature, orbital moment, and effective quantum theory of electrons in electromagnetic fields,* Journal of Physics: Condensed Matter **20**, 193202 (2008).

[17] G. Chang, B. J. Wieder, F. Schindler, D. S. Sanchez, I. Belopolski, S.-M. Huang, B. Singh, D. Wu, T.-R. Chang, T. Neupert, S.-Y. Xu, H. Lin, and M. Z. Hasan, *Topological quantum properties of chiral crystals,* Nature Materials **17**, 978 (2018).

[18] N. P. Armitage, E. J. Mele, and A. Vishwanath, *Weyl and Dirac semimetals in three-dimensional solids,* Reviews of Modern Physics **90**, 015001 (2018).

[19] M. G. Vergniory, L. Elcoro, C. Felser, N. Regnault, B. A. Bernevig, and Z. Wang, *A complete catalogue of high-quality topological materials,* Nature **566**, 480 (2019).

[20] S.-S. Chern, *A Simple Intrinsic Proof of the Gauss-Bonnet Formula for Closed Riemannian Manifolds,* Annals of Mathematics **45**, 747 (1944), 1969302 .

[21] D. Xiao, M.-C. Chang, and Q. Niu, *Berry phase effects on electronic properties,* Reviews of Modern Physics **82**, 1959 (2010).

[22] C. L. Kane and E. J. Mele, *Z_2 topological Order and the Quantum Spin Hall Effect,* Physical Review Letters **95**, 146802 (2005).

[23] M. Z. Hasan and J. E. Moore, *Three-Dimensional Topological Insulators,* Annual Review of Condensed Matter Physics **2**, 55 (2011).

[24] M. König, S. Wiedmann, C. Brüne, A. Roth, H. Buhmann, L. W. Molenkamp, X.-L. Qi, and S.-C. Zhang, *Quantum Spin Hall Insulator State in HgTe Quantum Wells,* Science **318**, 766 (2007).

[25] D. Hsieh, D. Qian, L. Wray, Y. Xia, Y. S. Hor, R. J. Cava, and M. Z. Hasan, *A topological Dirac insulator in a quantum spin Hall phase,* Nature **452**, 970 (2008).

[26] H. Zhang, C.-X. Liu, X.-L. Qi, X. Dai, Z. Fang, and S.-C. Zhang, *Topological insulators in Bi_2Se_3, Bi_2Te_3 and Sb_2Te_3 with a single Dirac cone on the surface,* Nature Physics **5**, 438 (2009).

[27] C. Shekhar, S. Ouardi, A. K. Nayak, G. H. Fecher, W. Schnelle, and C. Felser, *Ultrahigh mobility and nonsaturating magnetoresistance in Heusler topological insulators,* Physical Review B **86**, 155314 (2012).

[28] X. Wan, A. M. Turner, A. Vishwanath, and S. Y. Savrasov, *Topological semimetal and Fermi-arc surface states in the electronic structure of pyrochlore iridates,* Physical Review B **83**, 205101 (2011).

[29] A. A. Burkov, M. D. Hook, and L. Balents, *Topological nodal semimetals,* Physical Review B **84**, 235126 (2011).

[30] S. M. Young, S. Zaheer, J. C. Y. Teo, C. L. Kane, E. J. Mele, and A. M. Rappe, *Dirac Semimetal in Three Dimensions,* Physical Review Letters **108**, 140405 (2012).

[31] Z. Wang, Y. Sun, X.-Q. Chen, C. Franchini, G. Xu, H. Weng, X. Dai, and Z. Fang, *Dirac semimetal and topological phase transitions in A_3Bi ($A = Na, K, Rb$),* Physical Review B **85**, 195320 (2012).

[32] H. Weng, C. Fang, Z. Fang, B. A. Bernevig, and X. Dai, *Weyl Semimetal Phase in Noncentrosymmetric Transition-Metal Monophosphides,* Physical Review X **5**, 011029 (2015).

[33] S.-Y. Xu, I. Belopolski, N. Alidoust, M. Neupane, G. Bian, C. Zhang, R. Sankar, G. Chang, Z. Yuan, C.-C. Lee, S.-M. Huang, H. Zheng, J. Ma, D. S. Sanchez, B. Wang, A. Bansil, F. Chou, P. P. Shibayev, H. Lin, S. Jia, and M. Z. Hasan, *Discovery of a Weyl fermion semimetal and topological Fermi arcs,* Science **349**, 613 (2015).

[34] B. Q. Lv, H. M. Weng, B. B. Fu, X. P. Wang, H. Miao, J. Ma, P. Richard, X. C. Huang, L. X. Zhao, G. F. Chen, Z. Fang, X. Dai, T. Qian, and H. Ding, *Experimental Discovery of Weyl Semimetal TaAs,* Physical Review X **5**, 031013 (2015).

[35] Z. K. Liu, B. Zhou, Y. Zhang, Z. J. Wang, H. M. Weng, D. Prabhakaran, S.-K. Mo, Z. X. Shen, Z. Fang, X. Dai, Z. Hussain, and Y. L. Chen, *Discovery of a Three-Dimensional Topological Dirac Semimetal, Na_3Bi,* Science **343**, 864 (2014).

[36] H. Kramers, *Théorie générale de la rotation paramagnétique dans les cristaux,* Proceedings of the Royal Academy of Sciences at Amsterdam **33**, 959 (1930).

[37] L. Balents, *Weyl electrons kiss,* Physics **4**, 36 (2011).

[38] S.-Y. Xu, C. Liu, S. K. Kushwaha, R. Sankar, J. W. Krizan, I. Belopolski, M. Neupane, G. Bian, N. Alidoust, T.-R. Chang, H.-T. Jeng, C.-Y. Huang, W.-F. Tsai, H. Lin, P. P. Shibayev, F.-C. Chou, R. J. Cava, and M. Z. Hasan, *Observation of Fermi arc surface states in a topological metal,* Science **347**, 294 (2015).

[39] L. Isaev, Y. H. Moon, and G. Ortiz, *Bulk-boundary correspondence in three-dimensional topological insulators,* Physical Review B **84**, 075444 (2011).

[40] A. M. Essin and V. Gurarie, *Bulk-boundary correspondence of topological insulators from their respective Green's functions,* Physical Review B **84**, 125132 (2011).

[41] H. B. Nielsen and M. Ninomiya, *The Adler-Bell-Jackiw anomaly and Weyl fermions in a crystal,* Physics Letters B **130**, 389 (1983).

[42] A. A. Zyuzin and A. A. Burkov, *Topological response in Weyl semimetals and the chiral anomaly,* Physical Review B **86**, 115133 (2012).

[43] X. Huang, L. Zhao, Y. Long, P. Wang, D. Chen, Z. Yang, H. Liang, M. Xue, H. Weng, Z. Fang, X. Dai, and G. Chen, *Observation of the Chiral-Anomaly-Induced Negative Magnetoresistance in 3D Weyl Semimetal TaAs,* Physical Review X **5**, 031023 (2015).

[44] C.-L. Zhang, S.-Y. Xu, I. Belopolski, Z. Yuan, Z. Lin, B. Tong, G. Bian, N. Alidoust, C.-C. Lee, S.-M. Huang, T.-R. Chang, G. Chang, C.-H. Hsu, H.-T. Jeng, M. Neupane, D. S. Sanchez, H. Zheng, J. Wang, H. Lin, C. Zhang, H.-Z. Lu, S.-Q. Shen, T. Neupert, M. Zahid Hasan, and S. Jia, *Signatures of the Adler–Bell–Jackiw chiral anomaly in a Weyl fermion semimetal,* Nature Communications **7**, 10735 (2016).

[45] Y. Li, Z. Wang, P. Li, X. Yang, Z. Shen, F. Sheng, X. Li, Y. Lu, Y. Zheng, and Z.-A. Xu, *Negative magnetoresistance in Weyl semimetals NbAs and NbP: Intrinsic chiral anomaly and extrinsic effects,* Frontiers of Physics **12**, 127205 (2017).

[46] P. Hosur, S. A. Parameswaran, and A. Vishwanath, *Charge Transport in Weyl Semimetals,* Physical Review Letters **108**, 046602 (2012).

[47] P. E. C. Ashby and J. P. Carbotte, *Magneto-optical conductivity of Weyl semimetals,* Physical Review B **87**, 245131 (2013).

[48] C. J. Tabert, J. P. Carbotte, and E. J. Nicol, *Optical and transport properties in three-dimensional Dirac and Weyl semimetals,* Physical Review B **93**, 085426 (2016).

[49] C.-K. Chan, N. H. Lindner, G. Refael, and P. A. Lee, *Photocurrents in Weyl semimetals,* Physical Review B **95**, 041104 (2017).

[50] F. de Juan, A. G. Grushin, T. Morimoto, and J. E. Moore, *Quantized circular photogalvanic effect in Weyl semimetals,* Nature Communications **8**, 15995 (2017).

[51] Q. Ma, S.-Y. Xu, C.-K. Chan, C.-L. Zhang, G. Chang, Y. Lin, W. Xie, T. Palacios, H. Lin, S. Jia, P. A. Lee, P. Jarillo-Herrero, and N. Gedik, *Direct optical detection of Weyl fermion chirality in a topological semimetal,* Nature Physics **13**, 842 (2017).

[52] Z. Fang, N. Nagaosa, K. S. Takahashi, A. Asamitsu, R. Mathieu, T. Ogasawara, H. Yamada, M. Kawasaki, Y. Tokura, and K. Terakura, *The Anomalous Hall Effect and Magnetic Monopoles in Momentum Space,* Science **302**, 92 (2003).

[53] G. Xu, H. Weng, Z. Wang, X. Dai, and Z. Fang, *Chern Semimetal and the Quantized Anomalous Hall Effect in $HgCr_2Se_4$,* Physical Review Letters **107**, 186806 (2011).

[54] K.-Y. Yang, Y.-M. Lu, and Y. Ran, *Quantum Hall effects in a Weyl semimetal: Possible application in pyrochlore iridates,* Physical Review B **84**, 075129 (2011).

[55] Y. Sun, Y. Zhang, C. Felser, and B. Yan, *Strong Intrinsic Spin Hall Effect in the TaAs Family of Weyl Semimetals,* Physical Review Letters **117**, 146403 (2016).

[56] L. P. He, X. C. Hong, J. K. Dong, J. Pan, Z. Zhang, J. Zhang, and S. Y. Li, *Quantum Transport Evidence for the Three-Dimensional Dirac Semimetal Phase in Cd_3As_2,* Physical Review Letters **113**, 246402 (2014).

[57] J. Cao, S. Liang, C. Zhang, Y. Liu, J. Huang, Z. Jin, Z.-G. Chen, Z. Wang, Q. Wang, J. Zhao, S. Li, X. Dai, J. Zou, Z. Xia, L. Li, and F. Xiu, *Landau level splitting in Cd_3As_2 under high magnetic fields,* Nature Communications **6**, 7779 (2015).

[58] Y. Zhao, H. Liu, C. Zhang, H. Wang, J. Wang, Z. Lin, Y. Xing, H. Lu, J. Liu, Y. Wang, S. M. Brombosz, Z. Xiao, S. Jia, X. C. Xie, and J. Wang, *Anisotropic Fermi Surface and Quantum Limit Transport in High Mobility Three-Dimensional Dirac Semimetal Cd_3As_2,* Physical Review X **5**, 031037 (2015).

[59] H. Pan, K. Zhang, Z. Wei, B. Zhao, J. Wang, M. Gao, L. Pi, M. Han, F. Song, X. Wang, B. Wang, and R. Zhang, *Quantum oscillation and nontrivial transport in the Dirac semimetal Cd_3As_2 nanodevice,* Applied Physics Letters **108**, 183103 (2016).

[60] B. Bradlyn, J. Cano, Z. Wang, M. G. Vergniory, C. Felser, R. J. Cava, and B. A. Bernevig, *Beyond Dirac and Weyl fermions: Unconventional quasiparticles in conventional crystals,* Science **353**, aaf5037 (2016).

[61] B. J. Wieder, Y. Kim, A. M. Rappe, and C. L. Kane, *Double Dirac Semimetals in Three Dimensions,* Physical Review Letters **116**, 186402 (2016).

[62] B. Bradlyn, L. Elcoro, J. Cano, M. G. Vergniory, Z. Wang, C. Felser, M. I. Aroyo, and B. A. Bernevig, *Topological quantum chemistry,* Nature **547**, 298 (2017).

[63] F. Flicker, F. de Juan, B. Bradlyn, T. Morimoto, M. G. Vergniory, and A. G. Grushin, *Chiral optical response of multifold fermions,* Physical Review B **98**, 155145 (2018).

[64] T. Zhang, Y. Jiang, Z. Song, H. Huang, Y. He, Z. Fang, H. Weng, and C. Fang, *Catalogue of topological electronic materials,* Nature **566**, 475 (2019).

[65] S. Nie, B. A. Bernevig, and Z. Wang, *Sixfold excitations in electrides,* Physical Review Research **3**, L012028 (2021).

[66] L. Jin, *Spin-polarized sextuple excitations in ferromagnetic materials,* Physical Review B **105** (2022), 10.1103/PhysRevB.105.245141.

[67] Y. Shen, Y. Jin, Y. Ge, M. Chen, and Z. Zhu, *Chiral topological metals with multiple types of quasiparticle fermions and large spin Hall effect in the SrGePt family materials,* Physical Review B **108**, 035428 (2023).

[68] B. Q. Lv, Z.-L. Feng, Q.-N. Xu, X. Gao, J.-Z. Ma, L.-Y. Kong, P. Richard, Y.-B. Huang, V. N. Strocov, C. Fang, H.-M. Weng, Y.-G. Shi, T. Qian, and H. Ding, *Observation of three-component fermions in the topological semimetal molybdenum phosphide,* Nature **546**, 627 (2017).

[69] J.-Z. Ma, J.-B. He, Y.-F. Xu, B. Q. Lv, D. Chen, W.-L. Zhu, S. Zhang, L.-Y. Kong, X. Gao, L.-Y. Rong, Y.-B. Huang, P. Richard, C.-Y. Xi, E. S. Choi, Y. Shao, Y.-L. Wang, H.-J. Gao, X. Dai, C. Fang, H.-M. Weng, G.-F. Chen, T. Qian, and H. Ding, *Three-component fermions with surface Fermi arcs in tungsten carbide,* Nature Physics **14**, 349 (2018).

[70] B.-B. Fu, C.-J. Yi, T.-T. Zhang, M. Caputo, J.-Z. Ma, X. Gao, B. Q. Lv, L.-Y. Kong, Y.-B. Huang, P. Richard, M. Shi, V. N. Strocov, C. Fang, H.-M. Weng, Y.-G. Shi, T. Qian, and H. Ding, *Dirac nodal surfaces and nodal lines in ZrSiS,* Science Advances **5**, eaau6459 (2019).

[71] N. Kumar, M. Yao, J. Nayak, M. G. Vergniory, J. Bannies, Z. Wang, N. B. M. Schröter, V. N. Strocov, L. Müchler, W. Shi, E. D. L. Rienks, J. L. Mañes, C. Shekhar, S. S. P. Parkin, J. Fink, G. H. Fecher, Y. Sun, B. A. Bernevig, and C. Felser, *Signatures of Sixfold Degenerate Exotic Fermions in a Superconducting Metal $PdSb_2$,* Advanced Materials **32**, 1906046 (2020).

[72] S. Thirupathaiah, Y. S. Kushnirenk, K. Koepernik, B. R. Piening, B. Büchner, S. Aswartham, J. van den Brink, S. Borisenko, and I. C. Fulga, *Sixfold fermion near the Fermi level in cubic $PtBi_2$,* SciPost Physics **10**, 004 (2021).

[73] P. Tang, Q. Zhou, and S.-C. Zhang, *Multiple Types of Topological Fermions in Transition Metal Silicides,* Physical Review Letters **119**, 206402 (2017).

[74] G. Chang, S.-Y. Xu, B. J. Wieder, D. S. Sanchez, S.-M. Huang, I. Belopolski, T.-R. Chang, S. Zhang, A. Bansil, H. Lin, and M. Z. Hasan, *Unconventional chiral fermions and large topological fermi arcs in RhSi,* Physical Review Letters **119**, 206401 (2017).

[75] D. A. Pshenay-Severin, Y. V. Ivanov, A. A. Burkov, and A. T. Burkov, *Band structure and unconventional electronic topology of CoSi,* Journal of Physics: Condensed Matter **30**, 135501 (2018).

[76] T. Zhang, Z. Song, A. Alexandradinata, H. Weng, C. Fang, L. Lu, and Z. Fang, *Double-Weyl Phonons in Transition-Metal Monosilicides,* Physical Review Letters **120**, 016401 (2018).

[77] Z. Li, T. Iitaka, H. Zeng, and H. Su, *Optical response of the chiral topological semimetal RhSi,* Physical Review B **100**, 155201 (2019).

[78] N. B. M. Schröter, D. Pei, M. G. Vergniory, Y. Sun, K. Manna, F. de Juan, J. A. Krieger, V. Süss, M. Schmidt, P. Dudin, B. Bradlyn, T. K. Kim, T. Schmitt, C. Cacho, C. Felser, V. N. Strocov, and Y. Chen, *Chiral topological semimetal with multifold band crossings and long Fermi arcs,* Nature Physics **15**, 759 (2019).

[79] Z. Rao, H. Li, T. Zhang, S. Tian, C. Li, B. Fu, C. Tang, L. Wang, Z. Li, W. Fan, J. Li, Y. Huang, Z. Liu, Y. Long, C. Fang, H. Weng, Y. Shi, H. Lei, Y. Sun, T. Qian, and H. Ding, *Observation of unconventional chiral fermions with long Fermi arcs in CoSi,* Nature **567**, 496 (2019).

[80] D. S. Sanchez, I. Belopolski, T. A. Cochran, X. Xu, J.-X. Yin, G. Chang, W. Xie, K. Manna, V. Süß, C.-Y. Huang, N. Alidoust, D. Multer, S. S. Zhang, N. Shumiya, X. Wang, G.-Q. Wang, T.-R. Chang, C. Felser, S.-Y. Xu, S. Jia, H. Lin, and M. Z. Hasan, *Topological chiral crystals with helicoid-arc quantum states,* Nature **567**, 500 (2019).

[81] D. Takane, Z. Wang, S. Souma, K. Nakayama, T. Nakamura, H. Oinuma, Y. Nakata, H. Iwasawa, C. Cacho, T. Kim, K. Horiba, H. Kumigashira, T. Takahashi, Y. Ando, and T. Sato, *Observation of chiral fermions with a large topological charge and associated fermi-arc surface states in CoSi,* Physical Review Letters **122**, 076402 (2019).

[82] B. Xu, Z. Fang, M.-Á. Sánchez-Martínez, J. W. F. Venderbos, Z. Ni, T. Qiu, K. Manna, K. Wang, J. Paglione, C. Bernhard, C. Felser, E. J. Mele, A. G. Grushin, A. M. Rappe, and L. Wu, *Optical signatures of multifold fermions in the chiral topological semimetal CoSi,* Proceedings of the National Academy of Sciences **117**, 27104 (2020).

[83] D. Rees, K. Manna, B. Lu, T. Morimoto, H. Borrmann, C. Felser, J. E. Moore, D. H. Torchinsky, and J. Orenstein, *Helicity-dependent photocurrents in the chiral Weyl semimetal RhSi,* Science Advances **6**, eaba0509 (2020).

[84] P. Sessi, F.-R. Fan, F. Küster, K. Manna, N. B. M. Schröter, J.-R. Ji, S. Stolz, J. A. Krieger, D. Pei, T. K. Kim, P. Dudin, C. Cacho, R. Widmer, H. Borrmann, W. Shi, K. Chang, Y. Sun, C. Felser, and S. S. P. Parkin, *Handedness-dependent quasiparticle interference in the two enantiomers of the topological chiral semimetal PdGa,* Nature Communications **11**, 3507 (2020).

[85] M. Yao, K. Manna, Q. Yang, A. Fedorov, V. Voroshnin, B. Valentin Schwarze, J. Hornung, S. Chattopadhyay, Z. Sun, S. N. Guin, J. Wosnitza, H. Borrmann, C. Shekhar, N. Kumar, J. Fink, Y. Sun, and C. Felser, *Observation of giant spin-split Fermi-arc with maximal Chern number in the chiral topological semimetal PtGa,* Nature Communications **11**, 2033 (2020).

[86] L. Z. Maulana, K. Manna, E. Uykur, C. Felser, M. Dressel, and A. V. Pronin, *Optical conductivity of multifold fermions: The case of RhSi,* Physical Review Research **2**, 023018 (2020).

[87] Z. Ni, B. Xu, M.-Á. Sánchez-Martínez, Y. Zhang, K. Manna, C. Bernhard, J. W. F. Venderbos, F. de Juan, C. Felser, A. G. Grushin, and L. Wu, *Linear and nonlinear optical responses in the chiral multifold semimetal RhSi,* npj Quantum Materials **5**, 1 (2020).

[88] N. B. M. Schröter, S. Stolz, K. Manna, F. de Juan, M. G. Vergniory, J. A. Krieger, D. Pei, T. Schmitt, P. Dudin, T. K. Kim, C. Cacho, B. Bradlyn, H. Borrmann, M. Schmidt, R. Widmer, V. N. Strocov, and C. Felser, *Observation and control of maximal Chern numbers in a chiral topological semimetal,* Science **369**, 179 (2020).

[89] D. Rees, B. Lu, Y. Sun, K. Manna, R. Özgür, S. Subedi, H. Borrmann, C. Felser, J. Orenstein, and D. H. Torchinsky, *Direct Measurement of Helicoid Surface States in RhSi Using Nonlinear Optics,* Physical Review Letters **127**, 157405 (2021).

[90] Z. Ni, K. Wang, Y. Zhang, O. Pozo, B. Xu, X. Han, K. Manna, J. Paglione, C. Felser, A. G. Grushin, F. de Juan, E. J. Mele, and L. Wu, *Giant topological longitudinal circular photo-galvanic effect in the chiral multifold semimetal CoSi,* Nature Communications **12**, 154 (2021).

[91] J.-Z. Ma, S.-N. Zhang, J. P. Song, Q.-S. Wu, S. A. Ekahana, M. Naamneh, M. Radovic, V. N. Strocov, S.-Y. Gao, T. Qian, H. Ding, K. He, K. Manna, C. Felser, N. C. Plumb, O. V. Yazyev, Y.-M. Xiong, and M. Shi, *Giant Chern number of a Weyl nodal surface without upper limit,* Physical Review B **105**, 115118 (2022).

[92] Z. Rao, Q. Hu, S. Tian, Q. Qu, C. Chen, S. Gao, Z. Yuan, C. Tang, W. Fan, J. Huang, Y. Huang, L. Wang, L. Zhang, F. Li, K. Wang, H. Yang, H. Weng, T. Qian, J. Xu, K. Jiang, H. Lei, Y.-J. Sun, and H. Ding, *Charge instability of topological Fermi arcs in chiral crystal CoSi,* Science Bulletin **68**, 165 (2023).

[93] O. Schob and E. Parthé, *The structure of HfSn,* Acta Crystallographica **17**, 452 (1964).

[94] A. Furusaki, *Weyl points and Dirac lines protected by multiple screw rotations,* Science Bulletin **62**, 788 (2017).

[95] W. Wu, Y. Liu, S. Li, C. Zhong, Z.-M. Yu, X.-L. Sheng, Y. X. Zhao, and S. A. Yang, *Nodal surface semimetals: Theory and material realization,* Physical Review B **97**, 115125 (2018).

[96] H. B. Nielsen and M. Ninomiya, *Absence of neutrinos on a lattice: (I). Proof by homotopy theory,* Nuclear Physics B **185**, 20 (1981).

[97] H. B. Nielsen and M. Ninomiya, *Absence of neutrinos on a lattice: (II). Intuitive topological proof,* Nuclear Physics B **193**, 173 (1981).

[98] H. Nielsen and M. Ninomiya, *A no-go theorem for regularizing chiral fermions,* Physics Letters B **105**, 219 (1981).

[99] Z.-M. Yu, W. Wu, Y. X. Zhao, and S. A. Yang, *Circumventing the no-go theorem: A single Weyl point without surface Fermi arcs,* Physical Review B **100**, 041118 (2019).

[100] M. A. Wilde, M. Dodenhöft, A. Niedermayr, A. Bauer, M. M. Hirschmann, K. Alpin, A. P. Schnyder, and C. Pfleiderer, *Symmetry-enforced topological nodal planes at the Fermi surface of a chiral magnet,* Nature **594**, 374 (2021).

[101] W. de Haas and P. van Alphen, *The dependence of the susceptibility of diamagnetic metals upon the field,* Proc. Netherlands Roy. Acad. Sci **33**, 170 (1930).

[102] L. Schubnikow and W. J. De Haas, *A New Phenomenon in the Change of Resistance in a Magnetic Field of Single Crystals of Bismuth,* Nature **126**, 500 (1930).

[103] L. S. Lerner, *Shubnikov-de Haas Effect in Bismuth,* Physical Review **127**, 1480 (1962).

[104] H. P. R. Frederikse, W. R. Hosler, W. R. Thurber, J. Babiskin, and P. G. Siebenmann, *Shubnikov—de Haas Effect in $SrTiO_3$,* Physical Review **158**, 775 (1967).

[105] L. L. Chang, H. Sakaki, C. A. Chang, and L. Esaki, *Shubnikov—de Haas Oscillations in a Semiconductor Superlattice,* Physical Review Letters **38**, 1489 (1977).

[106] E. Mun, S. L. Bud'ko, Y. Lee, C. Martin, M. A. Tanatar, R. Prozorov, and P. C. Canfield, *Quantum oscillations in the heavy-fermion compound YbPtBi,* Physical Review B **92**, 085135 (2015).

[107] N. P. Breznay, I. M. Hayes, B. J. Ramshaw, R. D. McDonald, Y. Krockenberger, A. Ikeda, H. Irie, H. Yamamoto, and J. G. Analytis, *Shubnikov-de Haas quantum oscillations reveal a reconstructed Fermi surface near optimal doping in a thin film of the cuprate superconductor $Pr_{1.86}Ce_{0.14}CuO_{4\pm\delta}$,* Physical Review B **94**, 104514 (2016).

[108] P. F. Sullivan and G. Seidel, *Steady-State, ac-Temperature Calorimetry,* Physical Review **173**, 679 (1968).

[109] N. A. Fortune, J. S. Brooks, M. J. Graf, and L. Y. Chiang, *Magneto-quantum oscillations of the specific heat in the Bechgaard salt $(TMTSF)_2ClO_4$,* Synthetic Metals **42**, 1667 (1991).

[110] L. Wang and O. Vafek, *Quantum oscillations of the specific heat in d-wave superconductors with loop current order,* Physical Review B **88**, 024506 (2013).

[111] B. A. Green and B. S. Chandrasekhar, *Observation of Oscillatory Magnetostriction in Bismuth at 4.2°K,* Physical Review Letters **11**, 331 (1963).

[112] T. E. Thompson, P. R. Aron, B. S. Chandrasekhar, and D. N. Langenberg, *Magnetostriction and Magnetoelastic Quantum Oscillations in $p - PbTe$,* Physical Review B **4**, 518 (1971).

[113] R. Griessen and R. S. Sorbello, *Oscillatory Magnetostriction and the Stress Dependence of the Fermi Surface of Aluminum,* Physical Review B **6**, 2198 (1972).

[114] M. Doerr, S. Schönecker, A. Haase, E. Kampert, J. A. A. J. Perenboom, M. Richter, M. Rotter, M. S. Kim, and M. Loewenhaupt, *High Field Magnetoelastic Quantum Oscillations of Palladium,* Journal of Low Temperature Physics **159**, 20 (2010).

[115] D. A. Zocco, K. Grube, F. Eilers, T. Wolf, and H. v. Löhneysen, *Fermi Surface of KFe_2As_2 from Quantum Oscillations in Magnetostriction,* in *Proceedings of the International Conference on Strongly Correlated Electron Systems (SCES2013)*, Vol. 3 (Journal of the Physical Society of Japan, 2014).

[116] J. Xiang, S. Hu, Z. Song, M. Lv, J. Zhang, L. Zhao, W. Li, Z. Chen, S. Zhang, J.-T. Wang, Y.-f. Yang, X. Dai, F. Steglich, G. Chen, and P. Sun, *Giant Magnetic Quantum Oscillations in the Thermal Conductivity of TaAs: Indications of Chiral Zero Sound,* Physical Review X **9**, 031036 (2019).

[117] P. Czajka, T. Gao, M. Hirschberger, P. Lampen-Kelley, A. Banerjee, J. Yan, D. G. Mandrus, S. E. Nagler, and N. P. Ong, *Oscillations of the thermal conductivity in the spin-liquid state of α-$RuCl_3$,* Nature Physics **17**, 915 (2021).

[118] V. L. Gurevich, V. G. Skobov, and Y. A. Firsov, *Giant quantum oscillations in the acoustical absorption by a metal in a magnetic field,* Soviet Physics–JETP [translation of Zhurnal Eksperimentalnoi i Teoreticheskoi Fiziki] **13**, 552 (1961).

[119] Y. Shapira, S. J. Williamson, and S. Fischler, *Quantum Oscillations in the Ultrasonic Attenuation and Magnetic Susceptibility of InBi,* Physical Review **144**, 715 (1966).

[120] C. Schindler, D. Gorbunov, S. Zherlitsyn, S. Galeski, M. Schmidt, J. Wosnitza, and J. Gooth, *Strong anisotropy of the electron-phonon interaction in NbP probed by magnetoacoustic quantum oscillations,* Physical Review B **102**, 165156 (2020).

[121] D. Shoenberg, *Magnetic Oscillations in Metals* (Cambridge University Press, 1984).

[122] A. S. Joseph and A. C. Thorsen, *Low-Field de Haas-van Alphen Effect in Ag,* Physical Review **138**, A1159 (1965).

[123] D. Shoenberg and J. Vanderkooy, *Absolute amplitudes in the de Haas-van Alphen effect,* Journal of Low Temperature Physics **2**, 483 (1970).

[124] B. Vignolle, D. Vignolles, M.-H. Julien, and C. Proust, *From quantum oscillations to charge order in high-T_c copper oxides in high magnetic fields,* Comptes Rendus Physique **14**, 39 (2013).

[125] A. I. Coldea, S. F. Blake, S. Kasahara, A. A. Haghighirad, M. D. Watson, W. Knafo, E. S. Choi, A. McCollam, P. Reiss, T. Yamashita, M. Bruma, S. C. Speller, Y. Matsuda, T. Wolf, T. Shibauchi, and A. J. Schofield, *Evolution of the low-temperature Fermi surface of superconducting $FeSe_{1-x}S_x$ across a nematic phase transition,* npj Quantum Materials **4**, 1 (2019).

[126] L. Taillefer, R. Newbury, G. G. Lonzarich, Z. Fisk, and J. L. Smith, *Direct observation of heavy quasiparticles in UPt_3 via the dHvA effect,* Journal of Magnetism and Magnetic Materials **63**, 372 (1987).

[127] J. Hornung, S. Mishra, J. Stirnat, M. Raba, B. V. Schwarze, J. Klotz, D. Aoki, J. Wosnitza, T. Helm, and I. Sheikin, *Anomalous quantum oscillations of $CeCoIn_5$ in high magnetic fields,* Physical Review B **104**, 235155 (2021).

[128] L. Onsager, *Interpretation of the de Haas-van Alphen effect,* The London, Edinburgh, and Dublin Philosophical Magazine and Journal of Science **43**, 1006 (1952).

[129] I. M. Lifshitz and A. Kosevich, *Theory of magnetic susceptibility in metals at low temperatures,* Soviet Physics–JETP [translation of Zhurnal Eksperimentalnoi i Teoreticheskoi Fiziki] **2**, 636 (1956).

[130] S. Das Sarma and F. Stern, *Single-particle relaxation time versus scattering time in an impure electron gas,* Physical Review B **32**, 8442 (1985).

[131] T. Wang, J. Bai, S. Sakai, Y. Ohno, and H. Ohno, *Magnetotransport studies of AlGaN/GaN heterostructures grown on sapphire substrates: Effective mass and scattering time,* Applied Physics Letters **76**, 2737 (2000).

[132] L. Hsu and W. Walukiewicz, *Transport-to-quantum lifetime ratios in AlGaN/GaN heterostructures,* Applied Physics Letters **80**, 2508 (2002).

[133] L. Li, G. J. Ye, V. Tran, R. Fei, G. Chen, H. Wang, J. Wang, K. Watanabe, T. Taniguchi, L. Yang, X. H. Chen, and Y. Zhang, *Quantum oscillations in a two-dimensional electron gas in black phosphorus thin films,* Nature Nanotechnology **10**, 608 (2015).

[134] M. Katsnelson and A. Geim, *Electron scattering on microscopic corrugations in graphene,* Philosophical Transactions of the Royal Society A: Mathematical, Physical and Engineering Sciences **366**, 195 (2007).

[135] A. Ferreira, T. G. Rappoport, M. A. Cazalilla, and A. H. Castro Neto, *Extrinsic Spin Hall Effect Induced by Resonant Skew Scattering in Graphene,* Physical Review Letters **112**, 066601 (2014).

[136] J. Sinova, S. O. Valenzuela, J. Wunderlich, C. H. Back, and T. Jungwirth, *Spin Hall effects,* Reviews of Modern Physics **87**, 1213 (2015).

[137] Q.-Q. Yuan, L. Zhou, Z.-C. Rao, S. Tian, W.-M. Zhao, C.-L. Xue, Y. Liu, T. Zhang, C.-Y. Tang, Z.-Q. Shi, Z.-Y. Jia, H. Weng, H. Ding, Y.-J. Sun, H. Lei, and S.-C. Li, *Quasiparticle interference evidence of the topological Fermi arc states in chiral fermionic semimetal CoSi,* Science Advances **5** (2019), 10.1126/sciadv.aaw9485.

[138] X. Xu, X. Wang, T. A. Cochran, D. S. Sanchez, G. Chang, I. Belopolski, G. Wang, Y. Liu, H.-J. Tien, X. Gui, W. Xie, M. Z. Hasan, T.-R. Chang, and S. Jia, *Crystal growth and quantum oscillations in the topological chiral semimetal CoSi,* Physical Review B **100**, 045104 (2019).

[139] D. S. Wu, Z. Y. Mi, Y. J. Li, W. Wu, P. L. Li, Y. T. Song, G. T. Liu, G. Li, and J. L. Luo, *Single Crystal Growth and Magnetoresistivity of Topological Semimetal CoSi,* Chinese Physics Letters **36**, 077102 (2019).

[140] C. Guo, L. Hu, C. Putzke, J. Diaz, X. Huang, K. Manna, F.-R. Fan, C. Shekhar, Y. Sun, C. Felser, C. Liu, B. A. Bernevig, and P. J. W. Moll, *Quasi-symmetry-protected topology in a semi-metal,* Nature Physics **18**, 813 (2022).

[141] S. Sasmal, G. Dwari, B. B. Maity, V. Saini, A. Thamizhavel, and R. Mondal, *Shubnikov-de Haas and de Haas-van Alphen oscillations in Czochralski grown CoSi single crystal,* Journal of Physics: Condensed Matter **34**, 425702 (2022).

[142] H. Wang, S. Xu, X.-Q. Lu, X.-Y. Wang, X.-Y. Zeng, J.-F. Lin, K. Liu, Z.-Y. Lu, and T.-L. Xia, *De Haas–van Alphen quantum oscillations and electronic structure in the large-Chern-Number topological chiral semimetal CoSi,* Physical Review B **102**, 115129 (2020).

[143] J. von Neuman and E. Wigner, *Uber merkwürdige diskrete Eigenwerte. Uber das Verhalten von Eigenwerten bei adiabatischen Prozessen,* Physikalische Zeitschrift **30**, 467 (1929).

[144] C.-K. Chiu, J. C. Y. Teo, A. P. Schnyder, and S. Ryu, *Classification of topological quantum matter with symmetries,* Reviews of Modern Physics **88**, 035005 (2016).

[145] A. A. Burkov, *Weyl Metals,* Annual Review of Condensed Matter Physics **9**, 359 (2018).

[146] C.-K. Chiu and A. P. Schnyder, *Classification of reflection-symmetry-protected topological semimetals and nodal superconductors,* Physical Review B **90**, 205136 (2014).

[147] A. H. Castro Neto, F. Guinea, N. M. R. Peres, K. S. Novoselov, and A. K. Geim, *The electronic properties of graphene,* Reviews of Modern Physics **81**, 109 (2009).

[148] Y. X. Zhao and A. P. Schnyder, *Nonsymmorphic symmetry-required band crossings in topological semimetals,* Physical Review B **94**, 195109 (2016).

[149] T. Bzdušek, Q. Wu, A. Rüegg, M. Sigrist, and A. A. Soluyanov, *Nodal-chain metals,* Nature **538**, 75 (2016).

[150] A. P. Schnyder, *Lecture notes on: Accidental and symmetry-enforced band crossings in topological semimetals,* Topological Matter School, San Sebastian, Spain (2018).

[151] J. Zhang, Y.-H. Chan, C.-K. Chiu, M. G. Vergniory, L. M. Schoop, and A. P. Schnyder, *Topological band crossings in hexagonal materials,* Physical Review Materials **2**, 074201 (2018).

[152] N. Huber, K. Alpin, G. L. Causer, L. Worch, A. Bauer, G. Benka, M. M. Hirschmann, A. P. Schnyder, C. Pfleiderer, and M. A. Wilde, *Network of Topological Nodal Planes, Multifold Degeneracies, and Weyl Points in CoSi,* Physical Review Letters **129**, 026401 (2022).

[153] A. E. Petrova, V. N. Krasnorussky, A. A. Shikov, W. M. Yuhasz, T. A. Lograsso, J. C. Lashley, and S. M. Stishov, *Elastic, thermodynamic, and electronic properties of MnSi, FeSi, and CoSi,* Physical Review B **82**, 155124 (2010).

[154] P. Blaha, K. Schwarz, F. Tran, R. Laskowski, G. K. H. Madsen, and L. D. Marks, *WIEN2k: An APW+lo program for calculating the properties of solids,* The Journal of Chemical Physics **152**, 074101 (2020), https://doi.org/10.1063/1.5143061 .

[155] P. Giannozzi, S. Baroni, N. Bonini, M. Calandra, R. Car, C. Cavazzoni, D. Ceresoli, G. L. Chiarotti, M. Cococcioni, I. Dabo, A. D. Corso, S. de Gironcoli, S. Fabris, G. Fratesi, R. Gebauer, U. Gerstmann, C. Gougoussis, A. Kokalj, M. Lazzeri, L. Martin-Samos, N. Marzari, F. Mauri, R. Mazzarello, S. Paolini, A. Pasquarello, L. Paulatto, C. Sbraccia, S. Scandolo, G. Sclauzero, A. P. Seitsonen, A. Smogunov, P. Umari, and R. M. Wentzcovitch, *QUANTUM ESPRESSO: A modular and open-source software project for quantum simulations of materials,* Journal of Physics: Condensed Matter **21**, 395502 (2009).

[156] A. Dal Corso, *Pseudopotentials periodic table: From H to Pu,* Computational Materials Science **95**, 337 (2014).

[157] J. P. Perdew, K. Burke, and M. Ernzerhof, *Generalized gradient approximation made simple,* Physical Review Letters **77**, 3865 (1996).

[158] T. Fukui, Y. Hatsugai, and H. Suzuki, *Chern Numbers in Discretized Brillouin Zone: Efficient Method of Computing (Spin) Hall Conductances,* Journal of the Physical Society of Japan **74**, 1674 (2005).

[159] J.-Z. Ma, Q.-S. Wu, M. Song, S.-N. Zhang, E. B. Guedes, S. A. Ekahana, M. Krivenkov, M. Y. Yao, S.-Y. Gao, W.-H. Fan, T. Qian, H. Ding, N. C. Plumb, M. Radovic, J. H. Dil, Y.-M. Xiong, K. Manna, C. Felser, O. V. Yazyev, and M. Shi, *Observation of a singular Weyl point surrounded by charged nodal walls in PtGa,* Nature Communications **12**, 3994 (2021).

[160] C. S. A. Müller, T. Khouri, M. R. van Delft, S. Pezzini, Y.-T. Hsu, J. Ayres, M. Breitkreiz, L. M. Schoop, A. Carrington, N. E. Hussey, and S. Wiedmann, *Determination of the Fermi surface and field-induced quasiparticle tunneling around the Dirac nodal loop in ZrSiS,* Physical Review Research **2**, 023217 (2020).

[161] R. G. Chambers, *Magnetic breakdown in real metals,* Proceedings of the Physical Society **88**, 701 (1966).

[162] P. M. C. Rourke and S. R. Julian, *Numerical extraction of de Haas–van Alphen frequencies from calculated band energies,* Computer Physics Communications **183**, 324 (2012).

[163] M. H. Cohen and L. M. Falicov, *Magnetic Breakdown in Crystals,* Physical Review Letters **7**, 231 (1961).

[164] M. I. Kaganov and A. A. Slutskin, *Coherent magnetic breakdown,* Physics Reports **98**, 189 (1983).

[165] E. I. Blount, *Bloch electrons in a magnetic field,* Physical Review **126**, 1636 (1962).

[166] D. Shoenberg, *Magnetic interaction and phase smearing,* Journal of Low Temperature Physics **25**, 755 (1976).

[167] J. M. Perz and D. Shoenberg, *Spin properties of conduction electrons in sodium,* Journal of Low Temperature Physics **25**, 275 (1976).

[168] A. S. Alexandrov and A. M. Bratkovsky, *New fundamental dHvA frequency in canonical low-dimensional Fermi liquids,* Physics Letters A **234**, 53 (1997).

[169] V. M. Gvozdikov, A. G. M. Jansen, D. A. Pesin, I. D. Vagner, and P. Wyder, *De Haas–van Alphen and chemical potential oscillations in the magnetic-breakdown quasi-two-dimensional organic conductor* $\kappa-(BEDT-TTF)_2Cu(NCS)_2$, Physical Review B **70**, 245114 (2004).

[170] E. Ohmichi, Y. Maeno, and T. Ishiguro, *Enhancement of the Sum and Difference Frequencies in Shubnikov-de Haas Oscillation at Yamaji Angle in the Layered Perovskite* Sr_2RuO_4, Journal of the Physical Society of Japan **68**, 24 (1999).

[171] R. W. Stark and C. B. Friedberg, *Quantum Interference of Electron Waves in a Normal Metal,* Physical Review Letters **26**, 556 (1971).

[172] V. Leeb, N. Huber, C. Pfleiderer, J. Knolle, and M. A. Wilde, *A field guide to non-Onsager quantum oscillations in metals,* unpublished (2024).

[173] M. G. Priestley, L. M. Falicov, and G. Weisz, *Experimental and Theoretical Study of Magnetic Breakdown in Magnesium,* Physical Review **131**, 617 (1963).

[174] M. P. Everson, A. Johnson, H.-A. Lu, R. V. Coleman, and L. M. Falicov, *Magnetoquantum oscillations, magnetic breakdown, and Fermi-surface modifications in $NbSe_3$,* Physical Review B **36**, 6953 (1987).

[175] M. R. van Delft, S. Pezzini, T. Khouri, C. S. A. Müller, M. Breitkreiz, L. M. Schoop, A. Carrington, N. E. Hussey, and S. Wiedmann, *Electron-Hole Tunneling Revealed by Quantum Oscillations in the Nodal-Line Semimetal HfSiS,* Physical Review Letters **121**, 256602 (2018).

[176] Y. Aharonov and D. Bohm, *Significance of Electromagnetic Potentials in the Quantum Theory,* Physical Review **115**, 485 (1959).

[177] D. Graf, J. S. Brooks, E. S. Choi, M. Almeida, R. T. Henriques, J. C. Dias, and S. Uji, *Quantum interference in the quasi-one-dimensional organic conductor $(Per)_2Au(mnt)_2$,* Physical Review B **75**, 245101 (2007).

[178] M. V. Kartsovnik, G. Y. Logvenov, T. Ishiguro, W. Biberacher, H. Anzai, and N. D. Kushch, *Direct Observation of the Magnetic-Breakdown Induced Quantum Interference in the Quasi-Two-Dimensional Organic Metal κ-(BEDT-TTF)$_2$CU(NCS)$_2$,* Physical Review Letters **77**, 2530 (1996).

[179] A. Audouard, J.-Y. Fortin, D. Vignolles, R. B. Lyubovskii, L. Drigo, G. V. Shilov, F. Duc, E. I. Zhilyaeva, R. N. Lyubovskaya, and E. Canadell, *Non-Lifshitz–Kosevich field- and temperature-dependent amplitude of quantum oscillations in the quasi-two dimensional metal ϑ-$(ET)_4ZnBr_4(C_6H_4Cl_2)$,* Journal of Physics: Condensed Matter **27**, 315601 (2015).

[180] A. Neubauer, J. Bœuf, A. Bauer, B. Russ, H. v. Löhneysen, and C. Pfleiderer, *Ultra-high vacuum compatible image furnace,* Review of Scientific Instruments **82**, 013902 (2011).

[181] A. Bauer, G. Benka, A. Regnat, C. Franz, and C. Pfleiderer, *Ultra-high vacuum compatible preparation chain for intermetallic compounds,* Review of Scientific Instruments **87**, 113902 (2016).

[182] G. A. Benka, *Preparation and Investigation of Intermetallic Magnetic Compounds with Disorder*, Ph.D. thesis, Technische Universität München (2021).

[183] S. S. Samatham, D. Venkateshwarlu, and V. Ganesan, *Investigations on pseudogap semimetal CoSi,* Materials Research Express **1**, 026503 (2014).

[184] A. T. Burkov, S. V. Novikov, V. K. Zaitsev, and H. Reith, *Transport properties of cobalt monosilicide and its alloys at low temperatures,* Semiconductors **51**, 689 (2017).

[185] *Oxford Instruments Kelvinox MX400,* https://nanoscience.oxinst.com (accessed 17.06.2024).

[186] O. V. Lounasmaa, *Experimental Principles and Methods Below 1 K* (Academic Press, 1974).

[187] F. Pobell, *Matter and Methods at Low Temperatures* (Springer Science & Business Media, 2013).

[188] N. Huber, *Investigation of Shubnikov-de Haas Oscillations in the Topological Chiral Semimetal CoSi*, M.Sc. Thesis, Technische Universität München (2020).

[189] *Attocube ANRv51/ULT/RES+/HV Rotator (360° endless),* https://www.attocube.com/en/products/nanopositioners/low-temperature-nanopositioners/anrv51ultres-hv-rotator-360-endless (accessed 17.06.2024).

[190] *CMR-Direct LTT-m Low Temperature Transformer,* https://www.cmr-direct.com/shop/02-20-011-ltt-m-335?category=25 (accessed 17.06.2024).

[191] B. Salce, H. Godfrin, L. Dumoulin, P. Garoche, B. Pannetier, B. Equer, P. Hubert, C. Urbina, J. Lamarre, J. Brison, D. Lesueur, J. Bret, F. Ayela, N. Coron, and L. Gonzalez-Mestres, *Radiation detection at very low temperature DRTBT 1991 Aussois - Course collection,* in *DRTBT 1991: 1 Autumn School on Radiation Detection at Very Low Temperature* (1991).

[192] J. Ekin, *Experimental Techniques for Low-Temperature Measurements* (Oxford University Press, 2006).

[193] *Quantum Design PPMS,* https://www.qdusa.com/products/ppms.html (accessed 17.06.2024).

[194] *Quantum Design MPMS3 SQUID-Magnetometer,* https://qd-europe.com/de/en/produkt/mpms3-squid-magnetometer (accessed 17.06.2024).

[195] J. O. Smith, *Spectral Audio Signal Processing*, second edition ed. (W3K Publishing, 2011).

[196] K. M. M. Prabhu, *Window Functions and Their Applications in Signal Processing* (Taylor & Francis, 2014).

[197] M. Łuczyński, A. Dobrucki, and S. Brachmański, *Active tone elimination algorithm using FFT with interpolation and zero-padding,* in *2020 Signal Processing: Algorithms, Architectures, Arrangements, and Applications (SPA)* (2020) p. 163.

[198] S. Jia, S.-Y. Xu, and M. Z. Hasan, *Weyl semimetals, Fermi arcs and chiral anomalies,* Nature Materials **15**, 1140 (2016).

[199] N. Sirica, R. I. Tobey, L. X. Zhao, G. F. Chen, B. Xu, R. Yang, B. Shen, D. A. Yarotski, P. Bowlan, S. A. Trugman, J.-X. Zhu, Y. M. Dai, A. K. Azad, N. Ni, X. G. Qiu, A. J. Taylor, and R. P. Prasankumar, *Tracking Ultrafast Photocurrents in the Weyl Semimetal TaAs Using THz Emission Spectroscopy,* Physical Review Letters **122**, 197401 (2019).

[200] Y. Gao, S. Kaushik, E. J. Philip, Z. Li, Y. Qin, Y. P. Liu, W. L. Zhang, Y. L. Su, X. Chen, H. Weng, D. E. Kharzeev, M. K. Liu, and J. Qi, *Chiral terahertz wave emission from the Weyl semimetal TaAs,* Nature Communications **11**, 720 (2020).

[201] S. Kawarazaki, H. Yasuoka, and Y. Nakamura, *Moment formation on Co atom in FeSi-CoSi mixed system -Co^{59} NMR in the paramagnetic state,* Solid State Communications **10**, 919 (1972).

[202] V. N. Narozhnyi and V. N. Krasnorussky, *Studying the magnetic properties of CoSi single crystals,* Journal of Experimental and Theoretical Physics **116**, 780 (2013).

[203] A. B. Pippard, *Magnetoresistance in Metals* (Cambridge University Press, 1989).

[204] M. A. Wilde and C. Pfleiderer, *Large curvature near a small gap,* Nature Physics **18**, 731 (2022).

[205] N. Huber, S. Mishra, I. Sheikin, K. Alpin, A. P. Schnyder, G. Benka, A. Bauer, C. Pfleiderer, and M. A. Wilde, *Fermi surface of the chiral topological semimetal CoSi,* Physical Review B **109**, 205115 (2024).

[206] H. Yang, M. Schmidt, V. Süss, M. Chan, F. F. Balakirev, R. D. McDonald, S. S. P. Parkin, C. Felser, B. Yan, and P. J. W. Moll, *Quantum oscillations in the type-II Dirac semi-metal candidate $PtSe_2$,* New Journal of Physics **20**, 043008 (2018).

[207] A. I. Coldea, J. D. Fletcher, A. Carrington, J. G. Analytis, A. F. Bangura, J.-H. Chu, A. S. Erickson, I. R. Fisher, N. E. Hussey, and R. D. McDonald, *Fermi Surface of Superconducting LaFePO Determined from Quantum Oscillations,* Physical Review Letters **101**, 216402 (2008).

[208] S. Chapman, M. Hunt, P. Meeson, P. H. P. Reinders, M. Springford, and M. Norman, *Heavy quasiparticles in $CeCu_6$ studied using magnetic quantum oscillations,* Journal of Physics: Condensed Matter **2**, 8123 (1990).

[209] J. Y. Liu, J. Hu, Q. Zhang, D. Graf, H. B. Cao, S. M. A. Radmanesh, D. J. Adams, Y. L. Zhu, G. F. Cheng, X. Liu, W. A. Phelan, J. Wei, M. Jaime, F. Balakirev, D. A. Tennant, J. F. DiTusa, I. Chiorescu, L. Spinu, and Z. Q. Mao, *A magnetic topological semimetal $Sr_{1-y}Mn_{1-z}Sb_2$ ($y, z < 0.1$),* Nature Materials **16**, 905 (2017).

[210] A. Alexandradinata, C. Wang, W. Duan, and L. Glazman, *Revealing the Topology of Fermi-Surface Wave Functions from Magnetic Quantum Oscillations,* Physical Review X **8**, 011027 (2018).

[211] W. Zhao and X. Wang, *Berry phase in quantum oscillations of topological materials,* Advances in Physics: X **7**, 2064230 (2022).

[212] R. B. Dingle, *Some magnetic properties of metals II. The influence of collisions on the magnetic behaviour of large systems,* Proceedings of the Royal Society of London. Series A. Mathematical and Physical Sciences **211**, 517 (1952).

[213] T. E. O'Brien, M. Diez, and C. W. J. Beenakker, *Magnetic Breakdown and Klein Tunneling in a Type-II Weyl Semimetal,* Physical Review Letters **116**, 236401 (2016).

[214] V. M. Polyanovskii, *Anomalous temperature-dependence of the amplitude of quantum oscillations of the magnetoresistance in quasitwo-dimensional systems,* Soviet Physics Semiconductors - USSR **22**, 1408 (1988).

[215] D. R. Leadley, R. Fletcher, R. J. Nicholas, F. Tao, C. T. Foxon, and J. J. Harris, *Intersubband resonant scattering in $GaAs$-$Ga_{1-x}Al_xAs$ heterojunctions,* Physical Review. B, Condensed Matter **46**, 12439 (1992).

[216] P. T. Coleridge, *Inter-subband scattering in a 2D electron gas,* Semiconductor Science and Technology **5**, 961 (1990).

[217] M. E. Raikh and T. V. Shahbazyan, *Magnetointersubband oscillations of conductivity in a two-dimensional electronic system,* Physical Review B **49**, 5531 (1994).

[218] A. V. Goran, A. A. Bykov, A. I. Toropov, and S. A. Vitkalov, *Effect of electron-electron scattering on magnetointersubband resistance oscillations of two-dimensional electrons in GaAs quantum wells,* Physical Review B **80**, 193305 (2009).

[219] V. Polyanovsky, *High-temperature quantum oscillations of the magnetoresistance in layered systems,* Physical Review B **47**, 1985 (1993).

[220] P. D. Grigoriev, *Theory of the Shubnikov–de Haas effect in quasi-two-dimensional metals,* Physical Review B **67**, 144401 (2003).

[221] I. O. Thomas, V. V. Kabanov, and A. S. Alexandrov, *Shubnikov-de Haas effect in multiband quasi-two-dimensional metals,* Physical Review B **77**, 075434 (2008).

[222] E. Fermi, *Nuclear Physics: A Course Given by Enrico Fermi at the University of Chicago, Revised Edition* (University of Chicago Press, 1974).

[223] C. Mera Acosta, L. Yuan, G. M. Dalpian, and A. Zunger, *Different shapes of spin textures as a journey through the Brillouin zone,* Physical Review B **104**, 104408 (2021).

[224] W. Tan, X. Jiang, Y. Li, X. Wu, J. Wang, and B. Huang, *A Unified Understanding of Diverse Spin Textures of Kramers–Weyl Fermions in Nonmagnetic Chiral Crystals,* Advanced Functional Materials **32**, 2208023 (2022).

[225] J. A. Krieger, S. Stolz, I. Robredo, K. Manna, E. C. McFarlane, M. Date, E. B. Guedes, J. H. Dil, C. Shekhar, H. Borrmann, Q. Yang, M. Lin, V. N. Strocov, M. Caputo, B. Pal, M. D. Watson, T. K. Kim, C. Cacho, F. Mazzola, J. Fujii, I. Vobornik, S. S. P. Parkin, B. Bradlyn, C. Felser, M. G. Vergniory, and N. B. M. Schröter, *Parallel spin-momentum locking in a chiral topological semimetal,* arXiv:2210.08221 [cond-mat] .

[226] A. A. Allocca and N. R. Cooper, *Low-frequency quantum oscillations from interactions in layered metals,* Physical Review Research **3**, L042009 (2021).

[227] I. Y. Phinney, D. A. Bandurin, C. Collignon, I. A. Dmitriev, T. Taniguchi, K. Watanabe, and P. Jarillo-Herrero, *Strong Interminivalley Scattering in Twisted Bilayer Graphene Revealed by High-Temperature Magneto-Oscillations,* Physical Review Letters **127**, 056802 (2021).

[228] L. Ding, J. Koo, C. Yi, L. Xu, H. Zuo, M. Yang, Y. Shi, B. Yan, K. Behnia, and Z. Zhu, *Quantum oscillations, magnetic breakdown and thermal Hall effect in $Co_3Sn_2S_2$,* Journal of Physics D: Applied Physics **54**, 454003 (2021).

[229] O. Pavlosiuk, P. W. Swatek, J.-P. Wang, P. Wiśniewski, and D. Kaczorowski, *Giant magnetoresistance, Fermi-surface topology, Shoenberg effect, and vanishing quantum oscillations in the type-II Dirac semimetal candidates $MoSi_2$ and WSi_2,* Physical Review B **105**, 075141 (2022).

[230] P. Reiss, D. Graf, A. A. Haghighirad, W. Knafo, L. Drigo, M. Bristow, A. J. Schofield, and A. I. Coldea, *Quenched nematic criticality and two superconducting domes in an iron-based superconductor,* Nature Physics **16**, 89 (2020).

[231] V. Leeb and J. Knolle, *Interband scattering- and nematicity-induced quantum oscillation frequency in FeSe,* Physical Review B **109**, L081109 (2024).

[232] N. Huber, V. Leeb, A. Bauer, G. Benka, J. Knolle, C. Pfleiderer, and M. A. Wilde, *Quantum oscillations of the quasiparticle lifetime in a metal,* Nature **621**, 276 (2023).

[233] V. Leeb and J. Knolle, *Theory of difference-frequency quantum oscillations,* Physical Review B **108**, 054202 (2023).

Publications

Part of the work presented in Chapter 4 has been published in:

- **Network of Topological Nodal Planes, Multifold Degeneracies, and Weyl Points in CoSi**
  Nico Huber[†], Kirill Alpin[†], Grace L. Causer, Lukas Worch, Andreas Bauer, Georg Benka, Moritz M. Hirschmann, Andreas P. Schnyder, Christian Pfleiderer, and Marc A. Wilde
  Physical Review Letters **129**, 026401 (2022)

- **Fermi surface of the chiral topological semimetal CoSi**
  Nico Huber, Sanu Mishra, Ilya Sheikin, Kirill Alpin, Andreas P. Schnyder, Georg Benka, Andreas Bauer, Christian Pfleiderer, and Marc A. Wilde
  Physical Review B **109**, 205115 (2024)

Part of the work presented in Chapter 5 has been published in:

- **Quantum oscillations of the quasiparticle lifetime in a metal**
  Nico Huber[†], Valentin Leeb[†], Andreas Bauer, Georg Benka, Johannes Knolle, Christian Pfleiderer, and Marc A. Wilde
  Nature **621**, 276–281 (2023)

Other publications (in collaboration):

- **Weyl Nodes Close to the Fermi Energy in NbAs**
  Marcel Naumann, Frank Arnold, Zuzana Medvecka, Shu-Chun Wu, Vicky Süss, Marcus Schmidt, Binghai Yan, Nico Huber, Lukas Worch, Marc A. Wilde, Claudia Felser, Yan Sun, Elena Hassinger
  physica status solidi (b) **259**, 2100165 (2022)

[†]These authors contributed equally to this work.

Acknowledgments

This thesis would not have been possible without the support of many people. I am thankful for the advice, guidance and assistance I received and the collaborations and friendships that developed along the way. In particular I want to thank:

Prof. Christian Pfleiderer for your support, guidance and trust over the course of many years. Your enthusiasm for what you are doing was always a big motivation for me and throughout my time at the chair I always felt that there is something new to discover. Thank you for creating a great environment for students to learn and grow at your chair.

Dr. Marc Wilde for your guidance during my Master's and PhD thesis. Your lecture is what got me interested in quantum oscillations in the first place and the numerous discussions of our experimental results helped me a lot in gaining a deeper understanding of the physics behind them. Thank you also for the detailed DFT calculations and your help in showing me how to work with them.

Dr. Andreas Bauer for always assisting me with any problem I came to you with. Your knowledge and experience helped me in many situations and I am grateful for all the advice you gave me throughout the years.

Prof. Antony Carrington for agreeing to be my mentor for the PhD. I am grateful for the interesting scientific and technical discussions and the advice you gave me during our status meetings.

My office mates Alexander Engelhardt, Anh Tong, Carolina Burger and Christian Oberleitner. Thank you for sharing the best office at the chair. I had a great time with you and wish you all the best.

The PhD students next door Michelle Hollricher, Christoph Resch, Leo Maximov, Florian Kübelbäck, Michael Lampl and André Deyerling. Thanks for the good atmosphere at the chair and for always being helpful whenever there was a problem in the lab. Also thanks for reminding our office from time to time when it was 4pm.

The Bachelor, Master and working students I had the pleasure of working together with, in particular Ivan Volkau, Simon Röder, Louw Feenstra and Michael

Schmidlechner. Thank you for all the work you put into your projects and the fantastic results you produced.

The kiutra team, especially Jan Spallek and Alexander Regnat, for your guidance at my earliest days at the chair. I very much enjoyed working together with you on the Dryo and MARDER and wish you all the best for the future of kiutra.

Our technicians Stefan Giemsa and Andreas Mantwill for keeping everything running and to Stefan for the discussions on CAD designs and technical issues.

Our administrative office Sonja Niedermeier, Lisa Seitz, Astrid Mühlberg and Martina Meven for your assistance with the bureaucracy.

All other current and former members of E51 whom I had the pleasure to get to know during my time at the chair. Steffen Säubert, Pau Jorba, Andreas Wendl, Franz Haslbeck, Wolfgang Simeth, Markus Kleinhans, Grace Causer, Vivek Kumar, Denis Mettus, Jon Leiner, Felix Rucker, Alfonso Chacon, Marco Halder, Christopher Duvinage, Marc Seifert, Christoph Schnarr, Schorsch Sauther, Tomek Schulz, Fabian Jochum, Lukas Worch, Daniel Apweiler, Katharina Müller, Tobias Konrad, Lukas Bauer, Korbinian Fellner, Luke Jatho and many more.

The team at the reactor Johanna Jochum, Lukas Beddrich, Peter Wild, Markos Skoulatos for some nice evenings at the conferences in Incheon and Bologna.

Prof. Peter Böni for delivering unforgettable speeches at our Christmas parties.

The central workshop of the Physics department, especially the two Manfreds, for manufacturing even the most intricate parts for the various setups I have been working on during my time here. I have learned a lot about designing mechanical components from working together with you.

The team of the crystal laboratory Susanne Mayr, Claudia Schweiger, Katarzyna Danielewicz, Michael Stanger, Sandra Navaz Rubio, Gerald Neumann and Andreas Erb. Thank you for the preparation of numerous samples for my measurements and gold plating some of the components for the setups I designed.

Ilya Sheikin and Sanu Mishra for a perfectly prepared measurement environment and two successful experiments at the high-field magnetic laboratory in Grenoble.

Andreas P. Schnyder, Kirill Alpin and Moritz M. Hirschmann from the Max-Planck-Institute in Stuttgart. Thank you for the theoretical insights into the band structure and topology of CoSi and the fruitful collaboration.

Prof. Johannes Knolle and Valentin Leeb for numerous discussions on the origin of the difference frequency in our measurements and its implications. Our collaboration was a wonderful example of how the interplay between experiment and theory can work and I am looking forward to future joint projects.

The Stammtisch members Patrick Wastian, Katharina Hirschmann, Manuel Lebert, Markus Eder, Jakob Unfried, Wolfgang Gottwald and Rika Unkelbach. I had many great evenings with you during our studies and am happy that we keep meeting up regularly.

Klaus Eibensteiner for being a great friend and the good times we spent together.

My family, especially my parents Irene and Armin, for always being supportive and enabling me to do what I do. I also want to thank my brother Philipp for the advice he gave me over the years and my aunt Edith and uncle Walter who shared their home with me during my Bachelor.

My dear Caro for sharing many good memories and for always being there for me. Thank you for being you.

Disclaimer

This thesis, apart from this disclaimer, has been created solely by the author without the assistance of any generative artificial intelligence tools or technologies for content generation. All research, writing, and primary editing have been conducted by human effort, ensuring the integrity and originality of the work. Any software or digital tools used were limited to traditional word processing, data analysis, and reference management. This disclaimer is the only part of the thesis where content has been created with the help of ChatGPT, an AI language model developed by OpenAI.

While the content has not been generated by AI, the wording of individual paragraphs has been improved with the help of ChatGPT. The results were carefully revised by the author and only changes that did not alter the meaning but improved the readability have been incorporated.

Garching, 22.07.2024 Nico Huber